

Simulation, Modeling, and Characterization of the Wakes of Fixed and Moving Cylinders

Osama A. Marzouk

Dissertation submitted to the faculty of the Virginia Polytechnic Institute and State
University in partial fulfillment of the requirements for the degree of

Doctor of Philosophy
In
Engineering Mechanics

Dr. Ali H. Nayfeh, Chair
Dr. Saad A. Ragab
Dr. Muhammad R. Hajj
Dr. Slimane Adjerid
Dr. William J. Devenport

February 6, 2009
Blacksburg, Virginia

Keywords: Wake, Cylinder, Nonlinear Model, CFD, Lift, Drag, Cross-Flow, In-Line

Simulation, Modeling, and Characterization of the Wakes of Fixed and Moving Cylinders

Osama A. Marzouk

ABSTRACT

The first goal of this work was to develop models based on nonlinear ordinary-differential equations or nonlinear algebraic equations, which produce the lift and drag coefficients on a cylinder or a cylinder-like structure. We introduced an improved wake oscillator for the lift, which combines the van der Pol and Duffing equations. We proposed a two-term quadratic model that relates the drag and lift coefficients, which reproduces the phase relationship between the drag and lift and its variation with the Reynolds number. We found that a mixed-type (external and parametric) forcing is needed to represent the effects of the cylinder motion.

The second goal of this work was to develop a deeper understanding of the shedding and fluid forces on a cylinder and how they depend on its oscillatory motion within and outside the synchronization (or lock-in) band of frequencies. We performed extensive CFD (computational fluid dynamics) simulations and solved the unsteady Reynolds-averaged Navier-Stokes equations that govern the flow fields around fixed and moving (in either the cross-flow or in-line direction) cylinders. We identified various wake modes that can exist, depending on the cylinder motion (direction, amplitude, and frequency) by using modern methods of nonlinear dynamics. The possible responses can be period-one, periodic with large period, quasiperiodic, or chaotic. Moreover, we found that the route-to-chaos is torus breakdown. We investigated how four frequency sweeps of the cross-flow motion affect the response curves and the hysteresis phenomenon. We studied in detail the effect of the in-line motion on the wake and related this effect to the reduction in the lift and mean drag due to a synchronization type that is very different from the one due to cross-flow motion.

Dedication

I dedicate my Dissertation to my siblings:

Belal “male”

Eman “female”

Mohamed (Hamaada) “male”

Tarek “male”

Yasmine “female”

Contents

1	Introduction	1
1.1	Synopsis of the Dissertation	10
2	Computational Fluid Dynamics Simulations	12
3	Improved Models for the Lift and Drag on a Fixed Cylinder	22
3.1	Synopsis	22
3.2	Lift and Drag on a Fixed Cylinder	22
3.3	Modeling Background - Lift	25
3.4	Modeling Background - Drag	27
3.5	Motivation for Improved Lift and Drag Models	28
3.6	Improved Lift Model	29
3.7	Improved Drag Model	32
4	Improved Wake Oscillator for a Cylinder with Cross-Flow Motion	35
4.1	Synopsis	35
4.2	Analysis	36
4.3	Oscillators with External Forcing	37
4.4	Oscillators with Parametric Forcing	41
4.5	Oscillators with Mixed Forcing	42

5	Characterization of the Modes in the Wake	47
5.1	Synopsis	47
5.2	Analysis	48
5.3	Magnification of the Lift and Drag	49
5.4	Longtime Histories	52
5.5	Power Spectra	55
5.6	Phase Portraits and Poincaré Sections	59
5.7	Quasiperiodic versus Chaotic Responses	65
5.8	The Route to Chaos	69
6	A Cylinder Driven in the Cross-Flow Direction with Different Frequency-Sweep Types	71
6.1	Synopsis	71
6.2	Stationary Sweeps	72
6.3	Quasistationary Sweeps	80
6.4	Discrete Sweeps	82
6.5	Nonstationary Sweeps	84
7	Wake Changes Due to In-Line Cylinder Motion	86
7.1	Synopsis	86
7.2	In-Line Motion	87
7.3	Effects of Motion Frequency	87
7.4	Synchronization Map	94
7.5	Pre- and Post-Synchronization Modes	95
7.6	Higher-Order Spectral Analysis	105
7.7	Wake Structure and Surface Pressure	110

8 Summary and Conclusions	114
----------------------------------	------------

References	119
-------------------	------------

List of Figures

2.1	The physical domain and the used grid at a zero-displacement instant.	15
2.2	Close-up near the inner and outer boundaries of the O-type grid. . . .	16
2.3	Comparisons of the lift, drag, and mean base pressure coefficients obtained at $Re = 150$ with the results of Liu et al. (1998). Part (a) is reprinted with permission from Elsevier.	17
2.4	Comparison of the pressure coefficient C_p distribution obtained at $Re = 100$ with the LES results of Dalton (2006). Part (a) is printed with permission from Professor Charles Dalton.	18
2.5	Comparison of the wall pressure coefficient from our simulations with measurements of Norberg (1993) at $Re=200$	19
2.6	Variations of lift coefficient C_L and cross-flow motion Y with time for $A/D=0.199$ and forcing frequency equal to 1.101 times the naturel vortex-shedding frequency: (a) Stewart et al. (2005) and (b) our simulation. The solid line is for C_L and the dashed line is for Y	20
2.7	Comparison between our simulations and the measurements of Tanida et al. (1973) for the C_D component in phase with the harmonic in-line cylinder velocity $C_{D,V}$ at $Re=80$ with $A/D=0.14$	21

3.1	Time histories and corresponding power spectra of the lift and drag coefficients obtained from the CFD simulation at $Re = 500$	23
3.2	Projection of the phase portrait onto the $C_D - C_L$ plane at $Re = 500$	24
3.3	Comparisons of the steady-state time histories of the lift coefficients obtained with the CFD simulation and the improved model: (a) $Re = 300$ and (b) $Re = 500$	30
3.4	Comparisons of the steady-state time histories of the drag coefficient obtained from the CFD simulation and the improved model: (a) $Re = 300$ and (b) $Re = 500$	34
4.1	Prediction of the wake oscillator with external forcing having different amplitudes.	38
4.2	Stable solution of the forced oscillator.	39
4.3	Unstable solution of the forced oscillator.	39
4.4	Responses predicted with external acceleration-based forcing for different numbers of harmonic terms in the method of harmonic balance.	40
4.5	Frequency-response curves of wake oscillators with parametric forcing.	41
4.6	The mean (top) and amplitude (bottom) of the lift of a wake oscillator with linear parametric forcing.	42
4.7	Frequency-response curves of wake oscillators with mixed external-and-parametric velocity-based forcing (zero and positive phase β).	43
4.8	Frequency-response curves of wake oscillators with mixed external-and-parametric velocity-based forcing (zero and negative phase β).	44
4.9	Frequency-response curves of wake oscillators with mixed external-and-parametric acceleration-based forcing (zero, positive, and negative phase β).	44

4.10	Frequency-response curves of wake oscillators with mixed external-and-parametric acceleration-based forcing when $\beta = -160^\circ$	46
4.11	Frequency-response curves of wake oscillators with mixed external-and-parametric acceleration-based forcing when $\beta = -160^\circ$	46
5.1	Magnification factors of C_L and C_D within (curve without markers) and outside (curve with markers) the synchronization region.	51
5.2	Longtime history of C_L : (a) period-1 response at $F_E = 0.98$, (b) period-2 response at $F_E = 1.80$, and (c) period-3 response at $F_E = 1.40$	53
5.3	Longtime history of C_D : (a) period-1 response at $F_E = 0.98$, (b) period-2 response at $F_E = 1.80$, and (c) period-3 response at $F_E = 1.40$. The solid horizontal lines correspond to the mean values.	54
5.4	Power spectra of C_L : (a) period-1 response at $F_E = 0.98$, (b) period-2 response at $F_E = 1.80$, and (c) period-3 response at $F_E = 1.40$	56
5.5	Power spectra of C_L : (a) period-4 response at $F_E = 1.20$, (b) period-5 response at $F_E = 1.60$, and (c) period-9 response at $F_E = 0.68$	57
5.6	Power spectra of C_D : (a) period-1 response at $F_E = 0.98$, (b) period-2 response at $F_E = 1.80$, and (c) period-3 response at $F_E = 1.40$	58
5.7	Orbits in the \dot{C}_L - C_L plane: (a) period-1 response at $F_E = 0.98$, (b) period-2 response at $F_E = 1.80$, and (c) period-3 response at $F_E = 1.40$, (d) period-4 response at $F_E = 1.20$, (e) period-5 response at $F_E = 1.60$, and (f) period-9 response at $F_E = 0.68$	60

5.8 Poincaré sections of the orbits in Figure 5.7: (a) period-1 response at $F_E = 0.98$, (b) period-2 response at $F_E = 1.80$, and (c) period-3 response at $F_E = 1.40$, (d) period-4 response at $F_E = 1.20$, (e) period-5 response at $F_E = 1.60$, and (f) period-9 response at $F_E = 0.68$. The axes limits are the same as those in Figure 5.7. 61

5.9 Orbits in the C_L-C_D plane: (a) period-1 response at $F_E = 0.98$, (b) period-2 response at $F_E = 1.80$, and (c) period-3 response at $F_E = 1.40$, (d) period-4 response at $F_E = 1.20$, (e) period-5 response at $F_E = 1.60$, and (f) period-9 response at $F_E = 0.68$ 63

5.10 Poincaré sections of the orbits in Figure 5.9: (a) period-1 response at $F_E=0.98$, (b) period-2 response at $F_E=1.80$, (c) period-3 response at $F_E=1.40$, (d) period-4 response at $F_E=1.20$, (e) period-5 response at $F_E=1.60$, and (f) period-9 response at $F_E=0.68$. The axes limits are the same as those in Figure 5.9. 64

5.11 Longtime history of C_L : (a) quasiperiodic response at $F_E=0.77$, (b) quasiperiodic response at $F_E=1.00$, (c) chaotic response at $F_E=1.10$, and (d) chaotic response at $F_E=1.30$. All figures have the same time range. 67

5.12 Power spectra of C_L : (a) quasiperiodic response at $F_E=0.77$, (b) quasiperiodic response at $F_E=1.00$, (c) chaotic response at $F_E=1.10$, and (d) chaotic response at $F_E=1.30$ 68

5.13 Poincaré sections of the orbits for: (a) quasiperiodic response at $F_E=0.77$, (b) quasiperiodic response at $F_E=1.00$, (c) chaotic response at $F_E=1.10$, and (d) chaotic response at $F_E=1.30$ 69

5.14	Poincaré sections showing the transition from a quasiperiodic response to a chaotic one. The route to chaos is demonstrated by four increasing values of F_E , namely, (a) 1.00, (b) 1.02, (c) 1.06, and (d) 1.10.	70
6.1	Time histories of the displacement and lift coefficient with a stationary forcing around a frequency-stepping instant (nondimensional time = 2,400) when the smoothing method is not used.	74
6.2	Time histories of the displacement and lift coefficient with a stationary forcing around a frequency-stepping instant (nondimensional time = 2,400) when the smoothing method is used.	75
6.3	Frequency-response curves for the lift coefficient with a stationary forcing.	76
6.4	Frequency-response curves for the drag coefficient with a stationary forcing.	77
6.5	Time histories of the scaled cylinder motion (dashed line) and the lift coefficient (solid line) for type-B and type-A attractors. Each plot corresponds to a window of 20 time units.	78
6.6	Lissajous curves in the lift-displacement plane for type-B and type-A attractors. Directions of the curves are indicated.	79
6.7	Lissajous curves in the lift-drag plane for type-B and type-A attractors. Directions of the curves are indicated.	80
6.8	Frequency-response curves for the lift coefficient with a quasistationary forcing.	81
6.9	Frequency-response curves for the drag coefficient with a quasistationary forcing.	81
6.10	Frequency-response curve for the lift coefficient in the case of discrete forcing.	83

6.11	Frequency-response curve for the drag coefficient in the case of discrete forcing. The dashed lines correspond to aperiodic time histories of the drag coefficient.	83
6.12	Frequency-response curves for the lift coefficient with stationary forcing and different nonstationary forcing.	85
7.1	Calculated f_v/f_s versus f_E/f_s . Post-synchronization region is indicated by a slope of unity in the simulation results.	88
7.2	Calculated relative RMS C_L versus f_E/f_s	89
7.3	Calculated relative $\langle C_D \rangle$ versus f_E/f_s	89
7.4	Calculated relative RMS $C_{D,osc}$ versus f_E/f_s	90
7.5	Calculated and fitted relative synchronized RMS C_D versus f_E/f_s . . .	90
7.6	Variation of the mechanical work W_{cyc} with f_E/f_s	91
7.7	Variation of the phase angle ψ of the synchronized C_D with f_E/f_s . . .	92
7.8	Calculated relative P_{avg} versus f_E/f_s	93
7.9	Calculated and fitted relative P_{avg} for the synchronized cases versus f_E/f_s	93
7.10	Locus of the critical f_E in the $(A/D) - (f_E/f_s)$ plane.	94
7.11	Loci of the critical f_E in the $(A/D) - (f_E/f_s)$ plane at $Re=500$ (solid line) and $Re=300$ (dashed line). The threshold (A/D) is indicated by a solid circle.	95
7.12	Poincaré sections of nonsynchronized C_L : i) $f_E/f_s=0.4$, ii) $f_E/f_s=0.72$, iii) $f_E/f_s=0.73$, and iv) $f_E/f_s=1.7$	97
7.13	Poincaré sections of nonsynchronized C_D : i) $f_E/f_s=0.4$, ii) $f_E/f_s=0.72$, iii) $f_E/f_s=0.73$, and iv) $f_E/f_s=1.7$	98
7.14	Steady-state C_L and C_D versus time for $f_E/f_s=1.7$	99

7.15	Steady-state C_L and C_D versus time for $f_E/f_s=1.81$	99
7.16	Poincaré sections of C_L and C_D for $f_E/f_s=1.81$	100
7.17	Poincaré sections of C_L and C_D for cross-flow motion at $f_E/f_s=1$. . .	100
7.18	Spectra of C_L and C_D at $f_E/f_s=1.7$	101
7.19	Spectra of C_L and C_D at $f_E/f_s=1.81$	102
7.20	Spectra of C_D and C_L for cross-flow motion at $f_E/f_s=1$	103
7.21	Steady-state C_T and β_T for cross-flow motion at $f_E/f_s=1$	104
7.22	Steady-state C_T and β_T versus time for $f_E/f_s=1.81$	104
7.23	Magnitude-squared cross-bicoherence for $f_E/f_s=1.7$	106
7.24	Magnitude-squared cross-bicoherence for $f_E/f_s=1.81$	106
7.25	Magnitude-squared cross-bicoherence b_{LLD}^2 for cross-flow motion at $f_E/f_s=1$	107
7.26	Absolute of cross-power spectrum $ M_{LD} $ for $f_E/f_s=1.7$	108
7.27	Absolute of cross-power spectrum $ M_{LD} $ for $f_E/f_s=1.81$	109
7.28	Absolute of cross-power spectrum $ M_{LD} $ for cross-flow motion at $f_E/f_s=1$.	109
7.29	Vorticity contours when $X=0$ for synchronized cases: i) $f_E/f_s=1.81$ and ii) $f_E/f_s=3$. Positive (counterclockwise) vortex is being shed from the bottom surface.	110
7.30	Surface distribution of $\langle C_P \rangle$ for synchronized cases: i) $f_E/f_s=1.81$ and ii) $f_E/f_s=3$. The angle θ is 0 at the stagnation point and 90° at the top point.	111
7.31	Surface distribution of C_P over one motion cycle for $f_E/f_s=1.81$. The motion sequence is: i) $X=0$ and \dot{X} is maximum, ii) X is maximum and $\dot{X}=0$, iii) $X=0$ and \dot{X} is minimum, and iv) X is minimum and $\dot{X}=0$	112

List of Tables

3.1	Lift parameters at different Reynolds numbers.	29
3.2	Drag parameters at different Reynolds numbers.	33

Chapter 1

Introduction

The wake of a fixed body with a long span is characterized by a line of shed vortices (known as von Kármán vortex street) in wake. The exerted hydrodynamic or aerodynamic force on the body due to these variations in the wake is alternating and can cause considerable fatigue and eventually damage. The exerted force is often resolved into drag and lift components in the in-line and cross-flow directions, respectively. The small eddies that can be observed behind a plant stem in a river and the large alternating wind circulations in the lee of a mountain in isolated islands are examples of this phenomenon but with very different scales. This phenomenon is encountered also in high-rise buildings, chimneys, towers of wind turbines, launch vehicles on launch pads, and spars and risers used in the oil and gas industry.

Shedding-control (or anti-shedding) devices are needed to minimize the shedding intensity and protect the body. Helical strakes are commonly used to alleviate this vortex shedding (Medici, 2004; Constantinides and Oakley, 2006). These devices were proposed to mitigate the alternating wind loads on Saturn V due to vortex shedding while the vehicle is being transported to the launch pad or while it is on it (Barret, 1996). Helical strakes and twisted pairs of cable disrupt the spanwise coherence.

Other devices are used to suppress vortex shedding through introducing disturbances at the surface of the body, which interact properly with the vortex shedding (Sarpkaya and Isaacson, 1981; Blevins, 1990). For example, streamlined fairings influence the boundary-layer separation, and hair fairings and ribbons disrupt the vortex formation length. Recent studies proposed the use of roughness distributions (Bernitsas and Raghavan, 2008) or pivoted plates (Assi and Bearman, 2008) to suppress vortex shedding.

A circular cylinder is a favored configuration in many studies because of its geometric simplicity and because near-cylinder elements are used in several industrial applications. Furthermore, unlike square cylinders, galloping does not occur behind a circular cylinder (Di Silvio et al., 1975; Sarpkaya, 1978). This minimizes the effects of geometric parameters on the shedding in the wake. Many studies have been performed to understand and model the phenomena associated with the shedding problem for fixed and moving cylinders (rigid as well as flexible).

The problem of a cylinder vibrating due to forces exerted by the wake goes back to the work of Strouhal (1878) in aeroacoustics, which lead to the designation of the Strouhal number to represent the nondimensional shedding frequency, and to the work of Rayleigh (1879) on the oscillations of violin strings subject to incoming wind. However, Birkhoff and Zarantonello (1957) were the first to suggest an oscillator to model the wake of a cylinder, describing it as “swinging from side to side, somewhat like the tail of a swimming fish”. They did not specify a particular oscillator but alluded to a linear one. Seven years later, Bishop and Hassan (1964) performed experiments on a cylinder oscillating harmonically in the cross-flow direction, covering a range of Reynolds numbers from 5,850 to 10,800. The cylinder motion was adjusted via a Scotch-yoke mechanism. When the frequency of the cross-flow motion is close to

the natural vortex-shedding frequency, the wake responded at the motion frequency and not at the natural vortex-shedding frequency, and the wake is said to synchronize with the cylinder motion. The response within the synchronization band was examined for different motion amplitudes. They reported that the width of this band decreases as the Reynolds number increases. Based on these experiments, Bishop and Hassan proposed that the synchronized wake can be modeled by a simple forced oscillator. However, they did not specify a particular oscillator (which they called “wake” or “fluid” oscillator), but indicated that it is nonlinear and self-excited.

Since then, several models have been proposed for the wake of a fixed cylinder (Hartlen and Currie, 1970; Blevins, 1974; Balasubramanian and Skop, 1996; Nayfeh et al., 2003) and an elastically-mounted cylinder (Hartlen and Currie, 1970; Skop and Griffin, 1973 and 1975; Griffin et al., 1973; Skop, 1974; Iwan and Blevins, 1974; Landl, 1975; Currie and Turnball, 1987; Krenk and Nielsen, 1999; Mureithi et al., 2001; Facchinetti et al., 2004). Each model is a nonlinear ordinary-differential equation, which when integrated in time, can yield the correct history of the lift coefficient.

Two candidate oscillators have been commonly used so far for the lift force on a cylinder in a uniform flow: the Rayleigh oscillator (e.g., Hartlen and Currie, 1970; Mureithi et al., 2001) and the van der Pol oscillator (e.g., Facchinetti et al., 2004; Nayfeh et al., 2003; Modarres-Sadeghi et al., 2008). Both are self-excited, self-limiting nonlinear oscillators with cubic nonlinearity. Griffin et al. (1973) and Krenk and Nielsen (1999) proposed a combination of these two oscillators, whereas Landl (1975) proposed a variant of the van der Pol oscillator with an additional quintic term. Nayfeh et al. (2003) concluded that the van der Pol oscillator should be used to model the lift exerted on a fixed cylinder because this oscillator produces a phase angle between the main lift component and its third harmonic that is closer to that obtained from

numerical simulations of the Reynolds-averaged Navier-Stokes equations (RANS) for a wide range of Reynolds numbers.

The quality of a model is gauged by its capability to capture qualitatively and quantitatively the important physical phenomena recorded in experiments or full simulations of the flow (e.g., by solving the Navier-Stokes equations). Examining the problem of synchronized wakes of moving cylinders in the cross-flow direction shows that the wake exhibits abrupt changes as one of the problem parameters changes (e.g., the free-stream velocity, the natural cylinder frequency, forcing frequency and amplitude). This leads to discontinuous frequency-response curves with two branches, each one corresponds to a separate synchronized-wake mode. Common wake oscillators for the exerted lift on a moving cylinder are unable to capture this physical multi-valuedness characteristic. As a critical parameter is crossed, an existing stable periodic wake configuration loses stability, giving way to another stable configuration. Some existing models replace the multi-valued lift response by a single-valued one with rapid change (e.g., Hartlen and Currie, 1970) and some capture one branch only (e.g., Landl, 1975).

Whereas there are some differences between forced and elastically-mounted cylinders, both exhibit the synchronization phenomenon. Several researchers support the idea of analogy between the two situations and suggest using the results of the forced case to understand the elastically-mounted case (Iwan and Blevins, 1974; Zdravkovich, 1982; Botelho, 1983; Wu, 1989; Moe and Wu, 1990; Dahl et al., 2008). At least qualitatively, the lift exerted on a forced cylinder can be used to predict the amplitudes and frequencies of the vortex-induced vibration (VIV) of elastically-mounted cylinders. In this Dissertation, we restrict our attention to a forced cylinder.

For the wake of a fixed cylinder, there is a single parameter characterizing the problem,

namely, the Reynolds number. For a forced cylinder, two extra parameters are needed to describe the cylinder motion; its nondimensional amplitude and frequency. Some studies (e.g., Williamson, 1985; Ibrahim, 2005) used another nondimensional group, namely, the Keulegan-Carpenter number (KC) defined by $KC \equiv \frac{U_{max}}{fD}$, where U_{max} is the maximum wave speed, D is the cylinder diameter, and f is the wave frequency. It was introduced by Keulegan and Carpenter (1958) who performed experiments on a vertical cylinder and a flat plate subject to standing water waves; they measured the hydrodynamic-mass and hydrodynamic-drag coefficients for different wave patterns. They found that these coefficients do not depend on the ‘oscillation-based’ Reynolds number, but on the KC number.

In the case of a cylinder oscillating in a uniform stream, U_{max} and f correspond to the motion of the cylinder rather than the fluid. With sinusoidal motion of the type

$$y = A \sin(2\pi f t) \tag{1.1}$$

one can show that KC becomes $2\pi A/D$, and hence it is an alternate way for describing the oscillation amplitude. We do not use it here.

Williamson and Roshko (1988) performed an experimental study for a cylinder undergoing harmonic cross-flow motion in a Reynolds number range from 300 to 1,000. They used aluminum particles on the fluid surface to visualize the flow. They used the nondimensional wavelength λ/D of the cylinder motion and its nondimensional amplitude A/D as the control parameters. They reported different vortex patterns in the $(\lambda/D, A/D)$ plane, which was divided into areas covering different synchronized and nonsynchronized wake configurations.

Gu et al. (1994) also studied experimentally the structure of the near wake of a cylinder oscillating harmonically in the cross-flow direction. They used particle imaging to visualize the streamline patterns and vorticity distributions. The instantaneous

structure of the near wake was determined using particle tracking velocimetry (PTV) and particle image velocimetry (PIV). They considered low and moderate Reynolds numbers of 185 and 5,000 and a nondimensional motion amplitude of 0.2. They observed vorticity switching in the wake as the motion frequency increases. This switching is not significantly altered by the presence of small-scale Kelvin-Helmholtz vortices that coexist with the large-scale (Kármán) vortices.

Carberry et al. (2001) experimentally investigated the wake of a cylinder oscillating in the cross-flow direction with a nondimensional amplitude of 0.5 and a Reynolds number of 2,300. The motion was implemented via a stepper motor system. They concluded that the interaction between the instability waves in the wake and the motion of the cylinder leads to a transition from one mode to another. This interaction depends strongly on the ratio of the motion frequency to the natural vortex-shedding frequency. A jump in the lift force was observed within the synchronization band. A corresponding jump in the phase of the lift relative to the motion was also observed. Dong et al. (2004) and Dong and Karniadakis (2005) solved the three-dimensional Navier-Stokes equations using direct numerical simulation (DNS) to capture the flow field around a fixed and a driven cylinder in the cross-flow direction with a length-to-diameter ratio of π with a nondimensional motion amplitude of 0.3 at a moderate Reynolds number of 10,000. They used the spectral element method with 300 million degrees of freedom, which reflects a tremendous resolution of the grid as required by the DNS for this Reynolds number. Different polynomial orders were used, ranging from 5 to 8. The resolved domain extended 20 diameters upstream and 50 diameters downstream, with a cross-flow dimension of 40 diameters. The problem was solved in a coordinate system attached to the cylinder. Good agreement with some experimental data (Bishop and Hassan, 1964; Gopalkrishnan, 1993; Williamson, 1996; Norberg,

2003) was observed.

Facchinetti et al. (2004) modeled the VIV problem by coupling van der Pol oscillator for the lift with a linear oscillator for the cylinder motion. Three types of wake forcing were investigated: displacement, velocity, and acceleration forcings. Comparing the outcomes of the model with some experimental results for forced cylinder (Vickery and Watkins, 1962; Bishop and Hassan, 1964; King, 1977; Griffin, 1980; Pantazopoulos, 1994), they concluded that the acceleration forcing matches the data better than the other two. Then, they investigated the dynamical behavior of the three forced oscillators as the reduced velocity is varied in a nonstationary fashion. We note that there are several limitations in their study. First, the model is based on a constant Strouhal number and constant amplitude of the lift of the fixed cylinder, regardless of the Reynolds number. Second, the selected forced-cylinder data used to predict the van der Pol parameters exhibit large dispersion. Third, the proposed model cannot capture the 180° -jump in the phase between the displacement and the lift. Fourth, tuning the forced-oscillator parameters based on a certain set of recorded data and then using the same parameters to model the VIV problem at a different Reynolds number may be questionable because, if the VIV is inhibited, the lift model (which automatically reduces to a free-oscillator) would not be able to reproduce the limit cycle of the lift.

Kaiktsis et al. (2007) numerically studied the forces exerted on a cylinder driven harmonically in the cross-flow direction at a Reynolds number of 400. They solved the two-dimensional Navier-Stokes equations in a coordinate system fixed to the cylinder. The spectral element method was used with polynomial functions of order 9. The domain extended 20 diameters upstream, 60 diameters downstream, and 34 diameters in the cross-flow direction. They considered the cases when the the motion frequency

is set equal to, lower than, and higher than the natural vortex-shedding frequency. Therefore, they considered discrete frequencies of motion and did not examine the frequency-response curves. In their analysis, the lift force was decomposed into a component in phase with the velocity and a component 180° out of phase with the acceleration. Variations of these components, along with other flow parameters were examined over a range of nondimensional motion amplitudes from 0 to 0.6 for the three forcing cases. Smooth variations of the force coefficients and regular vortex patterns were found when the motion frequency was below the natural vortex-shedding frequency. Sharp changes in the force coefficients were found when the motion frequency was above the natural vortex-shedding frequency.

Ogink and Metrikine (2008) claimed that the component of the lift in phase with the acceleration has linear correlation with the forcing amplitude (i.e., the acceleration amplitude, thus the motion amplitude) in the experiments of Gopalkrishnan (1993) with a cylinder forced in the cross-flow direction at a Reynolds number of 10,000, which is not satisfied by the classical forced van der Pol model. Hence, they started from where Facchinetti et al. (2004) ended (i.e., the acceleration-forcing van der Pol) and modified the cubic term from $q^2\dot{q}$ to $1/(a + b q^2)\dot{q}$, where a and b ($a < 1$) are model-tuning parameters, and q is the model variable representing the ratio of the lift amplitude for the elastically mounted cylinder (under lock-in conditions) and the lift amplitude for the fixed cylinder needs to be changed. There are multiple concerns with this study. First, the experimental data do not in fact show strong linear correlation with the forcing amplitude as suggested by the figure made by Ogink and Metrikine (based on the measurements of Gopalkrishnan). Second, the modified model does not reasonably reproduce the linear correlation on which it was justified. Third, the results of the modified model do not compare well with the

experiments with elastically mounted cylinders of Khalak and Williamson (1999) and Feng (1968) in terms of capturing the multi-valuedness, lock-in range, and hysteresis. Fourth, as mentioned earlier, the idea of tuning the model parameters based on a set of data corresponding to a certain Reynolds number and then using them at a different Reynolds number leads to mismatching in modeling the free-wake case.

For studies of a one-degree-of-freedom moving cylinder, usually the transverse motion is considered and in-line motion is restrained because some studies show that induced in-line motion is one order of magnitude smaller than the transverse motion (Vandiver, 1987; Torum et al., 1996). Tanida et al. (1973) studied a one-degree-of-freedom cylinder oscillating harmonically in the in-line direction. The first part of their study considered a single circular cylinder oscillating in a uniform stream, whereas the second part was dedicated to the case of a cylinder oscillating in the wake of another cylinder (i.e., tandem cylinders). In both parts, they measured the lift and drag forces on the oscillating cylinder and observed the synchronization phenomenon regardless of the existence of the upstream fixed cylinder. For the in-line oscillation case, the cylinder was made to oscillate harmonically with an amplitude equal to 14% of its diameter. Whereas the amplitude was kept constant, the frequency was varied from below to above the natural vortex-shedding frequency (or Strouhal frequency according to their terminology). Each experiment corresponded to a single frequency. Individual experiments lasted for at least 20 s, which was long enough for the transient to decay and the steady state to develop. The effects of end plates were minimized by having a proper setup, including a large liquid tank relative to the cylinder diameter and low turbulence with high uniformity of the velocity distribution along the span of the cylinder. They reported that, during synchronization, the fluctuating lift ‘vanishes’; its magnitude drops to very small levels. They related

this to a positive aerodynamic damping induced by the cylinder oscillation, and to the work done by the drag force.

Kim and Williams (2006) measured the lift and drag forces on a cylinder driven harmonically in the in-line direction in air at a Reynolds number of 15,200. The cylinder diameter was 50.8 mm and its length was 610 mm. End plates were 510 mm apart so the aspect ratio was 10. A printed circuit motor connected to a Scotch-yoke mechanism was used to control the motion. The main part of the experiment was conducted at a very small oscillation amplitude of 3.5% of the diameter. Also, the motion frequency was 0.8 the natural vortex-shedding frequency. This is far beyond the synchronization in case of in-line motion. Their goal was to study the nonlinear coupling between the lift and drag. Whereas their study revealed interesting facts about this nonlinear interaction and explained the structure of the power spectra, fixing the frequency at a single value did not allow synchronization to take place. It also did not show how this force coupling changes for different frequencies.

1.1 Synopsis of the Dissertation

We followed computational and analytical approaches in this Dissertation. The analysis and results are presented as follows. We start with a description of the CFD simulation of the flow field. Then, we present the models proposed for the lift and drag coefficients on a cylinder. Next, we use modern methods of nonlinear dynamics to characterize the wake responses within and outside the synchronization (or lock-in) band due to cross-flow motion and study the route to chaos. After that, we examine how the lift and drag coefficients are affected by the manner in which the frequency of the cross-flow motion is varied: stationary, quasi-stationary, discrete, or

nonstationary. Finally, we examine the case of in-line motion and the associated lift suppression, instantaneous wake symmetry, and mean drag drop, which take place at a critical motion frequency, and the dependence of that frequency on the Reynolds number and motion amplitude. We also use higher order spectral methods to analyze the coupling between the lift and drag below and above that frequency and compare several features of the synchronization due to in-line motion to that due to cross-flow motion.

Chapter 2

Computational Fluid Dynamics

Simulations

The fluid is assumed to be incompressible and two-dimensional. Its motion is governed by the Navier-Stokes equations

$$\nabla \cdot \vec{u} = 0 \tag{2.1}$$

$$\frac{\partial}{\partial t} \vec{u} + \vec{u} \cdot \nabla \vec{u} = -\frac{1}{\rho} \nabla p + \nu \nabla^2 \vec{u} \tag{2.2}$$

To avoid the computational difficulties resulting from the poor coupling between the continuity and momentum equations, Equations (2.1, 2.2), for incompressible fluids, we use the artificial-compressibility method (Chorin, 1967; Soh and Goodrich, 1988; Rogers et al., 1991) and improve the coupling between the pressure and velocity fields by adding pseudo local time-derivative terms to both the continuity and momentum equations. Nayfeh et al. (2003) used this method to solve the flow over a fixed cylinder over a very wide range of Reynolds numbers, and Owis and Nayfeh (2001, 2004) used it and solve multi-phase flows over axisymmetric projectiles. In vector form, and with arbitrary Lagrange-Euler description, the governing equations become

$$\frac{\partial}{\partial t} \vec{\tilde{q}} + \frac{\partial}{\partial \tau} \vec{q} + \frac{\partial}{\partial x} (\vec{E} - \vec{E}_v) + \frac{\partial}{\partial y} (\vec{F} - \vec{F}_v) = 0 \quad (2.3)$$

where

$$\vec{\tilde{q}} = \begin{pmatrix} 0 \\ u \\ v \end{pmatrix}; \quad \vec{q} = \begin{pmatrix} p \\ u \\ v \end{pmatrix}; \quad \vec{E} = \begin{pmatrix} \rho \hat{\beta} u \\ u(u - u_g) + p \\ u v \end{pmatrix}; \quad \vec{F} = \begin{pmatrix} \rho \hat{\beta} v \\ u v \\ v(v - v_g) + p \end{pmatrix}$$

$$\vec{E}_v = \nu \begin{pmatrix} 0 \\ 2 \frac{\partial u}{\partial x} \\ \frac{\partial u}{\partial y} + \frac{\partial v}{\partial x} \end{pmatrix}; \quad \vec{F}_v = \nu \begin{pmatrix} 0 \\ \frac{\partial u}{\partial y} + \frac{\partial v}{\partial x} \\ 2 \frac{\partial v}{\partial x} \end{pmatrix}$$

where u_g and v_g are the velocity components of the grid points in the x and y directions, respectively. The original continuity equation, Equation (2.1), is elliptic in space, whereas the modified continuity equation is elliptic in space but hyperbolic in pseudo-time. The pseudo wave speed $\sqrt{\hat{\beta}}$ provides a mechanism for propagating information throughout the domain and drives the divergence of the velocity towards zero at each time step through sub-iterations in the pseudo time τ . Unlike the semi-implicit method for pressure-linked equations (SIMPLE) of Patankar and Spalding (1972), no terms are neglected from the differential operator (Fletcher, 1991). The value of $\hat{\beta}$ controls how fast the pseudo terms vanish and the original equations, Equations (2.1, 2.2), are restored. Examining numerical studies that have employed the artificial-compressibility method shows that $\hat{\beta}$ can vary by orders of magnitude (Muldoon and Acharya, 2007). Some studies chose $\sqrt{\hat{\beta}}$ to be close to a dominant

convective velocity in the problem (Marx, 1994). However, there is no universal optimum value for $\hat{\beta}$. Rather, it depends on the problem configuration, grid resolution, and time step. We fix $\hat{\beta}$ at $4.0 U_\infty^2$ in all of our simulations. We examined different (smaller and larger) values of $\hat{\beta}$ and found that this value is very reasonable in terms of the rate of convergence at the sub-iteration level.

The modified governing equations are first nondimensionalized using the cylinder diameter D as a reference length, the free-stream velocity U_∞ as a reference velocity, and ρU_∞^2 as a reference pressure, where ρ is the fluid density. They are then transformed into curvilinear body-fitted coordinates and integrated over an O-type grid. We use second-order central differencing in space for the viscous terms and an upwind scheme for the inviscid terms. We use a second-order three-level implicit scheme for time integration. The algebraic system of equations is solved using the line-relaxation scheme. The continuity and momentum equations are solved simultaneously, resulting in block tridiagonal systems. This is different from the sequential approach used in other methods, such as the marker-and-cell (MAC) of Harlow and Welch (1965). The physical domain and structured grid are shown in Figure 2.1. The near-boundary cells are shown in Figure 2.2. There are 150 points along the quasi-radial direction and 150 points along the quasi-angular direction. The quasi-angular spacing is uniform. A total of 150 points are distributed on either the inner boundary of the grid (the cylinder surface) or the outer boundary of the grid (whose radius is $25 D$). These points are connected by straight quasi-radial lines at each time step, and 150 grid points are distributed along each of them. The spacing along these lines is nonuniform and a single-parameter stretching function is used, which is a generalized form of the one used by Al-Jamal and Dalton (2004). For grid points with radial index i and

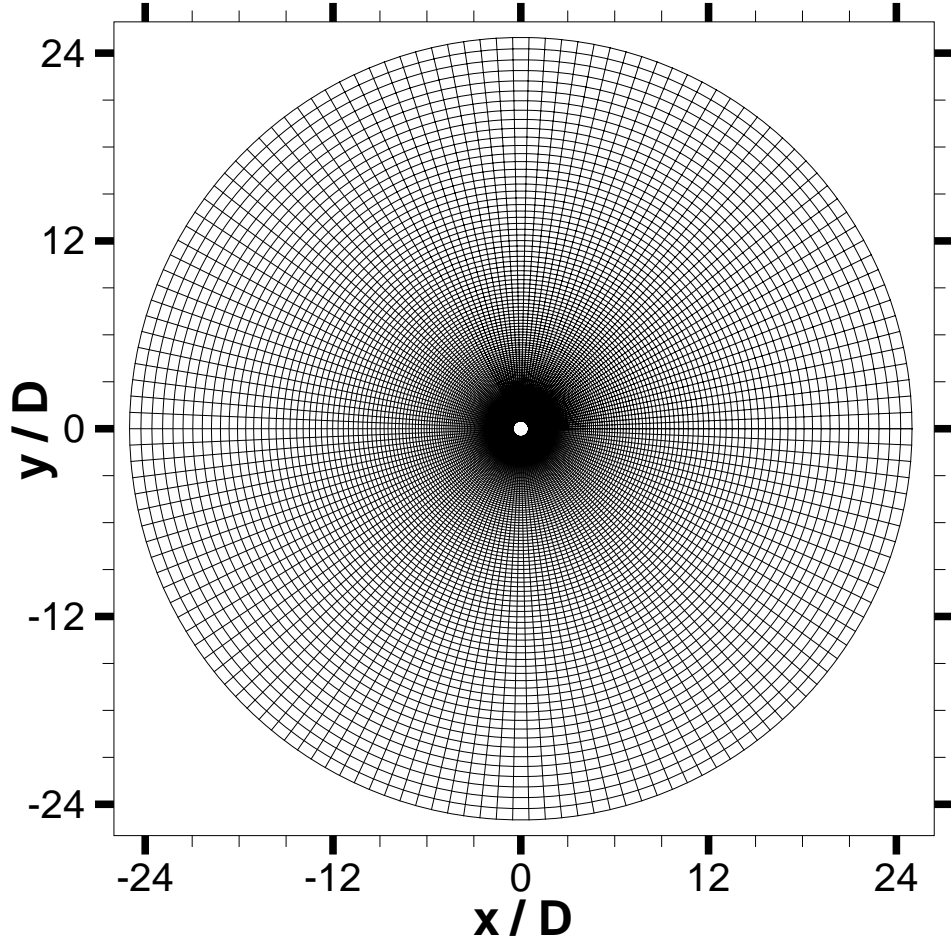


Figure 2.1: The physical domain and the used grid at a zero-displacement instant.

angular index j , the distance from the cylinder surface is obtained from

$$d(i, j)/D = a (e^{(i-1) \Delta\xi(j)} - 1) \quad (2.4)$$

where ξ is the transformed quasi-radial coordinate, $\Delta\xi(j)$ is the uniform ξ spacing along the j -th quasi-radial line, and a is the stretching parameter. At the cylinder surface, $\xi(i = 1, j) = 0$ and $d(i = 1, j) = 0$. For a fixed cylinder, the grid is not deformed and the quasi-radial and quasi-angular lines become radial lines and co-centric circles, respectively, forming a polar orthogonal grid. The first radial spacing (at the cylinder) is $0.009 D$, which increases to $0.724 D$ in the far field. As a increases, the spacing

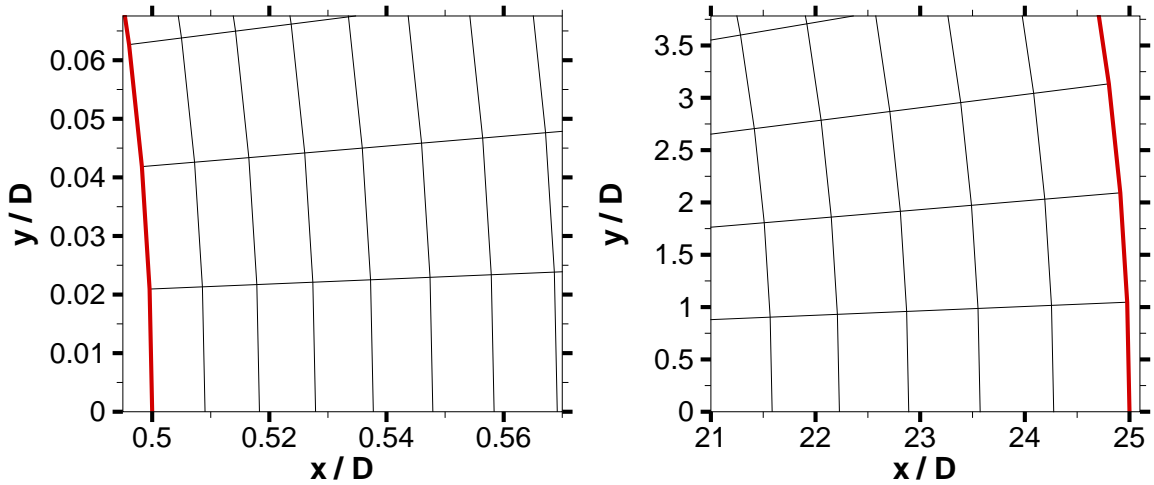


Figure 2.2: Close-up near the inner and outer boundaries of the O-type grid.

near the cylinder decreases, whereas the spacing near the outer boundary decreases. To avoid extremely elongated cells and to keep the first radial spacing below $0.01 D$, we set a equal to 0.3. Lower values cause the near-surface cells to be very stretched, whereas larger values cause the near-surface resolution to decrease beyond the desired level.

We model the turbulence scales using an eddy viscosity. We tried both of the Baldwin and Barth (1990) and the Spalart and Allmaras (1992) models and found that the former gives better results for the fixed cylinder, whereas the latter overpredicts the mean of the drag coefficient. Also, the Baldwin and Barth model is simpler and easier to implement. It is suitable for both internal and external flows (Brown et al., 2006). The Baldwin and Barth model is also a reasonable compromise between the two-equation models, which are more expensive and sometimes their results are in less agreement with experiments (Campioli, 2005) and the algebraic ones, which are acceptable only for attached wall-bounded flows (Wilcox, 2001). Since we limit most of our simulations to low Reynolds numbers (Re 500 and below), the turbulence levels

are small, thus the choice of the turbulence model is not critical.

At the inflow region, a uniform horizontal flow is applied. At the outflow region, the pressure is set equal to the free-stream value, whereas the velocities are extrapolated from the interior domain. At the cylinder surface, no-slip and no-penetration conditions are applied so that there is no relative motion between the cylinder and the fluid at the surface. This leads to continuous coupling between the exciting motion and the flow field, where the cylinder velocity is applied as a boundary condition at the grid points forming the cylinder. Because the motion is specified, the exact cylinder velocity is computed at each time step without any lagging and without the need of a predictor-corrector algorithm.

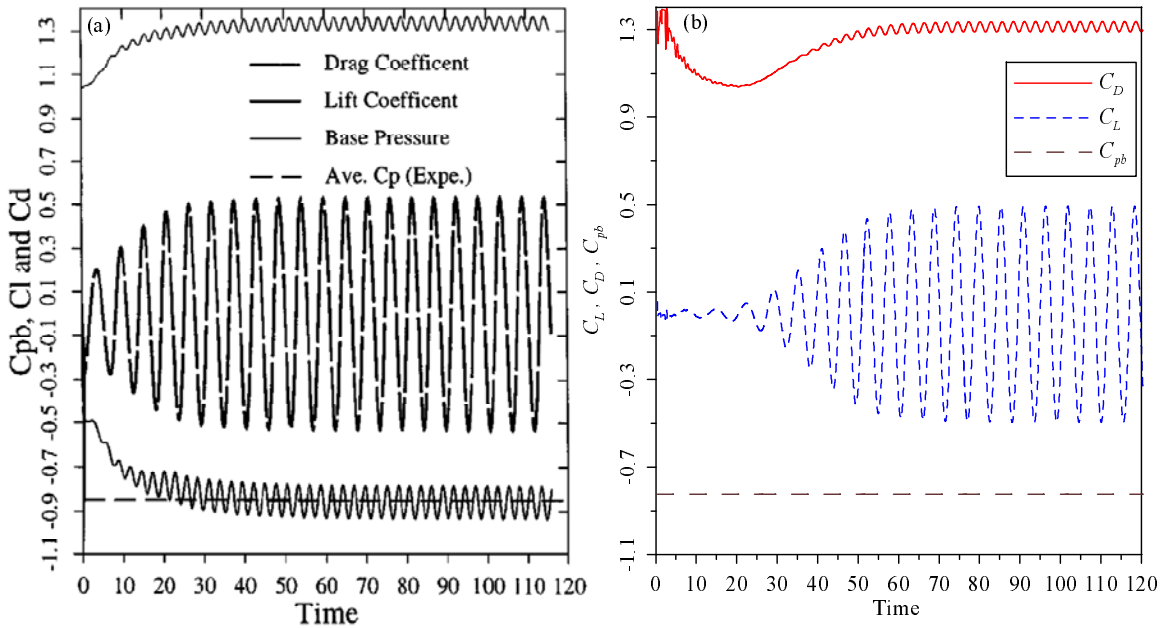


Figure 2.3: Comparisons of the lift, drag, and mean base pressure coefficients obtained at $Re = 150$ with the results of Liu et al. (1998). Part (a) is reprinted with permission from Elsevier.

In previous studies (e.g., Marzouk et al., 2007; Marzouk and Nayfeh, 2008a), we

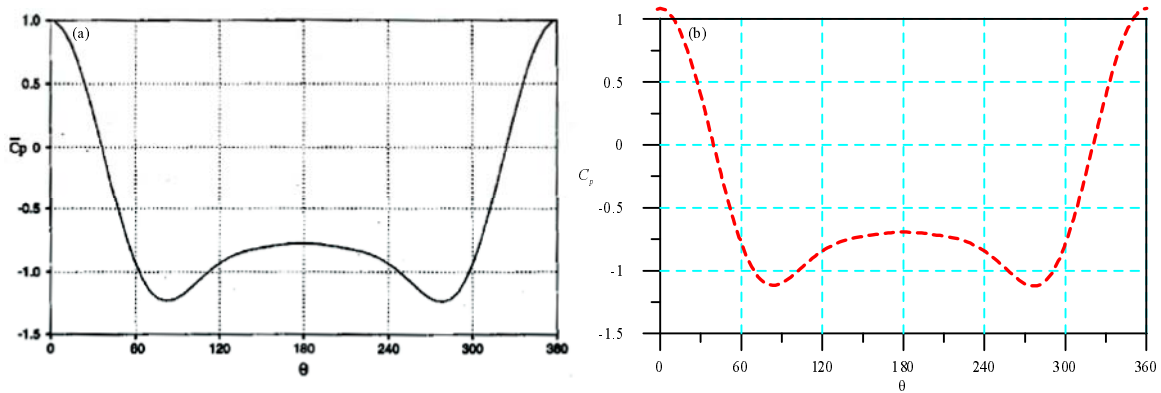


Figure 2.4: Comparison of the pressure coefficient C_p distribution obtained at $Re = 100$ with the LES results of Dalton (2006). Part (a) is printed with permission from Professor Charles Dalton.

validated the simulation against several experimental and numerical results. In Figure 2.3, we compare our results at $Re = 150$ with the results of Liu et al. (1998), who simulated the laminar flow over a cylinder using also the artificial compressibility approach. There is good agreement between our results and theirs for the histories of the lift and drag coefficients, C_L and C_D , as well as the mean base pressure C_{Pb} . The latter agrees well with the experiments of Williamson and Roshko (1990). In Figure 2.4, we compare the distribution of the pressure coefficient at $Re=100$ with that obtained by Dalton (2006) using LES simulations. The two solutions match quite well with each other.

Figure 2.5 shows the distribution of the wall pressure coefficient at $Re=200$ and 400 for a fixed cylinder; they are in good agreement with the experiments of Norberg (1993). In the experiments, the pressure fluctuations were measured with an Endevco 8507C miniature pressure transducer using a 2-mm diameter cylinder with 10-mm end plate diameter.

We also validate our simulations against some results of Stewart et al. (2005), who

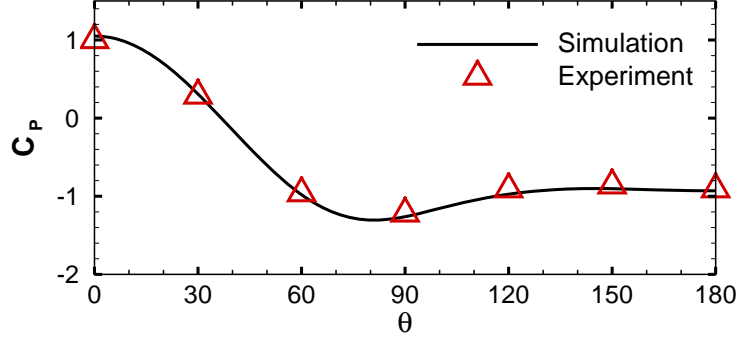


Figure 2.5: Comparison of the wall pressure coefficient from our simulations with measurements of Norberg (1993) at $Re=200$.

used the spectral element method to solve the two-dimensional Navier-Stokes equations for the flow over an oscillating cylinder in the cross-flow direction at $Re=200$. They used a C-type mesh, which extended from 15 diameters upstream to 23 diameters downstream and had a semi-width of 15 diameters. These dimensions are comparable to ours, but our O-type mesh is larger, which minimizes the blockage effect. They used Lagrangian interpolating polynomials of eighth order and found that the nondimensional natural vortex-shedding frequency to be 0.198, which is close to our value of 0.192 at the same Re . In fact, our value is closer to the measured value 0.190 of Kovasznay (1949), and 0.189 of Roshko (1953). In Figure 2.6, we compare the time history of our computed C_L with that of Stewart et al. for $A/D=0.199$ and forcing frequency equal to 1.101 times the natural vortex-shedding frequency. Clearly, there is good agreement not only in the magnitude of C_L , but also in the phase between the displacement Y and C_L .

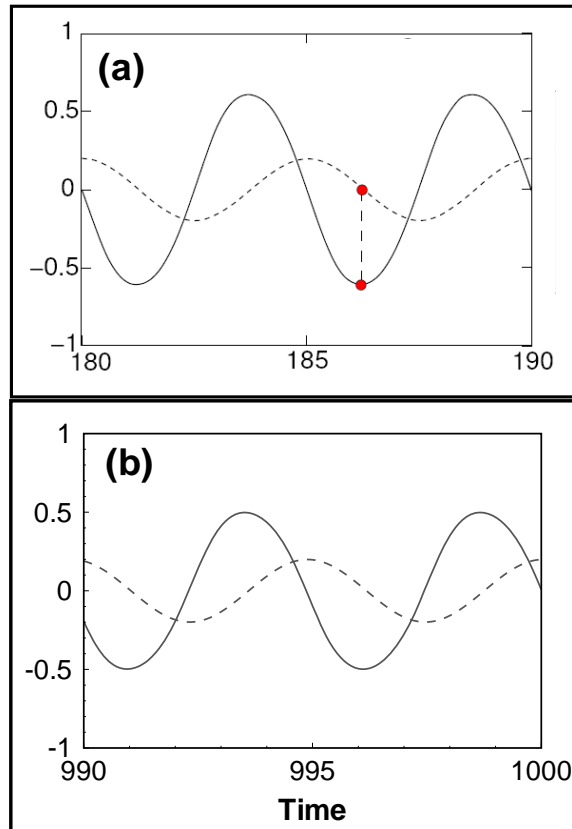


Figure 2.6: Variations of lift coefficient C_L and cross-flow motion Y with time for $A/D=0.199$ and forcing frequency equal to 1.101 times the natural vortex-shedding frequency: (a) Stewart et al. (2005) and (b) our simulation. The solid line is for C_L and the dashed line is for Y .

We compare our simulations with the reported experimental data of Tanida et al. (1973) for a cylinder oscillating harmonically in the in-line direction. Their experiments were conducted in oil at $Re=80$, with an in-line motion amplitude of 14% of the cylinder diameter. To reduce three-dimensionality effects, measurements were taken at the central section of the test cylinder. Figure 2.7 shows the component of the drag coefficient C_D in phase with the velocity of the in-line motion as a function of the nondimensional motion frequency f_E . Again, there is good agreement between our simulations and the measurements.

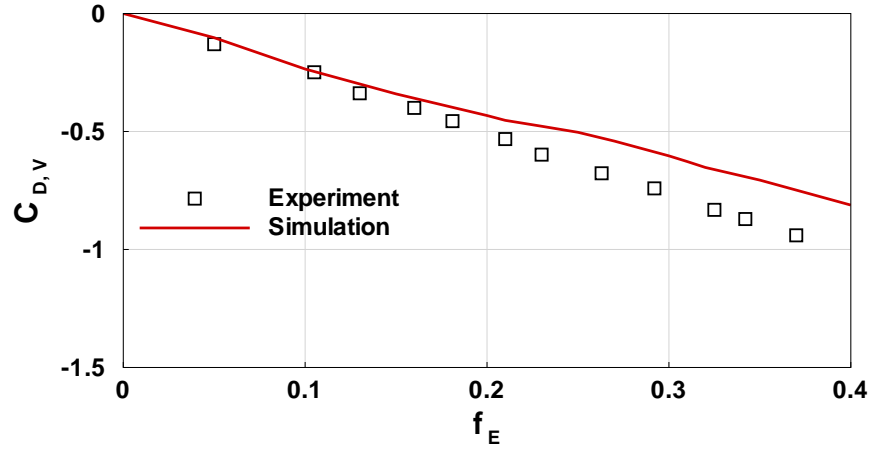


Figure 2.7: Comparison between our simulations and the measurements of Tanida et al. (1973) for the C_D component in phase with the harmonic in-line cylinder velocity $C_{D,V}$ at $Re=80$ with $A/D=0.14$.

Chapter 3

Improved Models for the Lift and Drag on a Fixed Cylinder

3.1 Synopsis

This chapter presents an improved wake oscillator to model the lift coefficient on a fixed cylinder in a uniform stream. A quadratic algebraic equation is also proposed to relate the drag coefficient to the lift coefficient. Unlike previously-proposed models, the developed model captures not only the basic features of the wake, such as the frequency and amplitude of the lift and drag, but also detailed features, such as the phase angle between the lift and drag.

3.2 Lift and Drag on a Fixed Cylinder

It is very useful to start by examining the typical behavior of the lift and drag coefficients. This will facilitate the rest of the discussion in this chapter. Figure 3.1 shows time histories and corresponding power spectra (magnitude power) of C_L and

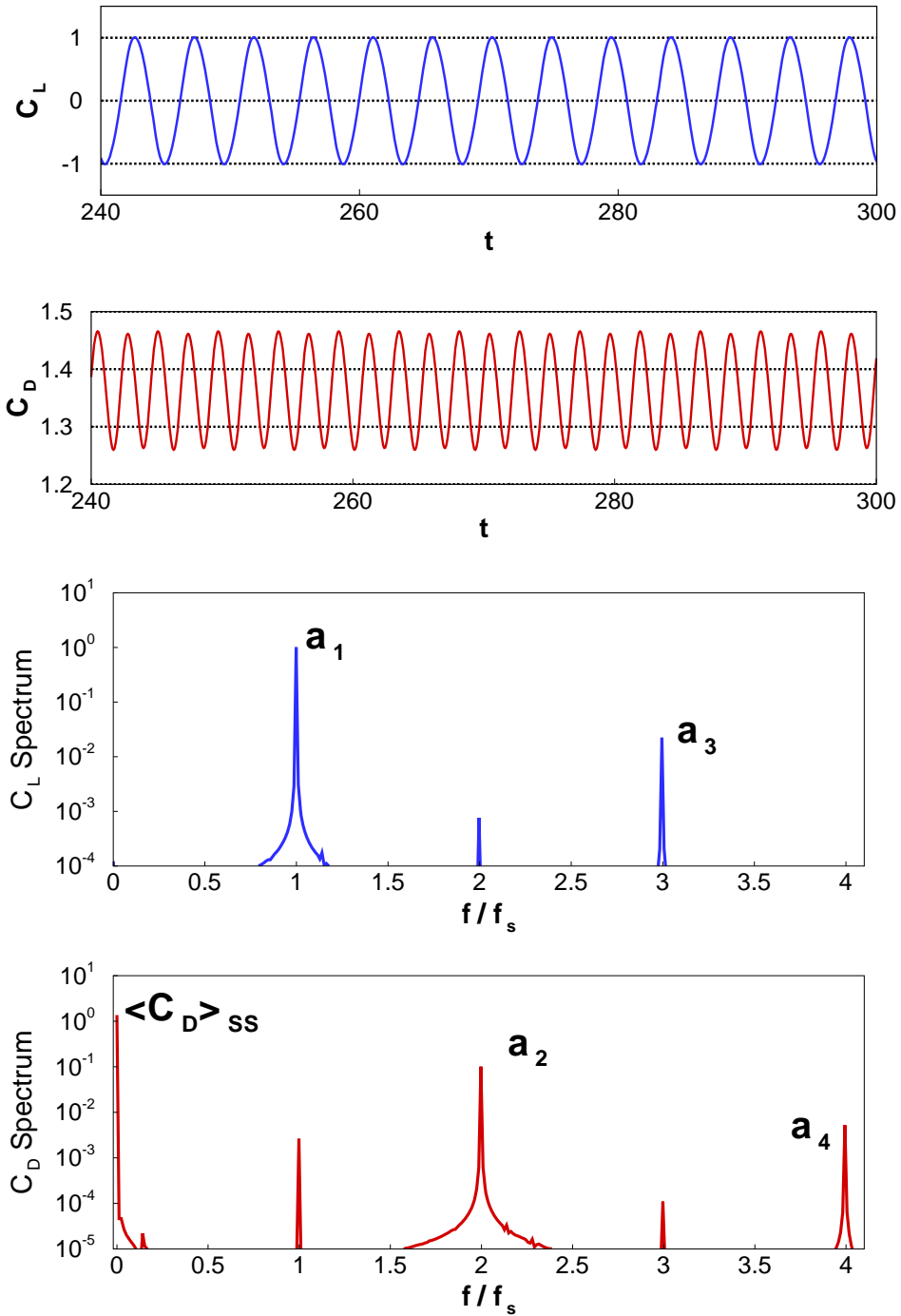


Figure 3.1: Time histories and corresponding power spectra of the lift and drag coefficients obtained from the CFD simulation at $Re = 500$.

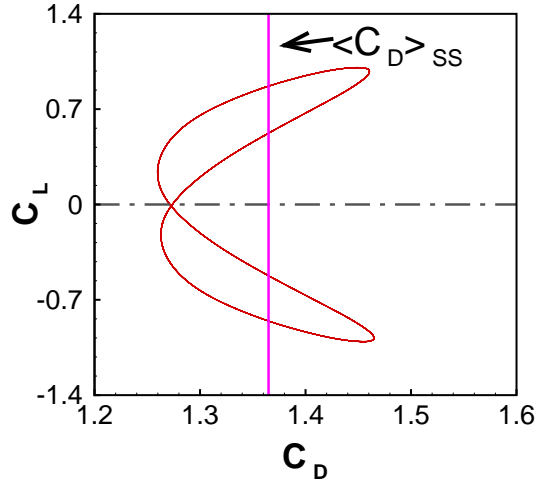


Figure 3.2: Projection of the phase portrait onto the $C_D - C_L$ plane at $Re = 500$.

C_D on a fixed cylinder at $Re = 500$. The lift power spectrum shows a large peak with amplitude a_1 at the natural vortex-shedding frequency f_s and a smaller peak a_3 at the its third harmonic $3f_s$. The corresponding time history shows the lift coefficient fluctuating periodically about the origin. Therefore, one infers that the lift coefficient oscillates at the shedding frequency and that its behavior is influenced by cubic, and, to lower extent, higher-order odd nonlinearities.

By contrast, the drag power spectrum shows a large peak a_2 at twice the shedding frequency ($2f_s$) and a smaller peak a_4 at the even harmonic $4f_s$. The corresponding time history shows the drag fluctuating periodically about a non-zero mean that reaches a constant value at steady state. This implies that the drag coefficient consists of a slowly varying mean term and a fluctuating term. The fluctuating term mainly varies quadratically with the lift coefficient, as the influence of the higher order even nonlinearities is quite small. The corresponding drag-polar plot in Figure 3.2 clearly illustrates this quadratic coupling between the drag and lift coefficients.

3.3 Modeling Background - Lift

Nayfeh et al. (2003) investigated two wake-oscillator models of the lift, namely, the van der Pol and Rayleigh oscillators. Using higher order spectral moments analysis, they found that for, a few cases, the phase angle ϕ_{13} between the lift components at f_s and $3f_s$ is around 90° . Consequently, they concluded that the van der Pol oscillator

$$\ddot{C}_L + \omega^2 C_L = \mu \dot{C}_L - \alpha C_L^2 \dot{C}_L \quad (3.1)$$

is the more suitable choice as an efficient and simple model for the steady-state lift coefficient. The angular frequency ω in equation (7) is related (but not equal) to the angular shedding frequency $\omega_s = 2\pi f_s$ and the parameters μ and α represent the linear and nonlinear damping coefficients, respectively. The values of μ and α are taken positive, so that the linear damping is destabilizing while the nonlinear damping is stabilizing. As a consequence, small disturbances grow and large ones decay, both eventually approaching a stable limit cycle. The values of the parameters in Equation (3.1) depend on the Reynolds number and their values are estimated based on the steady-state CFD lift data.

Using the method of multiple scales (Nayfeh, 1973, 1981) and assuming that the oscillator is weakly damped (i.e., $\mu = O(\epsilon)$ and $\alpha = O(\epsilon)$ where $\epsilon \ll 1$ is a small bookkeeping parameter), we obtained the following second-order approximate solution:

$$\begin{aligned} C_L(t) &= a(t) \sqrt{1 + \frac{1}{16\omega^2} \left[\mu - \frac{1}{4} \alpha a(t)^2 \right]^2} \sin[\omega t + \theta(t) + \eta(t)] \\ &\quad - \frac{\alpha}{32\omega} a(t)^3 \sin[3\omega t + 3\theta(t)] + \dots \\ &\equiv a_1(t) \sin[\omega t + \theta(t) + \eta(t)] - a_3(t) \sin[3\omega t + 3\theta(t)] + \dots \end{aligned} \quad (3.2)$$

where $\eta(t) = \tan^{-1} \left[\frac{16\omega}{\alpha a(t)^2 - 4\mu} \right]$ and the amplitude $a(t)$ and phase $\theta(t)$ are governed by

the modulation equations

$$\dot{a} = \frac{1}{8}(4\mu a - \alpha a^3) \quad (3.3)$$

$$\dot{\theta} = -\frac{1}{8\omega} \left(\mu^2 - \frac{3}{2}\alpha\mu a^2 + \frac{11}{32}\alpha^2 a^4 \right) \quad (3.4)$$

Setting $\dot{a} = 0$ in Equation (3.3), we obtain the steady-state values of a from the solution of $a(4\mu - \alpha a^2) = 0$. There are two possibilities: the trivial solution $a = 0$ and the nontrivial solution $a = 2\sqrt{\mu/\alpha}$. For the nontrivial solution, it follows from Equation (3.2) that

$$a_1 = 2\sqrt{\frac{\mu}{\alpha}} \quad \text{and} \quad a_3 = \frac{\mu}{4\omega} \sqrt{\frac{\mu}{\alpha}} \quad (3.5)$$

Moreover, we find that the angle $\eta = \frac{1}{2}\pi$ and, from Equation (3.4), we obtain the corresponding expression for $\dot{\theta} = -\mu^2/16$. Consequently, the angular shedding frequency is given by

$$\omega_s = \omega + \dot{\theta} = \omega - \frac{\mu^2}{16\omega} \quad (3.6)$$

Equation (3.6) shows that the angular frequency ω of the van der Pol oscillator is not exactly equal to the angular shedding frequency ω_s , as one would predict from a first-order expansion (Nayfeh et al., 2003). Hence, an improved second-order approximate expression for the steady-state lift coefficient becomes

$$C_L(t) \approx a_1 \cos(\omega_s t) + a_3 \cos(3\omega_s t + \frac{1}{2}\pi) \quad (3.7)$$

The methodology used to identify the system parameters for a given Reynolds number is as follows:

1. The CFD solver is used to calculate the time history of the lift coefficient.
2. Spectral analysis is performed on the steady-state part of the CFD data to extract the values of a_1 , a_3 , and f_s (or ω_s).

3. Equations (3.5) and (3.6) are then solved for the nonlinear and linear damping coefficients α and μ and the angular frequency ω .
4. With all of the parameters identified, Equation (3.1) is numerically integrated using a Runge-Kutta routine and the results are compared with the CFD results.

3.4 Modeling Background - Drag

Referring to Figure 3.1, we note that the drag consists of two major components. The first is a mean component that monotonically approaches a constant value in the steady state; this component is assumed to be independent of the lift. The second is an oscillatory component related to the lift and has a frequency equal to twice the lift frequency of oscillation.

Since the lift and drag have a common source, the pressure distribution on the cylinder surface, and in view of this two-to-one frequency relationship, Nayfeh et al. (2003) reasoned that the drag is quadratically related to the lift in some fashion. They examined the phase relation between the periodic components of the drag and lift and found that it is near 270° . Hence, they inferred that the periodic component of the drag must be proportional to $-C_L \dot{C}_L$ and proposed the drag model

$$C_D(t) = \langle C_D \rangle - 2 \frac{a_2}{\omega_s a_1^2} C_L(t) \dot{C}_L(t) \quad (3.8)$$

where a_2 is the amplitude of the drag component at $2 f_s$ and $\langle \ \rangle$ denotes the mean value. For steady-state behavior, the mean component of the drag $\langle C_D \rangle = \langle C_D \rangle_{ss}$ is constant. The constant value $\langle C_D \rangle_{ss}$ is determined from the CFD steady-state time history of the drag and the value of a_2 is determined from its spectral analysis.

3.5 Motivation for Improved Lift and Drag Models

The results presented in the previous section are solely based on matching the amplitudes and frequencies of the CFD and model results. Even though the agreement was generally acceptable, phase errors exist, especially in the drag, and we believe that the models need to be improved. Although the use of higher order spectral analysis of the CFD results showed that the phase ϕ_{13} between the lift components at f_s and $3f_s$ is nearly 90° , it actually differs from one case of Reynolds number to another. In fact, in some of our calculations, we found up to $\pm 25^\circ$ deviation from 90° . Obviously, this wide variation in the phase is not fully accounted for in the van der Pol model in Equation (3.1). This fact does not produce a real problem as long as one is concerned with the time histories because a_3 is usually two orders of magnitude smaller than a_1 . However, we would like to have the model very accurate in both of the time and spectral domains as we believe this excellent matching is important in case of extending the model to the moving-cylinder case.

Similarly, for the drag CFD calculations, we found that the phase ϕ_{12} between the lift component at f_s and the drag component at $2f_s$ deviates from 270° by as much as 85° . Qin (2004) proposed that the quadratic term in the drag model should be of the form C_L^2 instead of $-C_L\dot{C}_L$. He also found suggested a linear lift term in the drag model to account for linear coherence at f_s and $3f_s$. Thus, the model contained only a single linear term and a single quadratic term. Because we found that the drag components at f_s and $3f_s$ are negligible with respect to the fundamental one, we do not have linear terms in our drag model.

3.6 Improved Lift Model

Here, we modify the van der Pol oscillator by adding a Duffing-type nonlinearity to Equation (3.1), resulting in the new lift model

$$\ddot{C}_L + \omega^2 C_L = \mu \dot{C}_L - \alpha C_L^2 \dot{C}_L - \gamma C_L^3 \quad (3.9)$$

The coefficient γ is determined based on matching the phase ϕ_{13} obtained from the CFD data to the phase obtained from solving Equation (3.9). In this process, we use the method of harmonic balance to determine approximate solutions of the model. These solutions along with spectral analysis of the CFD data are used to identify all of the parameters in Equation (3.9).

Table 3.1: Lift parameters at different Reynolds numbers.

	Re = 300	Re = 500	Re = 1,000
f_s	0.211	0.217	0.229
a_1	0.914	1.009	1.229
a_3	0.012	0.022	0.042
ϕ_{13}	94°	95°	108°
ω_s	1.324	1.364	1.441
ω	1.324	1.375	1.568
μ	0.141	0.242	0.383
α	0.677	0.956	1.044
γ	-0.025	-0.031	-0.322

We seek a solution for the lift coefficient of the form

$$C_L(t) = c_1 \cos(\omega_s t) + c_2 \sin(\omega_s t) + c_3 \cos(3\omega_s t) + c_4 \sin(3\omega_s t) \quad (3.10)$$

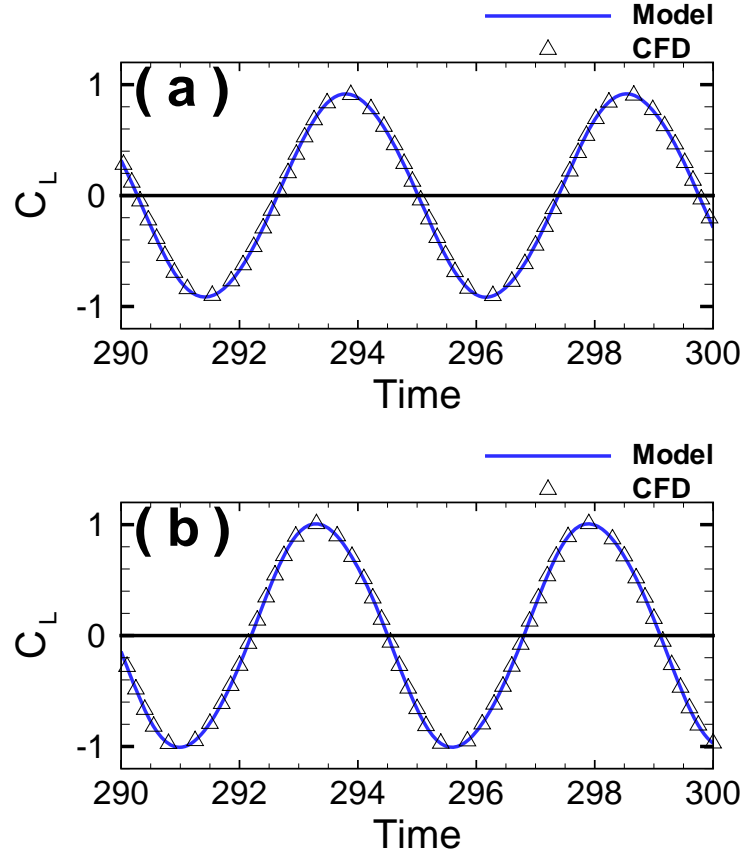


Figure 3.3: Comparisons of the steady-state time histories of the lift coefficients obtained with the CFD simulation and the improved model: (a) $Re = 300$ and (b) $Re = 500$.

Then, upon substituting Equation (3.10) into Equation (3.9) and separating the terms multiplying the different sine and cosine functions, we obtain the linear system

$$A\mathbf{y} = \mathbf{b} \quad (3.11)$$

where $\mathbf{y}^T = \{\omega^2, \mu, \alpha, \gamma\}$, $\mathbf{b}^T = \{c_1, c_2, 9c_3, 9c_4\}\omega_s^2$, and the A_{ij} entries of the matrix

A are

$$\begin{aligned}
A_{11} &= c_1, & A_{21} &= c_2, & A_{31} &= c_3, & A_{41} &= c_4, \\
A_{12} &= -c_2\omega_s, & A_{22} &= c_1\omega_s, & A_{32} &= -3c_4\omega_s, & A_{42} &= 3c_3\omega_s, \\
A_{13} &= \frac{1}{4} (c_2^3 - c_4c_2^2 + c_1^2c_2 + 2c_3^2c_2 + 2c_4^2c_2 - 2c_1c_3c_2 + c_1^2c_4) \omega_s, \\
A_{23} &= \frac{1}{4} (-c_1^3 - c_3c_1^2 - c_2^2c_1 - 2c_3^2c_1 - 2c_4^2c_1 - 2c_2c_4c_1 + c_2^2c_3) \omega_s, \\
A_{33} &= \frac{1}{4} (-c_2^3 + 6c_4c_2^2 + 3c_1^2c_2 + 3c_4^3 + 6c_1^2c_4 + 3c_3^2c_4) \omega_s, \\
A_{43} &= \frac{1}{4} (-c_1^3 - 6c_3c_1^2 + 3c_2^2c_1 - 3c_3^3 - 3c_3c_4^2 - 6c_2^2c_3) \omega_s, \\
A_{14} &= \frac{1}{4} (3c_1^3 + 3c_3c_1^2 + 3c_2^2c_1 + 6c_3^2c_1 + 6c_4^2c_1 + 6c_2c_4c_1 - 3c_2^2c_3), \\
A_{24} &= \frac{1}{4} (3c_2^3 - 3c_4c_2^2 + 3c_1^2c_2 + 6c_3^2c_2 + 6c_4^2c_2 - 6c_1c_3c_2 + 3c_1^2c_4), \\
A_{34} &= \frac{1}{4} (c_1^3 + 6c_3c_1^2 - 3c_2^2c_1 + 3c_3^3 + 3c_3c_4^2 + 6c_2^2c_3), \\
A_{44} &= \frac{1}{4} (-c_2^3 + 6c_4c_2^2 + 3c_1^2c_2 + 3c_4^3 + 6c_1^2c_4 + 3c_3^2c_4)
\end{aligned}$$

The c_j are determined by matching the solution in Equation (3.10) with the steady-state CFD simulation, which is expressed as

$$C_L(t) = a_1 \cos(\omega_s t) + a_3 \cos(3\omega_s t + \phi_{13}) \quad (3.12)$$

This yields the coefficients $c_1 = a_1$, $c_2 = 0$, $c_3 = a_3 \cos \phi_{13}$, and $c_4 = -a_3 \sin \phi_{13}$.

Listed in Table 3.1 are the results for the cases $\text{Re} = 300$ and 500 . From the values of α and γ , the Duffing cubic term is small, but should not be neglected in the modeling. In Figure 3.3, we plot the steady-state time histories of the lift coefficient obtained from the improved model and the CFD simulations. For both cases, there is excellent agreement between the two results.

3.7 Improved Drag Model

In the simulations we have conducted thus far, we found that the phase ϕ_{12} is not around 270° ; the actual value of the phase may vary from one case of Reynolds number to another by up to 85° , which is quite significant. Therefore, we propose a new model in which the drag is proportional to both $C_L \dot{C}_L$ and C_L^2 in the following manner:

$$C_D(t) = \langle C_D \rangle + 2k_1 \frac{a_2}{a_1^2} (C_L^2 - \langle C_L^2 \rangle) + 2k_2 \frac{a_2}{\omega_s a_1^2} C_L \dot{C}_L \quad (3.13)$$

The first expression in Equation (3.13) represents the mean component of the drag, which reaches a constant value $\langle C_D \rangle_{ss}$ in the steady state. The term $-\langle C_L^2 \rangle$ in the second expression in Equation (3.13) negates the DC component introduced by C_L^2 . The contributions of both quadratic expressions to the overall behavior of the drag are determined by matching the amplitude a_2 and phase ϕ_{12} obtained from the model with the CFD results at steady state.

To this end, we substitute Equation (3.12) into Equation (3.13), expand the result, and obtain

$$C_D(t) = \langle C_D \rangle_{ss} + a_2 [k_1 \cos(2\omega_s t) - k_2 \sin(2\omega_s t)] + \dots \quad (3.14)$$

Then, by comparing Equation (3.14) with the CFD result

$$C_D(t) = \langle C_D \rangle + a_2 \cos(2\omega_s t + \phi_{12}) + \dots \quad (3.15)$$

we obtain $k_1 = \cos \phi_{12}$ and $k_2 = \sin \phi_{12}$. In Table 3.2, we present the drag model parameters for $\text{Re} = 300$ and 500 . It is clear from the values of k_1 and k_2 that the term C_L^2 can play a role nearly as influential as the term $C_L \dot{C}_L$ on the behavior of the drag coefficient.

Table 3.2: Drag parameters at different Reynolds numbers.

	Re = 300	Re = 500	Re = 1,000
$\langle C_D \rangle_{ss}$	1.38	1.37	1.41
a_2	0.080	0.065	0.152
ϕ_{12}	335.1°	334.9°	331°
k_1	0.907	0.906	0.875
k_2	-0.421	-0.424	-0.485

In Figure 3.4, we plot the steady-state time histories of the drag coefficient for $Re = 300$ and 500 . Results obtained from the improved drag model are compared with the CFD simulation results and excellent agreement is demonstrated for all of the cases presented.

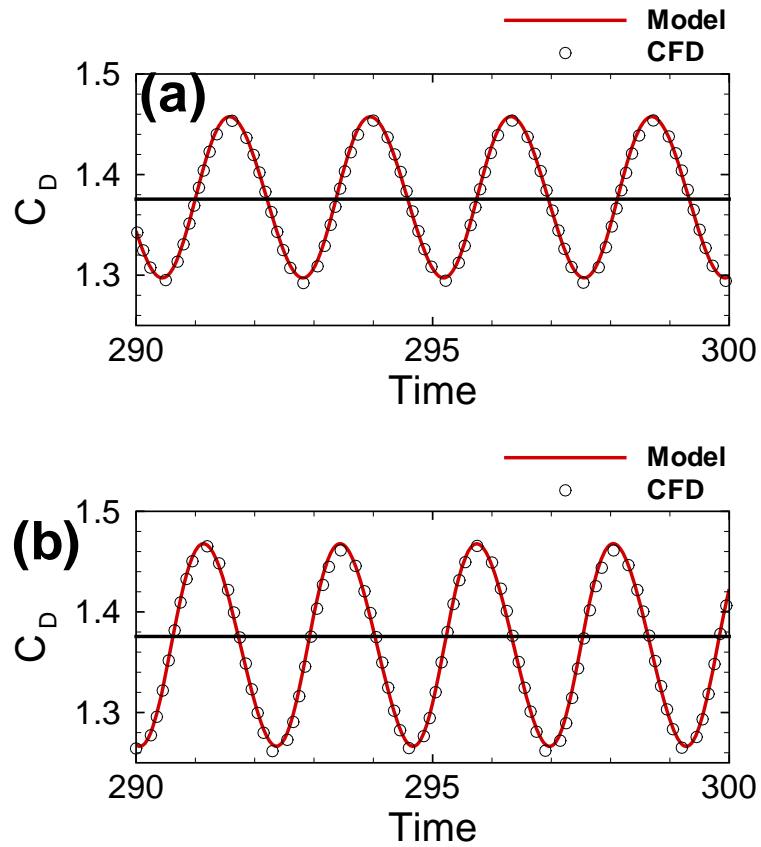


Figure 3.4: Comparisons of the steady-state time histories of the drag coefficient obtained from the CFD simulation and the improved model: (a) $Re = 300$ and (b) $Re = 500$.

Chapter 4

Improved Wake Oscillator for a Cylinder with Cross-Flow Motion

4.1 Synopsis

In this chapter, we extend the free-wake oscillator presented in the previous chapter to an oscillator for the wake of a cylinder moving in the cross-flow direction. We consider several forced oscillators that employ common forcing terms as well as introduce oscillators with new forcing types. Each model corresponds to a different structural coupling (or forcing) term, which can be external (additive), or parametric (multiplicative), or a combination of both. We evaluate the performances and stability limits of these oscillators and their ability to model the wake of a moving cylinder using analytical techniques. We investigate the impact of the model parameters on their prediction for different excitation frequencies. These parameters give a great deal of flexibility to the proposed oscillators, enabling their tuning for a wide range of problems. The new oscillators have dual forcing types (external and parametric), with either velocity-based or acceleration-based forcing. They can capture the

multi-valuedness and jumps in the frequency-response curves, in contrast to existing models that either capture one branch of the frequency-response curve (low amplitude or large amplitude) or replace the jump by a steep variation.

4.2 Analysis

We start with the forced version of the improved free-wake oscillator developed by Marzouk et al. (2007) for the lift coefficient on a fixed cylinder. This model with a generic forcing term is

$$\ddot{C}_L + \omega^2 C_L - \mu \dot{C}_L + \alpha C_L^2 \dot{C}_L + \gamma C_L^3 = \text{Forcing} \quad (4.1)$$

For the free-wake case (i.e., fixed cylinder), there is no forcing term and the right-hand side of Equation (4.1) is zero. We pick a typical case of a low Reynolds number where two-dimensionality can be reasonably assumed. Our aim is to choose the forcing term on the right-hand side of Equation (4.1) to predict the lift on a cylinder undergoing forced oscillations. We do not try to fit a certain set of experimental or numerical data. Rather, we search for the proper forcing terms that enable the model to capture the multi-valuedness of the response (and hence the hysteretic phenomenon). Therefore, we do not compare $C_L(t)$ in the subsequent sections with a particular set of data. Any stable point on the frequency-response curves to be presented later corresponds to a version of Equation (4.1) with a unique right-hand side. This version of the equation can be integrated numerically and the resulting $C_L(t)$ is periodic, like the one shown in Figure 3.3 but with different frequency and amplitude.

The numerical and experimental studies (e.g., Parkinson et al., 1968; Korpus et al., 2000; Carberry et al., 2001 and 2002; Marzouk and Nayfeh, 2007 and 2008a) show that the frequency-response curve of the lift exhibits a softening-type nonlinearity. The

amplitude of the synchronized lift is small at low frequencies and suddenly increases to high values as a critical frequency is exceeded. We tried several forcing terms in Equation (4.1) and examined the synchronized response for each case. A good candidate for the synchronized wake oscillator should be able to capture the observed jump in the response and its softening behavior. We used the method of harmonic balance to compute periodic solutions and verified the results using a fourth-order Runge-Kutta scheme.

We express the synchronized lift coefficient (C_L) as

$$C_L(t) = \sum_{i, \text{ odd}} a_i \cos(i \Omega t) + b_i \sin(i \Omega t) \quad (4.2)$$

It is reasonable to keep the first and third harmonics only because higher harmonics have relatively negligible amplitudes. We note that the lift spectrum consists of a main peak (at the forcing frequency Ω) and its odd harmonics only. This holds for free wakes also, but the main lift component is at the natural vortex-shedding frequency, ω_s , which is the angular natural vortex-shedding frequency.

It is better to use relative quantities when showing the results rather than the absolute ones. The results are presented in terms of the lift amplitude C_L of the forced wake relative to the free wake value C_{L_o} and the angular forcing frequency Ω relative to the angular natural vortex-shedding frequency ω_s of the free wake.

4.3 Oscillators with External Forcing

We start with external forcing terms and consider three cases where the forcing is harmonic and related to either the displacement, velocity, or acceleration; that is,

$$\text{Forcing} = K \cos(\Omega t) \quad (4.3)$$

$$\text{Forcing} = -K \Omega \sin(\Omega t) \quad (4.4)$$

$$\text{Forcing} = -K \Omega^2 \cos(\Omega t) \quad (4.5)$$

The responses of the wake oscillator with different forcing amplitudes K are shown in Figure 4.1.

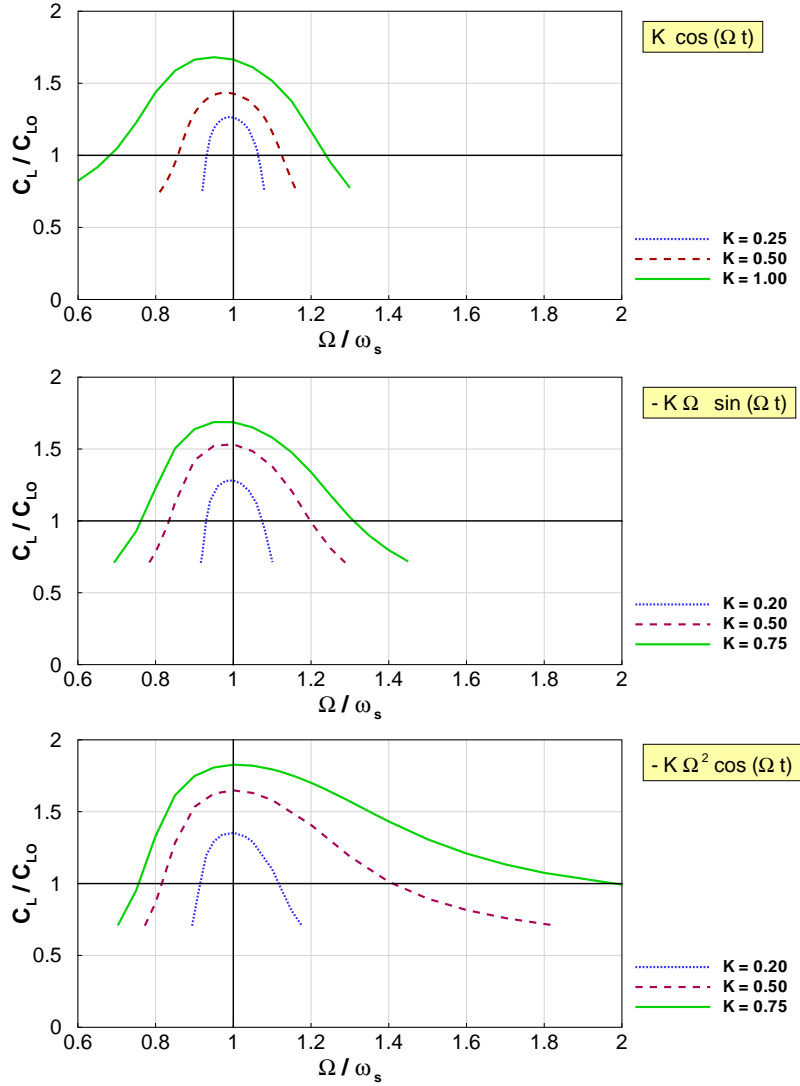


Figure 4.1: Prediction of the wake oscillator with external forcing having different amplitudes.

Whereas the three forcing types result in quite similar response profiles, the acceleration-type forcing causes the frequency-response curve to be biased to the high-frequency side. Using a displacement-type forcing results in an opposite effect. Because all of the responses are continuous and single-valued, these forcing types do not reproduce all of the features of the wake. This is a very important finding and explains why the models proposed in the literature do not capture the discontinuity in the response because they typically have an external velocity-type forcing term, as in Equation (4.4). We should add here that this velocity-type forcing was merely an arbitrary choice by Hartlen and Currie (1970) and was not based on any, even simplified, analysis.

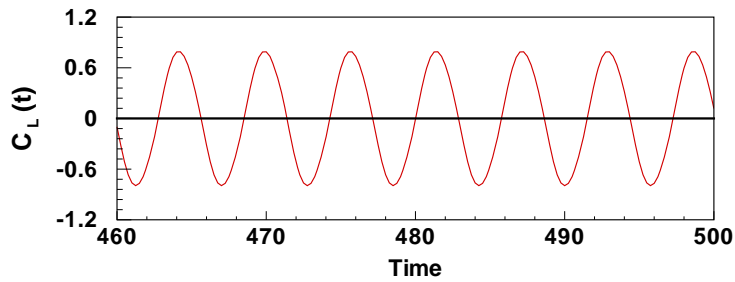


Figure 4.2: Stable solution of the forced oscillator.

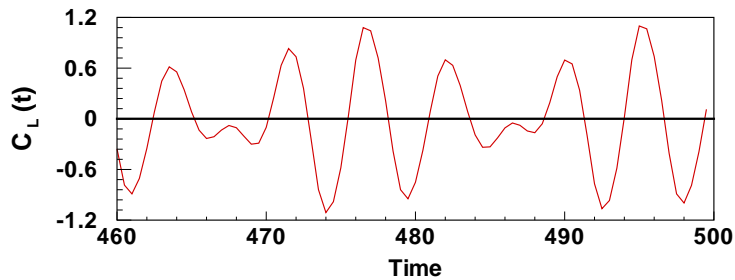


Figure 4.3: Unstable solution of the forced oscillator.

A horizontal line in each plot in Figure 4.1 at a value ≈ 0.707 represents the stability limit. The lift is periodic and synchronized at the forcing frequency above these lines,

whereas it is either periodic with a large period or aperiodic and nonsynchronized below them. We are not interested in these unstable solutions and thus do not show them in Figure 4.1 and the subsequent figures. At these stability limits, instability occurs, resulting in the periodic solution losing stability. An example of a stable periodic $C_L(t)$ is given in Figure 4.2, and an example of an unstable solution is given in Figure 4.3. These examples correspond to the points $\Omega/\omega_s=0.8$ and 0.75 in the middle plot of Figure 4.1, with the forcing amplitude $K=0.5$.

Before proceeding to other forcing types, we verified that two odd-harmonic terms produce accurate results. Adding even harmonics to Equation (4.2) has no effect because their amplitudes turn out to be zeros. Also, adding a fifth-harmonic term has almost no effect on the wake response, as shown in Figure 4.4.

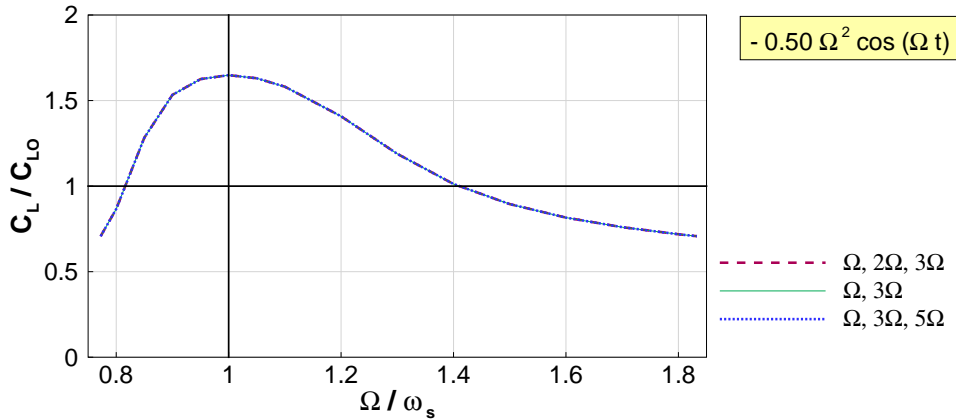


Figure 4.4: Responses predicted with external acceleration-based forcing for different numbers of harmonic terms in the method of harmonic balance.

4.4 Oscillators with Parametric Forcing

We next study parametric (or multiplicative) forcing terms of the following types:

$$\text{Forcing} = K \cos(\Omega t) C_L^2 \quad (4.6)$$

$$\text{Forcing} = -K \Omega \sin(\Omega t) C_L^2 \quad (4.7)$$

$$\text{Forcing} = -K \Omega^2 \cos(\Omega t) C_L^2 \quad (4.8)$$

The responses of the oscillators for the same forcing amplitude of $K = 1.2$ are given

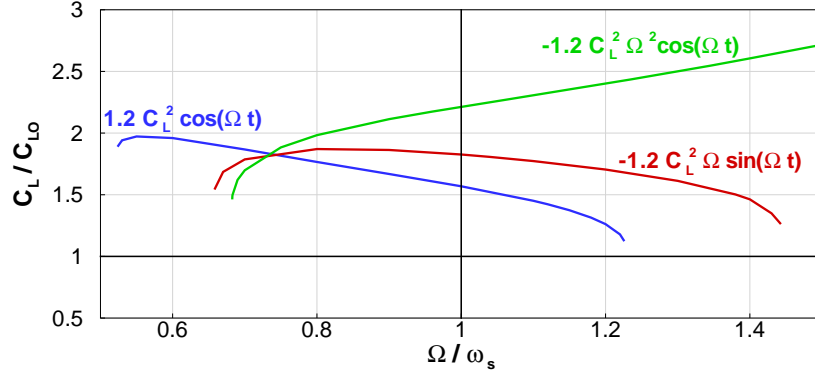


Figure 4.5: Frequency-response curves of wake oscillators with parametric forcing.

in Figure 4.5. This forcing amplitude was selected so that the response range matches the high-amplitude lift obtained for this forced wake problem in some numerical and experimental studies. Also, the choice of C_L^2 rather than C_L was necessary to avoid a DC component and even harmonics in the response. To illustrate this, we show in Figure 4.6 a case for the following parametric forcing:

$$\text{Forcing} = K \cos(\Omega t) C_L \quad (4.9)$$

There exists only one stable period solution at a certain frequency, indicating the synchronized C_L is single-valued and not multi-valued. Also, there are no stable

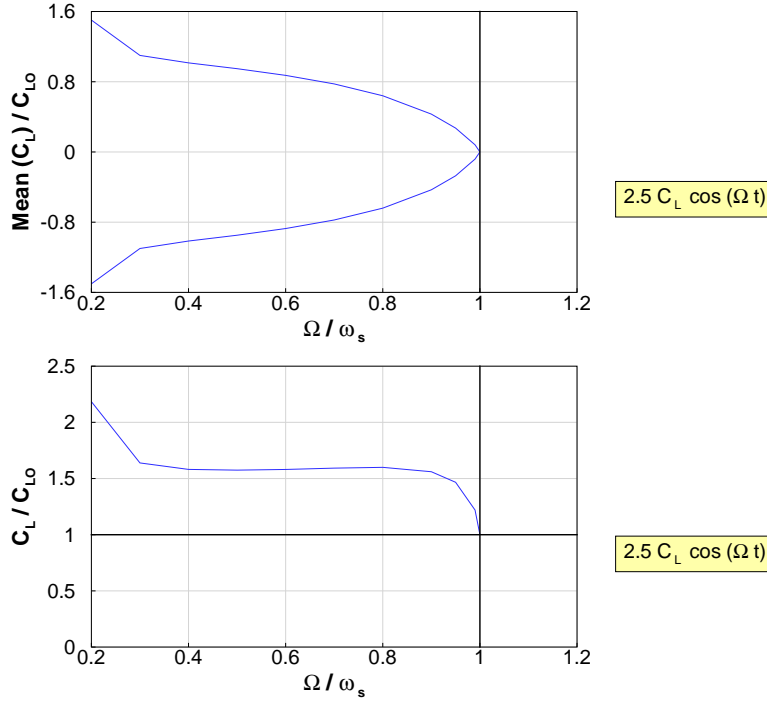


Figure 4.6: The mean (top) and amplitude (bottom) of the lift of a wake oscillator with linear parametric forcing.

periodic solutions for $\Omega > \omega_s$. Moreover, there is a significant mean component in the response. Because all of these characteristics are at variance with numerical and experimental results, this forcing type is ruled out.

4.5 Oscillators with Mixed Forcing

Because neither the external forcing by itself nor the parametric forcing by itself could capture the desired multi-valued responses, the question arises whether a combination of them could capture the dynamics. To answer this question, we consider the following forcing terms:

$$\text{Forcing} = -K_1 \Omega \sin(\Omega t) - K_2 \Omega^2 \sin(\Omega t + \beta) C_L^2 \quad (4.10)$$

$$\text{Forcing} = -K_1 \Omega^2 \cos(\Omega t) - K_2 \Omega^2 \cos(\Omega t + \beta) C_L^2 \quad (4.11)$$

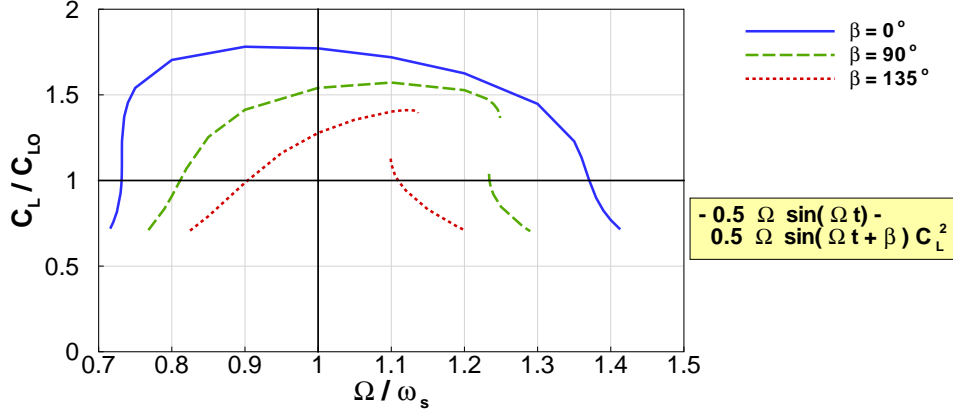


Figure 4.7: Frequency-response curves of wake oscillators with mixed external-and-parametric velocity-based forcing (zero and positive phase β).

The forcings in Equations (4.10) and (4.11) involve a phase angle β between the parametric and external parts. We found that this phase is very important and has a key role in tuning the response. A positive phase yields a hardening-type nonlinear response, whereas a negative phase yields a softening-type nonlinear response. Thus, we need to choose negative values for β . This effect of β and sample response curves generated using the velocity-based forcing of Equation (4.10) are given in Figure 4.7 for zero and positive phase values and in Figure 4.8 for zero and negative phase values. Similar results for the acceleration-based forcing of Equation (4.11) are given in Figure 4.9.

These figures provide the answer to the raised question, which is yes. Multi-valuedness is achieved when a combination of external and parametric forcing is used. To illustrate this, one can look, for example, at the curve corresponding to $\beta = 135^\circ$ in Figure 4.7. There are two detached branches: one in the range $1.099 \geq \Omega / \omega_s \geq 1.200$

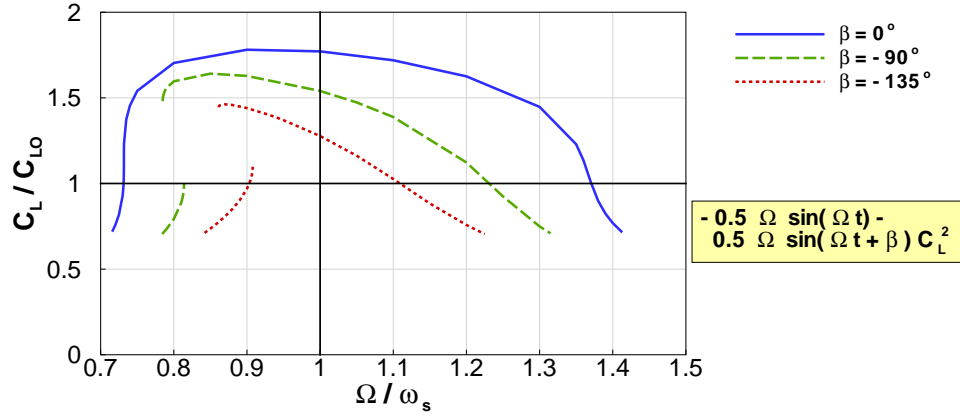


Figure 4.8: Frequency-response curves of wake oscillators with mixed external-and-parametric velocity-based forcing (zero and negative phase β).

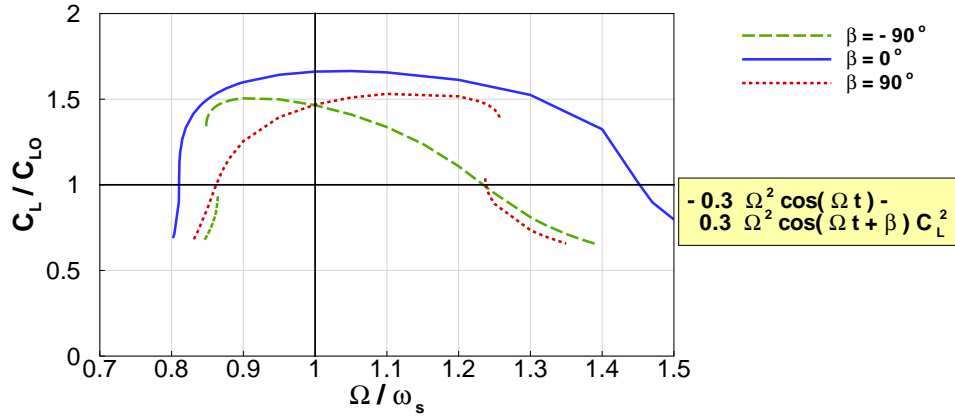


Figure 4.9: Frequency-response curves of wake oscillators with mixed external-and-parametric acceleration-based forcing (zero, positive, and negative phase β).

and the other in the range $0.825 \geq \Omega/\omega_s \geq 1.137$. Consequently, there is a narrow range of overlap ($1.099 \geq \Omega/\omega_s \geq 1.137$), where two possible solutions coexist: one corresponds to a high-amplitude periodic C_L with $C_L/C_{L0} \approx 1.4$ and the other corresponds to a low-amplitude periodic C_L with $C_L/C_{L0} = 0.99-1.13$. The initial conditions will determine which of these solutions would be realized. In physical sit-

uations, a riser, an umbilical, a tower of an offshore wind turbine, or a cylinder-like structure subject to an oscillatory incoming stream (due to the existence of an upstream bluff structure that causes vortex shedding) or due to turbulence will initially experience the low-amplitude C_L solution if the ratio of the oscillation frequency to the Strouhal frequency lies within this overlap range. As this frequency ratio is decreased beyond the range of the low-amplitude branch, a sudden jump-up occurs from the low-amplitude branch to the large-amplitude one (at $\Omega/\omega_s=1.099$ in the current example). If this ratio is decreased further, C_L follows the large-amplitude branch. However, if this ratio is increased beyond the range of the large-amplitude branch (i.e., beyond $\Omega/\omega_s= 1.137$ in the current example), a jump-down occurs from the upper branch to the lower branch. Therefore, multi-valuedness results in a hysteresis. We emphasize that the change in the frequency ratio is not only dependent on the frequency of the oscillatory flow (or the oscillatory cylinder), but also on the Strouhal frequency of the non-oscillating stream (i.e., uniform) or non-oscillating cylinder (i.e., fixed). Thus, this frequency ratio depends also on the Reynolds number (or the velocity of the incoming stream, which can change in time).

There is no substantial difference between the response with the forcing in Equation (4.10) and with that in Equation (4.11). However, the physical meaning of each forcing type might result in favoring one over the other. The choice depends on whether the cylinder acceleration or velocity is the dominant in driving the wake.

We then examine the effect of the forcing amplitudes (K_1 and K_2). In Figure 4.10, we use the same value for both amplitudes and fix the phase β at -160° . Increasing K_1 and K_2 broadens the range of stable responses and increases their amplitude. In Figure 4.11, we consider the cases $K_1 = 2K_2$ and $K_1 = K_2/2$. For the first case (stronger external part of the forcing), multi-valuedness is lost, and the two branches

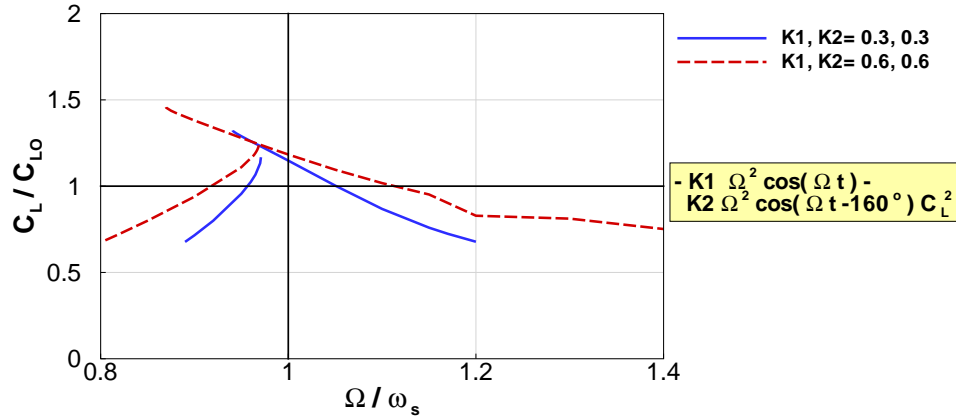


Figure 4.10: Frequency-response curves of wake oscillators with mixed external-and-parametric acceleration-based forcing when $\beta = -160^\circ$.

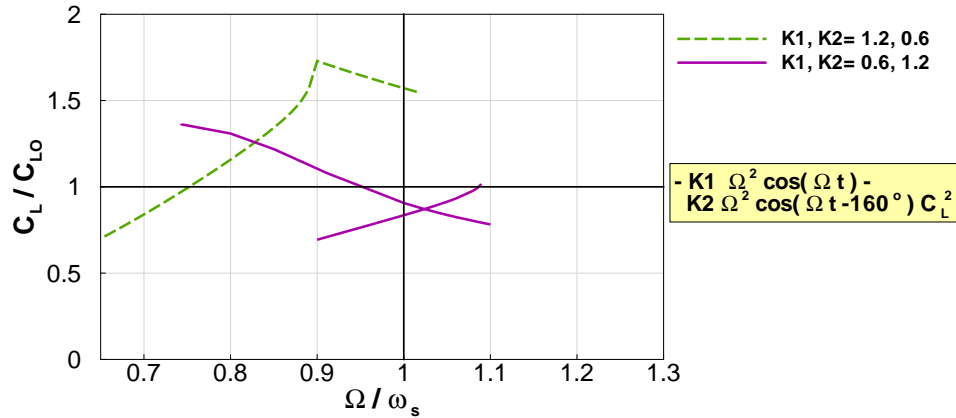


Figure 4.11: Frequency-response curves of wake oscillators with mixed external-and-parametric acceleration-based forcing when $\beta = -160^\circ$.

of the response curve merge together. Also, the stable response is shifted toward the low-frequency side and its amplitude is increased. Opposite effects result when the parametric part of the forcing overpowers the external one. The forcing parameters (β , K_1 , and K_2) can be chosen so that the oscillator accurately models the synchronized lift for arbitrary flow conditions.

Chapter 5

Characterization of the Modes in the Wake

5.1 Synopsis

In this chapter, we study the modes that can occur in the wake of a cylinder driven in the cross-flow direction within and outside the frequency band of synchronization. Within this band, shedding is locked onto the oscillation frequency and a period-1 response is obtained. However, complex modes take place outside the synchronization band and conventional analysis techniques (such as time histories or power spectra) might fail to characterize and distinguish some of these modes. We combine power spectra with phase portraits and Poincaré sections and show that the non-synchronized responses may be periodic with large period, quasiperiodic, or chaotic. Moreover, we show that the route to chaos is torus breakdown.

5.2 Analysis

We consider the flow over a rigid cylinder, which is forced to move harmonically in the cross-flow direction with a nondimensional amplitude A/D and frequency f_E (the subscript E stands for excitation). We use the lift coefficient to characterize the flow response to the applied cylinder motion. Depending on the amplitude and frequency of this motion, the nonlinearity of the flow may cause the shedding frequency and hence the frequency of the lift to be synchronized with the motion. This phenomenon is also referred to as fundamental synchronization. Consequently, the synchronized lift is periodic with a period equal to the period of the cylinder motion and we refer to this motion as period-one motion. We note that the lift on a fixed cylinder is also periodic, but the period is $T_s = 1/f_s$, in contrast to $T_E = 1/f_E$ in the synchronized case of a driven cylinder. The lift in this problem has been modeled by a forced single-degree-of-freedom nonlinear oscillator with cubic nonlinearity (e.g., Hartlen and Currie, 1970; Iwan and Blevins, 1974; Marzouk and Nayfeh, 2008b). As the frequency of excitation is decreased or increased outside the fundamental synchronization region, the synchronized response bifurcates and exhibits different behaviors, which are more complex than the period-one response (Bishop and Hassan, 1964; Williamson and Roshko, 1988; Korpus et al., 2000; Baek and Lee, 2001; Dong and Karniadakis, 2005; Zheng and Zhang, 2008). In this chapter, we use modern methods of nonlinear dynamics to characterize these complex responses (Nayfeh and Balachandran, 1995). These methods include power spectra, phase portraits, and Poincaré sections.

We simulated the flows over fixed and driven cylinders at $Re=500$. This choice of Re is a reasonable compromise between two factors. The first is to avoid the highly dissipative regime at lower Re , which can remarkably suppress or even eliminate the nonlinear phenomena in the flow (Blackburn and Henderson, 1996 and 1999).

Placzek et al. (2009), for example, did not obtain bistability in the wake because of the low Reynolds numbers they considered ($Re=100$). The second is to reduce three-dimensional effects, which become strong at higher Re . We should add that the motion increases the spanwise coherence and makes the flow field closer to two-dimensional (Blevins, 1990; Meneghini et al., 1997; Saltara et al., 1998; Blevins and Coughran, 2008). For the fixed-cylinder case, our calculated natural vortex-shedding frequency f_s , standard deviation of the lift coefficient, mean drag coefficient, and standard deviation of the drag coefficient are 0.217, 0.713, 1.36, and 0.072, respectively. These results are in agreement with different experimental and numerical studies, such as those of Roshko (1953) ($f_s=0.21$ from wind-tunnel experiments on a cylinder with a length-to-diameter ratio of 625), Wen et al. (2004) (mean $C_D=1.4$ from soap film experiments), and Norberg, (2003) (standard deviation of $C_L=0.67$ from 2D and 3D simulations).

The nondimensional cross-flow displacement $Y(t)$ is described by

$$Y(t) = \frac{A}{D} \sin(2\pi f_E t) \quad (5.1)$$

The motion starts from the beginning of the simulation and lasts long enough for the steady state to develop. We typically run the simulation for 1,000 nondimensional time units (about 215 times the natural shedding period), which provides sufficiently long intervals of lift and drag coefficients free of transient effects.

5.3 Magnification of the Lift and Drag

We set $A/D=0.25$ and vary $F_E \equiv f_E/f_s$ from 0.5 to 2.0. This amplitude choice is based on an earlier study (Marzouk and Nayfeh, 2007), where we found that this value is reasonably high enough for nonlinear effects to develop in the flow. We start

with a survey of the responses in the interval $2.0 \geq F_E \geq 0.5$ and plot measures of them in Figure 5.1. Within the synchronization region, the lift and drag are periodic with periods T_E and $2T_E$, respectively, and hence we could use their maxima as the measures. On the other hand, because the responses outside the synchronization region are modulated, we use magnification factors as the measures. The magnification factors are defined as the standard deviations scaled with respect to those of the fixed-cylinder case (0.713 for C_L and 0.072 for C_D). We note that there are two jumps in the curves at both ends of the synchronization region, where the synchronized responses lose stability. Another jump in the lift occurs within the synchronization region, which corresponds to an abrupt change in the wake, as observed in various experimental and numerical studies, such as the experiments of Williamson and Roshko (1988) at $100 \geq \text{Re} \geq 300$ and the simulations of Korpus et al. (2000) at $\text{Re}=3,800$. Next, we use different analysis tools to characterize the simulated results, starting with the periodic ones.

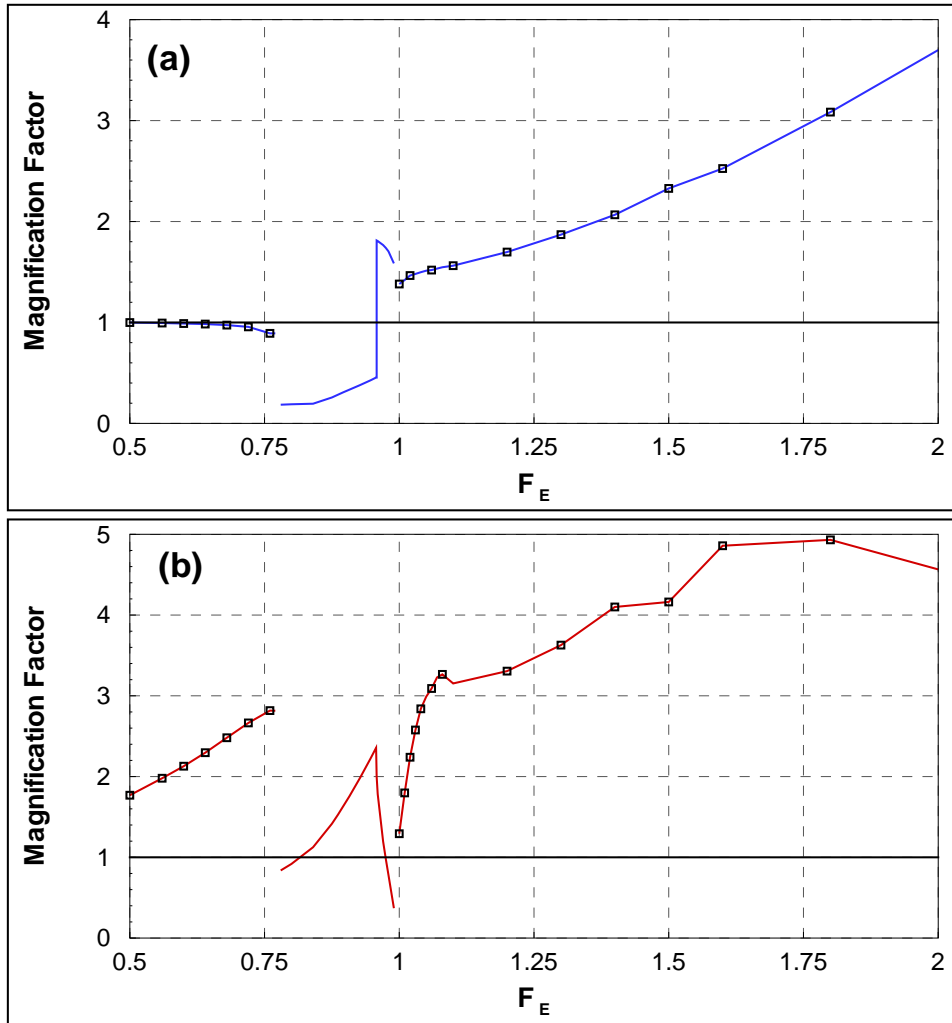


Figure 5.1: Magnification factors of C_L and C_D within (curve without markers) and outside (curve with markers) the synchronization region.

5.4 Longtime Histories

One might be able to use longtime histories of low-order periodic responses to characterize them. In Figure 5.2, we show the time series of C_L for three cases: period-1 (synchronized), period-2, and period-3 responses. The time series in Figure 5.2a is for a period-1 at $F_E=0.98$; it is a uniform trace and its envelope is flat. Moreover, it is nearly harmonic and has a dominant frequency, which, in this case, is the forcing frequency. In Figures 5.2b and 5.2c, we show the time series for $F_E = 1.8$ and $F_E = 1.4$, respectively. In Figure 5.2b, a complete cycle of C_L takes place over 5.11 time units, which is twice the period of the excitation ($T_E=2.555$ time units); therefore, it is a period-2 response. In Figure 5.2c, a complete cycle of C_L takes place over 9.86 time units, which is three times the period of the excitation ($T_E=3.29$ time units); therefore, it is a period-3 response. For these period- n responses, each C_L cycle has n different peaks. The C_D time series corresponding to the cases in Figure 5.2 are shown in Figure 5.3. For the synchronized case, C_D is near harmonic as is the case for C_L , but with frequency $2f_E$. For the period-2 and period-3 responses, the C_D time series are not as helpful as those of C_L in recognizing the type of the response because of the intensified modulation. We conclude that it is not easy to determine the period from a time series to the accuracy needed and hence ascertain the order of periodicity from the time series even for period-2 and period-3 responses. Next, we check whether the spectrum is a better tool for characterizing periodic responses.

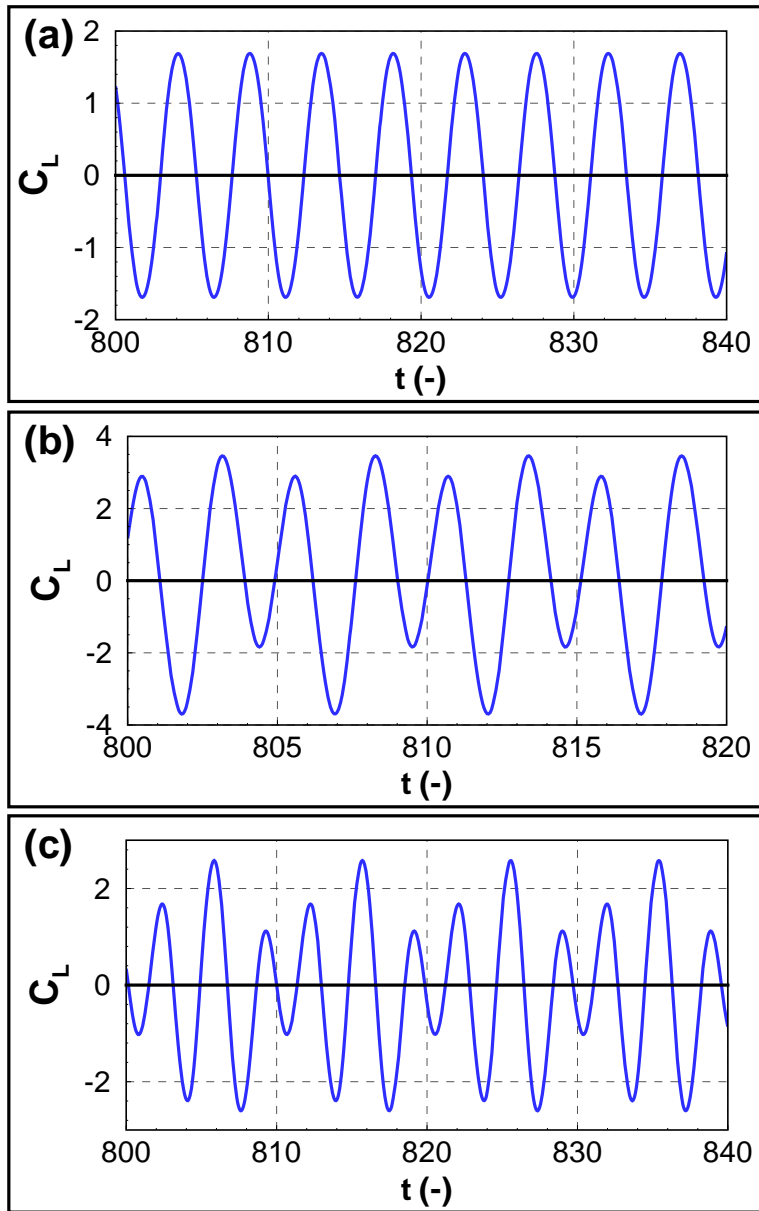


Figure 5.2: Longtime history of C_L : (a) period-1 response at $F_E = 0.98$, (b) period-2 response at $F_E = 1.80$, and (c) period-3 response at $F_E = 1.40$.

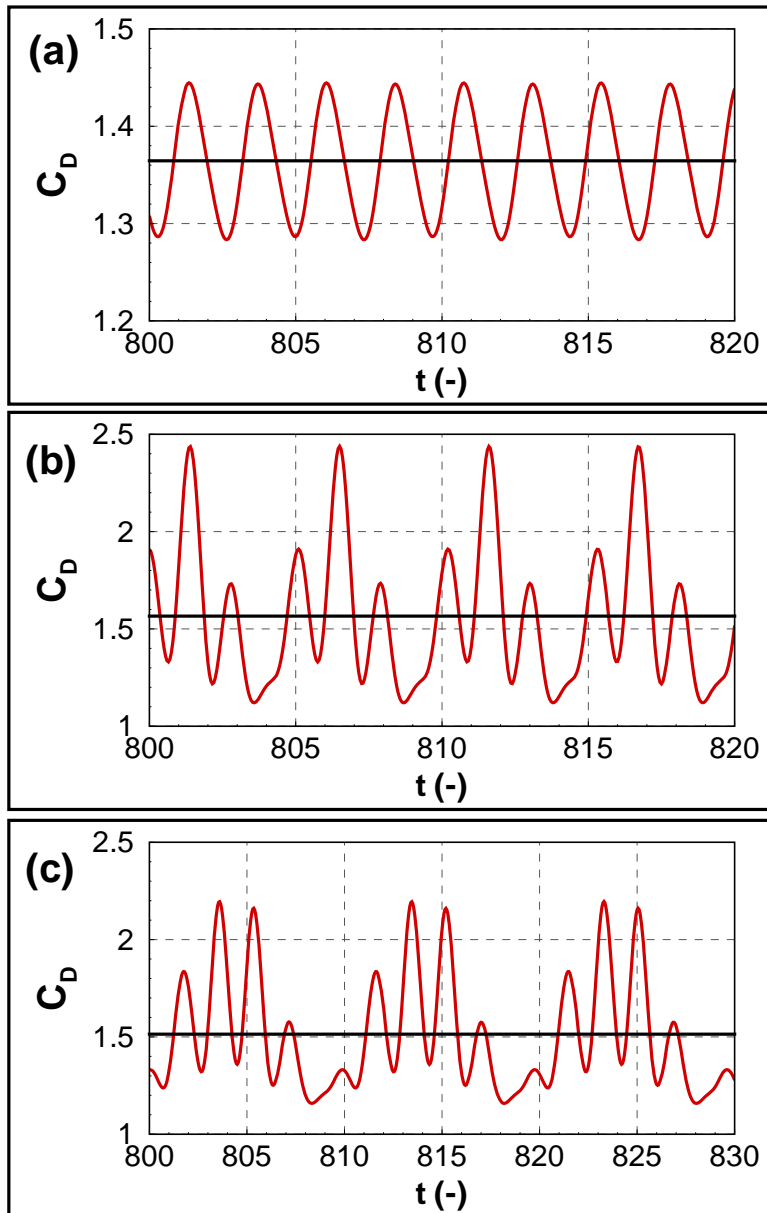


Figure 5.3: Longtime history of C_D : (a) period-1 response at $F_E = 0.98$, (b) period-2 response at $F_E = 1.80$, and (c) period-3 response at $F_E = 1.40$. The solid horizontal lines correspond to the mean values.

5.5 Power Spectra

In Figure 5.4, we show the power spectra of C_L for the time series in Figure 5.2. The spectrum of C_L in Figure 5.4a has a sharp spike at f_E and a two orders of magnitude smaller third superharmonic at $3f_E$. Hence, there is no ambiguity in concluding that its corresponding response is periodic with period $T_E = 1/f_E$, and hence it is a period-1 response. In addition to the strong spike at the excitation frequency f_E and its superharmonics mf_E , the spectrum in Figure 5.4b has spikes at $kf_E/2$, where k is an integer, indicating that the period of the response is $2/f_E$, which is double that of the excitation. Therefore, it is a period-2 response. Also, in addition to the strong spike at the excitation frequency f_E and its superharmonics mf_E , the spectrum in Figures 5.4c has spikes at $kf_E/3$, where k is an integer, indicating that the period of the response is $3/f_E$, which is three times that of the excitation. Therefore, it is a period-3 response. Similarly, the spectrum in Figure 5.5a has spikes at $kf_E/4$, where k is an integer, indicating that the period of the response is $4/f_E$. Therefore, it is a period-4 response. The spectrum in Figure 5.5b has spikes at the subharmonics $f_E/5$ and $3f_E/5$ and hence the corresponding response is period-5. The spectrum in Figure 5.5c has a number of spikes below f_E , which seem to be at $kf_E/9$ and hence its corresponding response might be a period-9. This is confirmed below using its one-sided Poincaré section. As the period of the response becomes longer and the number of spikes below f_E increases, as in the last case, determining with sufficient accuracy whether their corresponding frequencies are commensurate with f_E might not be feasible and hence such responses might be confused with quasiperiodic responses. For such responses, we use their one-sided Poincaré sections.

The spectra of the corresponding C_D of the period- n responses in Figure 5.4 are shown in Figure 5.6. In addition to the considerable DC component in the C_D spectra, they

differ from the C_L ones in that they have twice the number of dominant spikes. For example, the period-2 response has two C_L -spectrum spikes at f_E and $f_E/2$, whereas it has four C_D -spectrum spikes at $2f_E$, $3f_E/2$, f_E , and $f_E/2$.

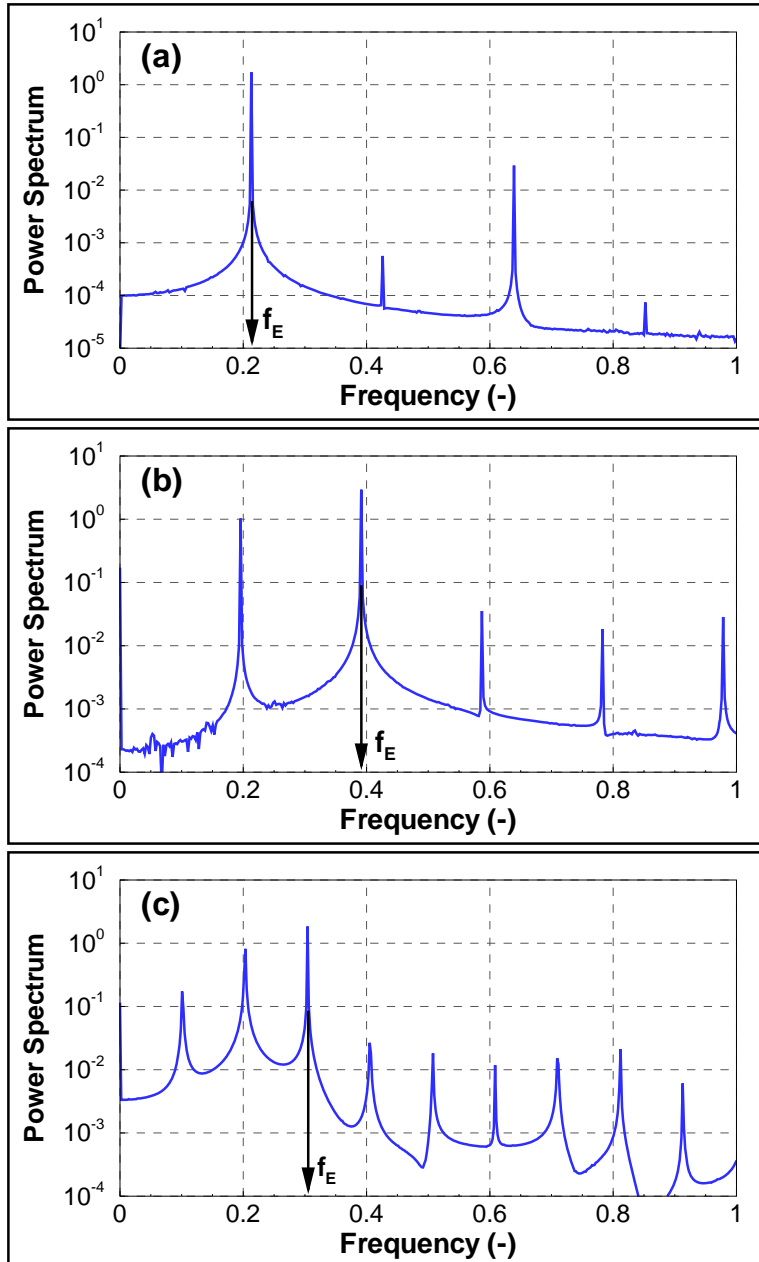


Figure 5.4: Power spectra of C_L : (a) period-1 response at $F_E = 0.98$, (b) period-2 response at $F_E = 1.80$, and (c) period-3 response at $F_E = 1.40$.

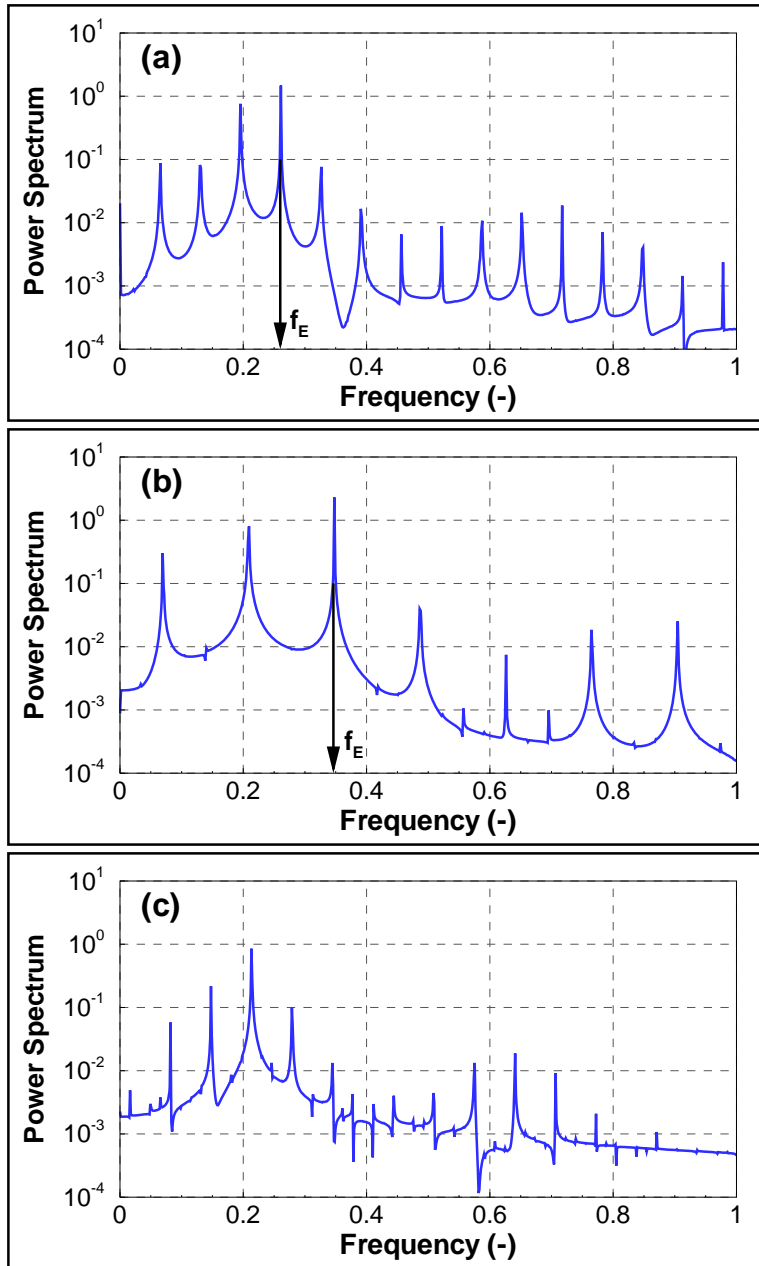


Figure 5.5: Power spectra of C_L : (a) period-4 response at $F_E = 1.20$, (b) period-5 response at $F_E = 1.60$, and (c) period-9 response at $F_E = 0.68$.

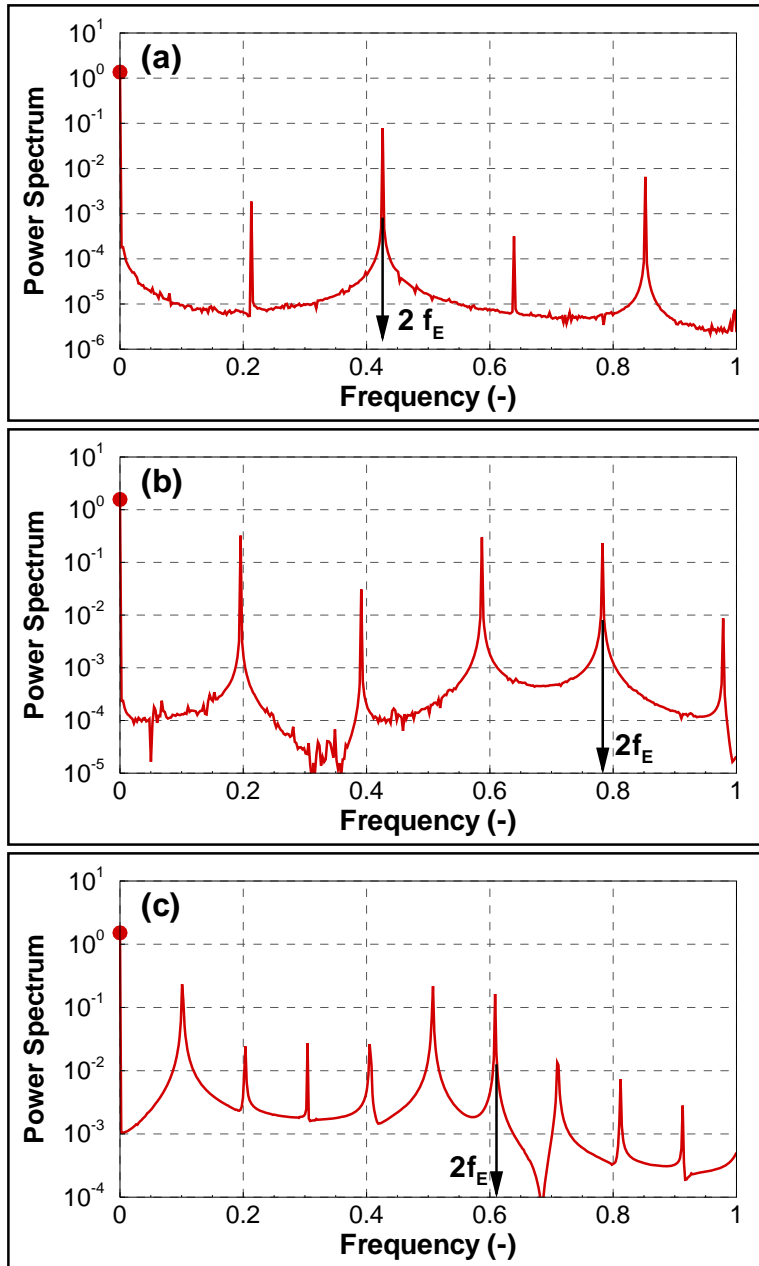


Figure 5.6: Power spectra of C_D : (a) period-1 response at $F_E = 0.98$, (b) period-2 response at $F_E = 1.80$, and (c) period-3 response at $F_E = 1.40$.

5.6 Phase Portraits and Poincaré Sections

Next, we use two-dimensional projections of the phase portraits (or the Lissajous curves) onto the $\dot{C}_L - C_L$ plane to characterize period- n responses. A periodic response corresponds to a closed orbit in the state space. In Figure 5.7, we show two-dimensional projections onto the $\dot{C}_L - C_L$ plane of the orbits of six period- n responses: period-1 at $F_E = 0.98$, period-2 at $F_E = 1.80$, period-3 at $F_E = 1.40$, period-4 at $F_E = 1.20$, period-5 at $F_E = 1.60$, and period-9 at $F_E = 0.68$. Clearly, the lower order orbits close on themselves, but it is not clear whether the period-9 orbit closes on itself. The period-1 response loops once before it closes on itself, whereas the period- n for $n \geq 2$ loops n times before it closes on itself.

As n increases (as in the period-9 case), one cannot recognize the number of peaks in a C_L cycle, whether the spikes below f_E are its subharmonics, the number of subharmonics, whether the orbit closes on itself, and the number of loops in the phase portrait. A more reliable method is needed, which is the one-sided Poincaré section of the orbits. They are generated by sampling the longtime time series every excitation period $T_E = 1/f_E$. In Figure 5.8, we show Poincaré sections of the portraits in Figure 5.7 using the same range for the variables. With such sampling, we eliminated the component at the sampling frequency from the response and reduced its dimension by one. Therefore, the single-loop orbit of the period-1 response is reduced to a single point as in Figure 5.8a, the two-loop orbit of the period-2 response is reduced to two points as in Figure 5.8b, and, in general, the the multi-loop orbit of a period- n response is reduced to n points falling on a closed curve as in Figures 5.8c-f. The locations of the n points in the Poincaré section are not unique and depend on the time at which sampling starts. Comparing Figure 5.8f with Figure 5.7f demonstrates the effectiveness of this method in identifying period- n responses with any n .

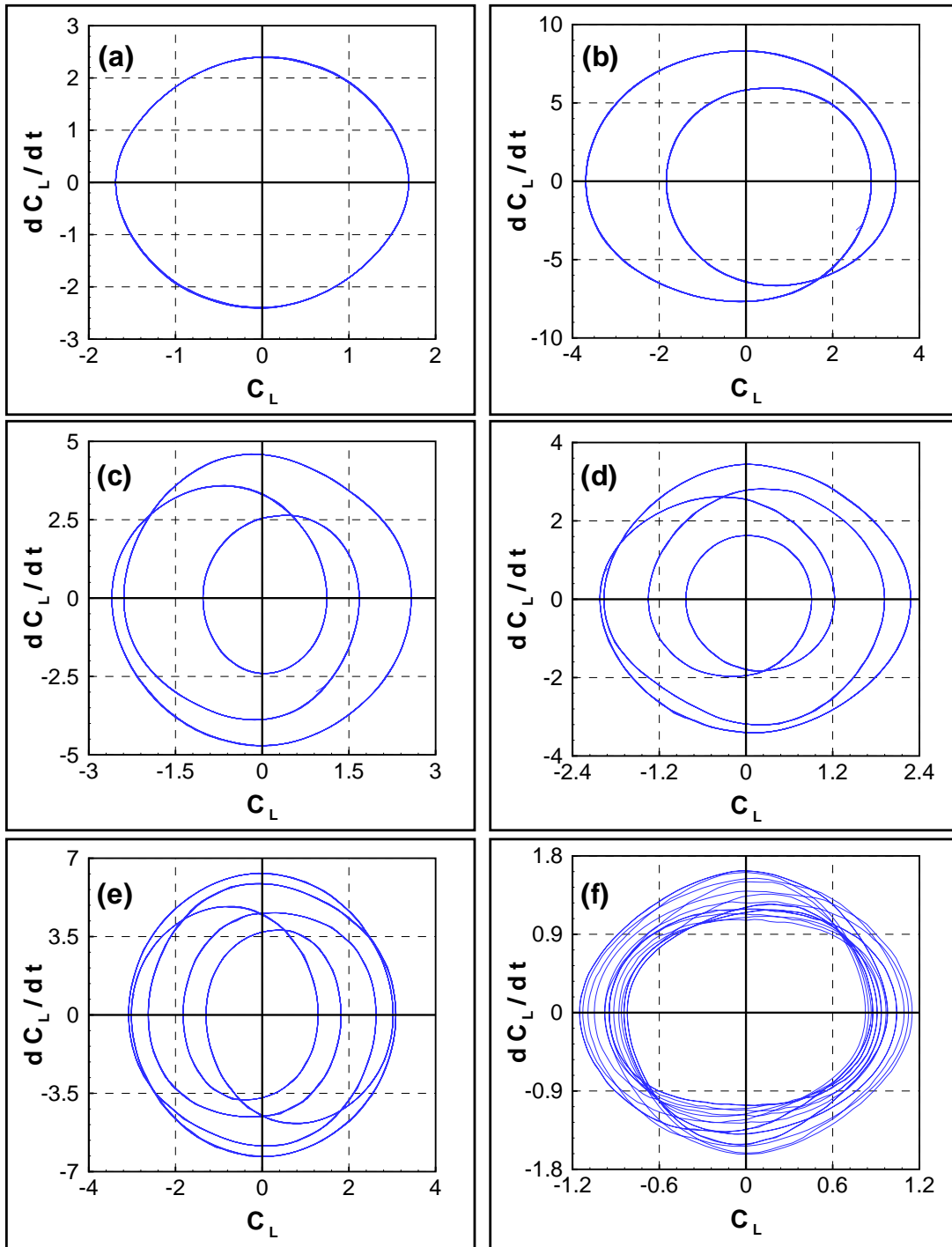


Figure 5.7: Orbits in the \dot{C}_L - C_L plane: (a) period-1 response at $F_E = 0.98$, (b) period-2 response at $F_E = 1.80$, and (c) period-3 response at $F_E = 1.40$, (d) period-4 response at $F_E = 1.20$, (e) period-5 response at $F_E = 1.60$, and (f) period-9 response at $F_E = 0.68$.

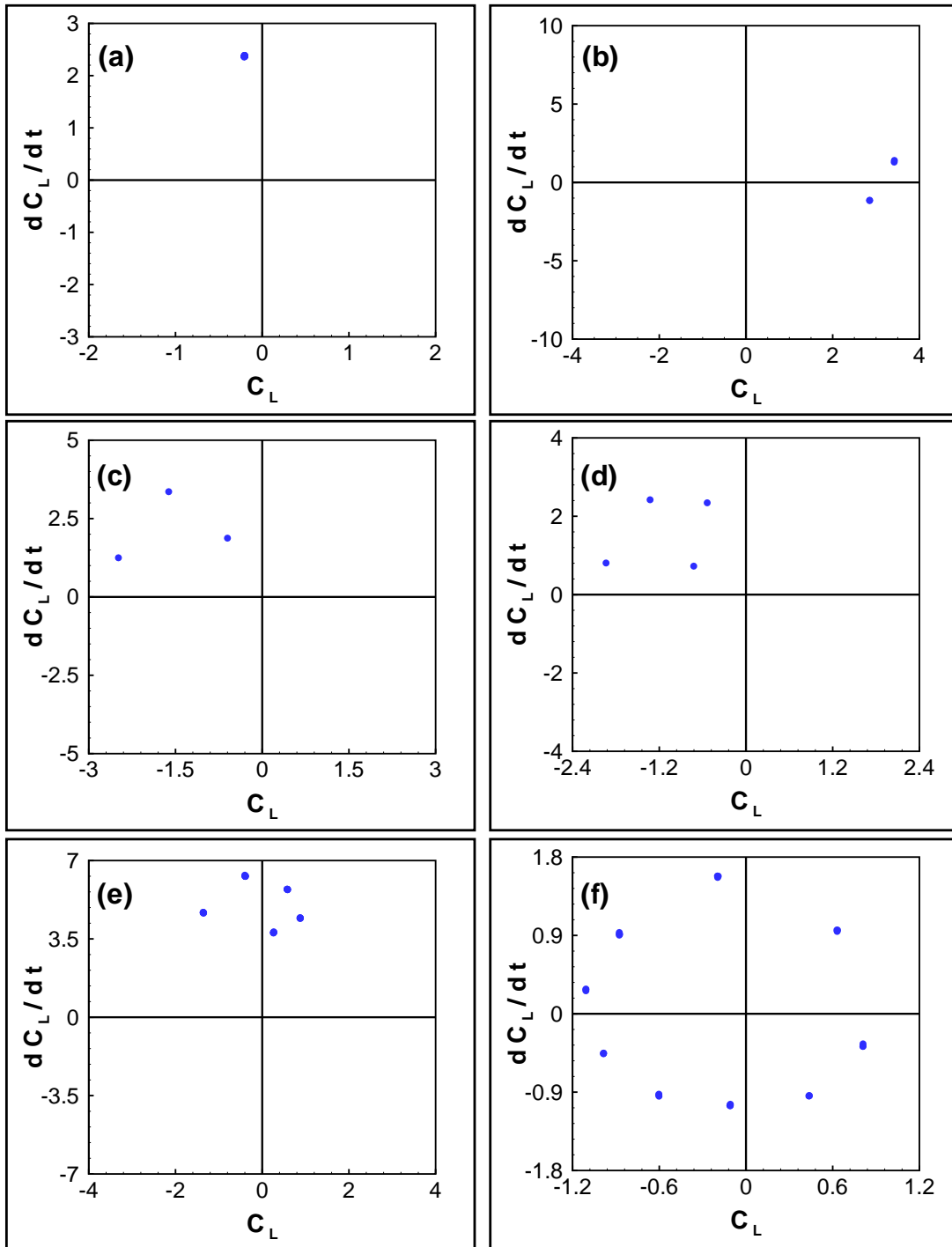


Figure 5.8: Poincaré sections of the orbits in Figure 5.7: (a) period-1 response at $F_E = 0.98$, (b) period-2 response at $F_E = 1.80$, and (c) period-3 response at $F_E = 1.40$, (d) period-4 response at $F_E = 1.20$, (e) period-5 response at $F_E = 1.60$, and (f) period-9 response at $F_E = 0.68$. The axes limits are the same as those in Figure 5.7.

Next, we examine the choice of the Poincaré sections. Specifically, we consider Poincaré sections in the C_L-C_D plane rather than the \dot{C}_L-C_L plane. We show in Figure 5.9 the C_L-C_D orbits for the period- n responses examined in Figures 5.7 and 5.8. Each loop in the \dot{C}_L-C_L plane corresponds to two loops in the C_L-C_D plane, which is a consequence of the two-to-one frequency relationship between C_L and C_D as demonstrated, for example, by Figures 5.4a and 5.6a. This makes the projections onto the C_L-C_D phase plane less suitable for characterizing period- n responses. On the other hand, the Poincaré sections in the C_L-C_D plane (shown in Figure 5.10) are as useful as those in the \dot{C}_L-C_L plane because they have the same number of points, which means that two loops of a C_L-C_D orbit correspond to a single point in the respective Poincaré section.

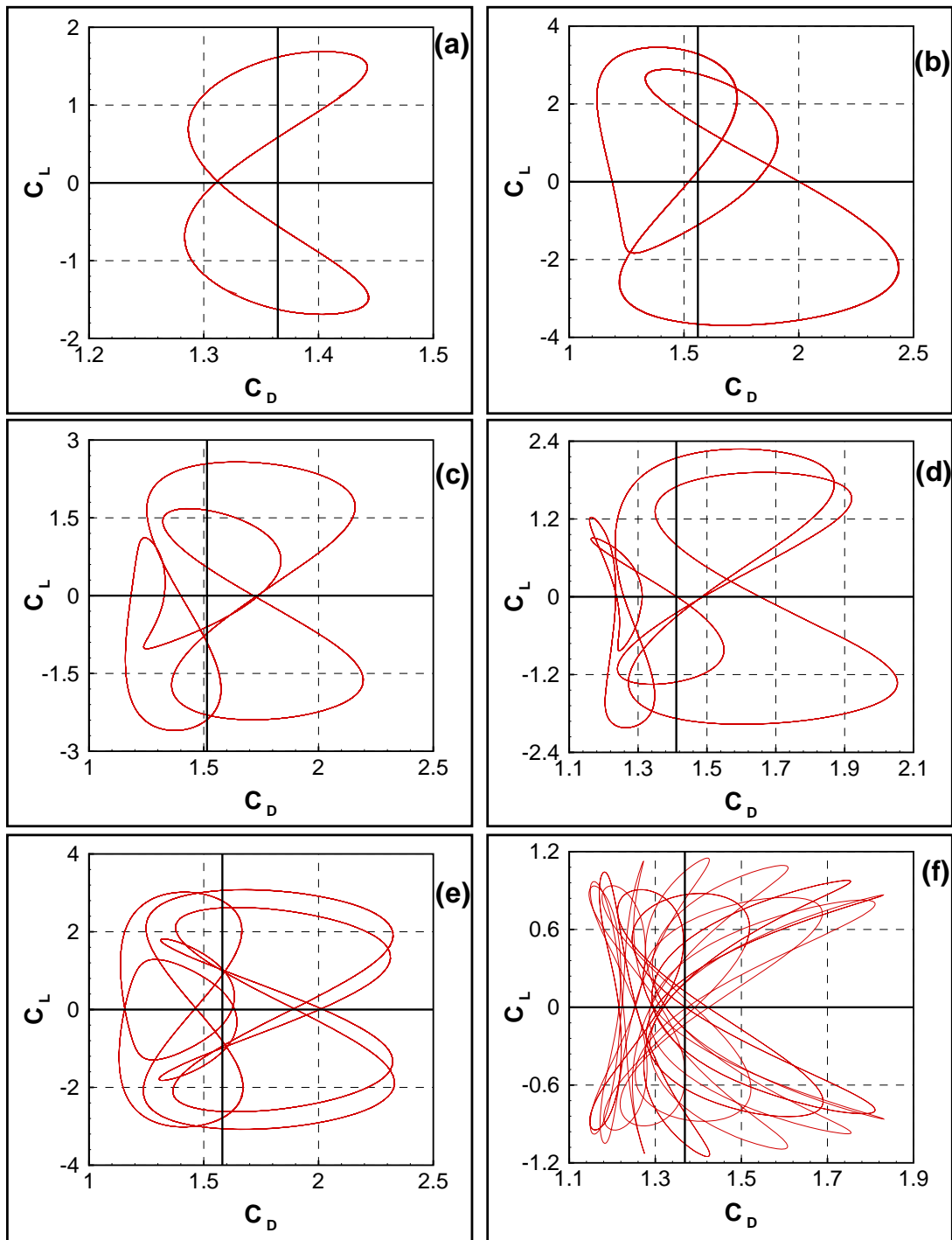


Figure 5.9: Orbits in the C_L - C_D plane: (a) period-1 response at $F_E = 0.98$, (b) period-2 response at $F_E = 1.80$, and (c) period-3 response at $F_E = 1.40$, (d) period-4 response at $F_E = 1.20$, (e) period-5 response at $F_E = 1.60$, and (f) period-9 response at $F_E = 0.68$.

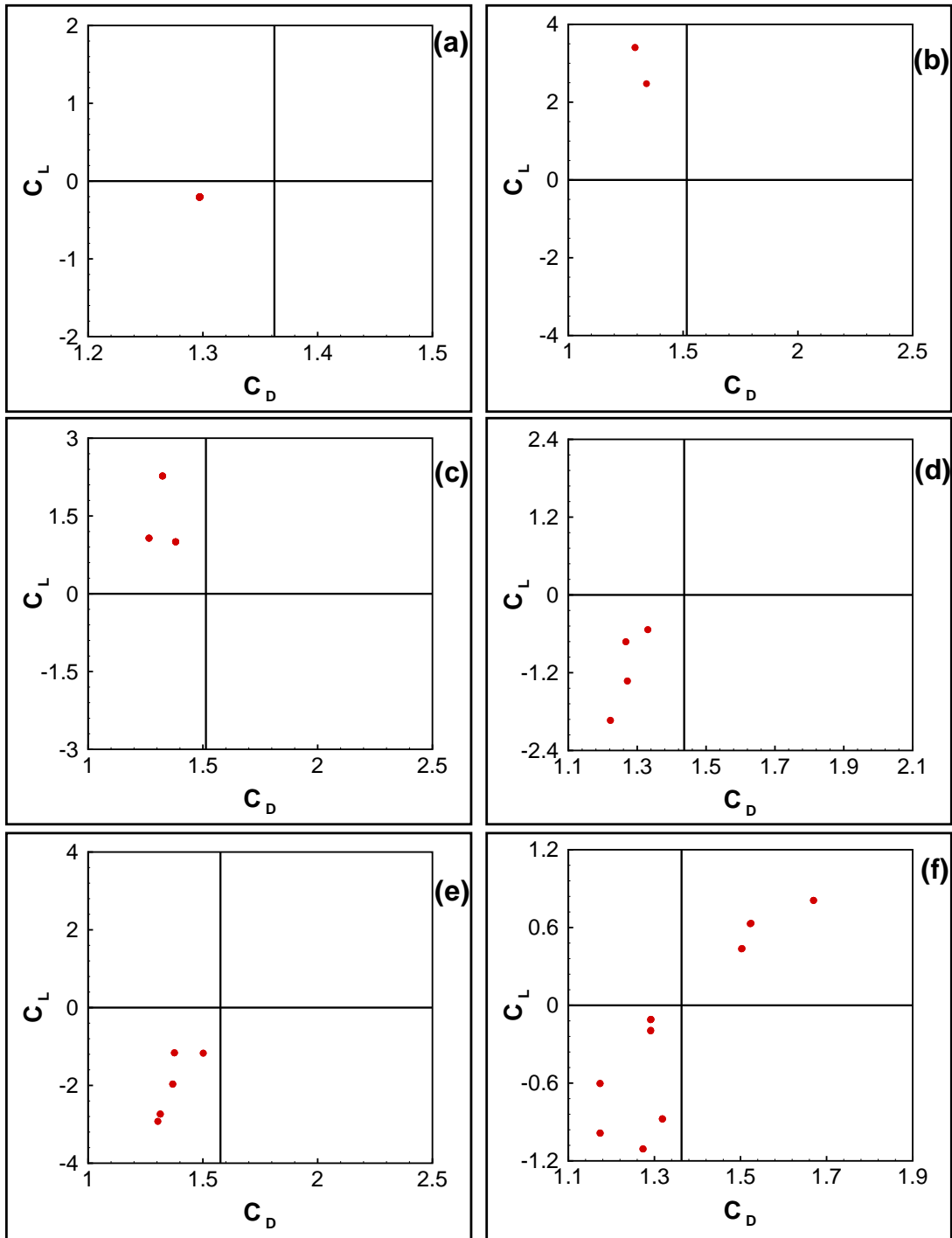


Figure 5.10: Poincaré sections of the orbits in Figure 5.9: (a) period-1 response at $F_E=0.98$, (b) period-2 response at $F_E=1.80$, (c) period-3 response at $F_E=1.40$, (d) period-4 response at $F_E=1.20$, (e) period-5 response at $F_E=1.60$, and (f) period-9 response at $F_E=0.68$. The axes limits are the same as those in Figure 5.9.

5.7 Quasiperiodic versus Chaotic Responses

A slight increase or decrease in the excitation frequency from a particular value that corresponds to a period- n response changes it to a quasiperiodic one, which we examine next along with chaotic responses and investigate the tools that discriminate between them. To this end, we selected two quasiperiodic responses (at $= 0.77$ and $= 1.00$) and two chaotic responses (at $= 1.10$ and $= 1.30$). We apply the same tools used to characterize period- n responses, especially their power spectra and Poincaré sections. So, we start with the longtime history for C_L , its power spectrum, and then the projection of its phase portrait and Poincaré section onto the \dot{C}_L - C_L and C_L - C_D planes.

We show the time series of C_L for the two quasiperiodic responses in Figures 5.11a and 5.11b and for the two chaotic responses in Figures 5.11c and 5.11d. The common feature in these four figures is the presence of many sinusoids, resulting in complex time series. Whereas a quick look at Figures 5.11a and 5.11d might suggest that they correspond to period- n responses, careful examination reveals that there is actually no robust period at which either of these responses is repeated as was the case in Figures 5.2b and 5.2c. Also, there is a beating behavior in Figure 5.11c that looks similar to the one in Figure 5.11b. This can lead to a mistaken deduction that both responses are of the same type.

In Figure 5.12, the spectra of C_L for the same cases are shown. The fact that the spectra in Figures 5.12a and 5.12b feature many discrete spikes suggest that they correspond to either period- n or quasiperiodic responses, depending on whether the spikes are commensurate or incommensurate with f_E . Because it would be difficult to accurately compute the locations of the discrete spikes, the power spectra would not be sufficient to conclude that these responses are quasiperiodic. On the other hand,

the broadband character of the spectra in Figures 5.12c and 5.12d suggest that they correspond to chaotic responses.

Because the orbits or trajectories of quasiperiodic and chaotic responses do not close on themselves, phase portraits are not useful to discriminate between them or to discriminate them from period- n responses with large n . Therefore, we turn to Poincaré sections. In these sections, period- n responses correspond to n discrete points, quasiperiodic responses correspond to infinitely many points falling on a closed curve, and chaotic responses correspond to neither a finite number of points nor infinitely many points falling on a closed curve. Because each of the Poincaré sections in Figures 5.13a and 5.13b is an infinite number of points falling on a closed curve, their corresponding responses are quasiperiodic. On the other hand, because each of the Poincaré sections in Figures 5.13c and 5.13d is neither a finite number of points nor an infinite number of points falling on a closed curve, the corresponding responses are chaotic, thereby confirming the conclusion from their broadband spectra.

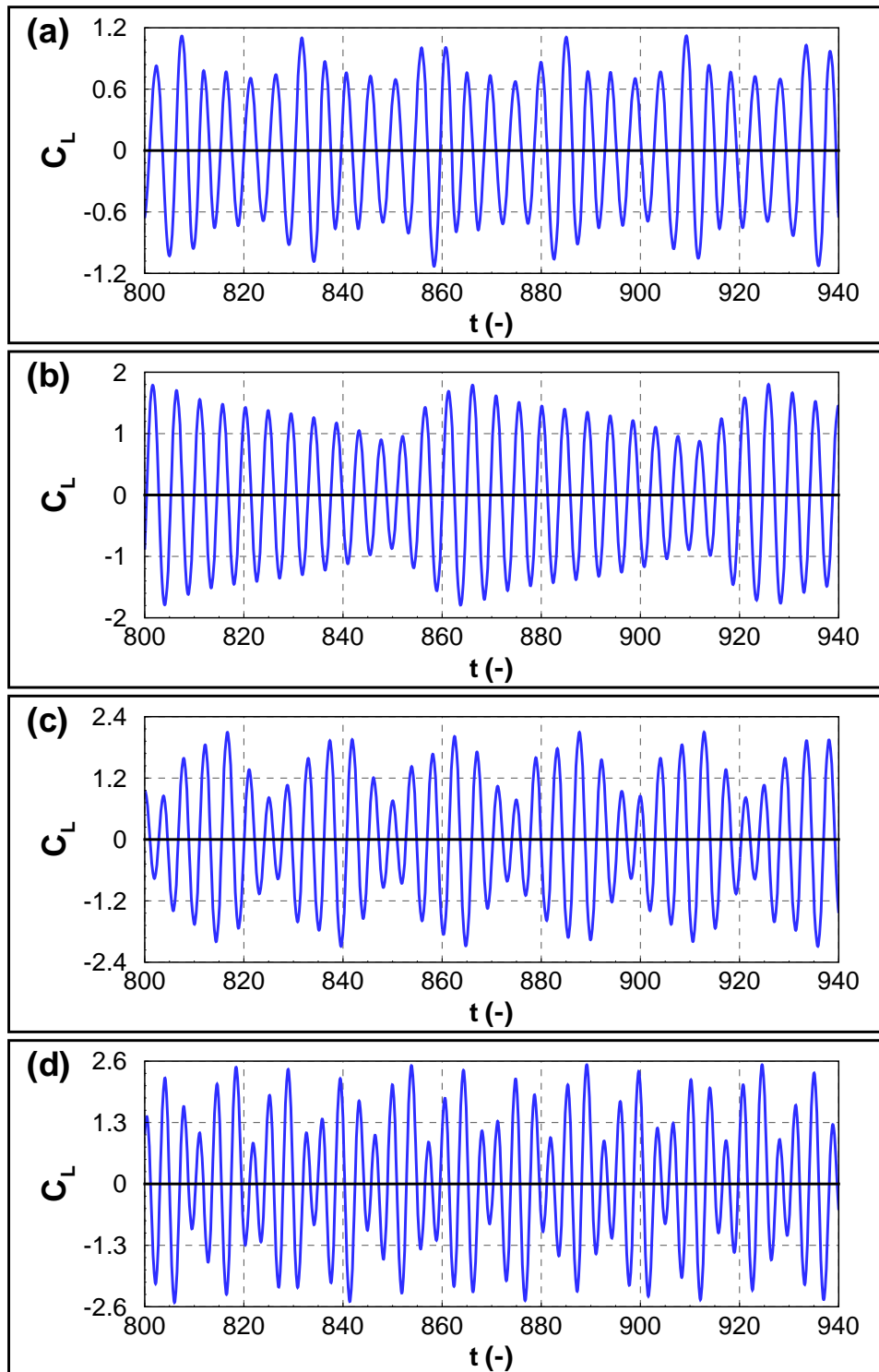


Figure 5.11: Longtime history of C_L : (a) quasiperiodic response at $F_E=0.77$, (b) quasiperiodic response at $F_E=1.00$, (c) chaotic response at $F_E=1.10$, and (d) chaotic response at $F_E=1.30$. All figures have the same time range.

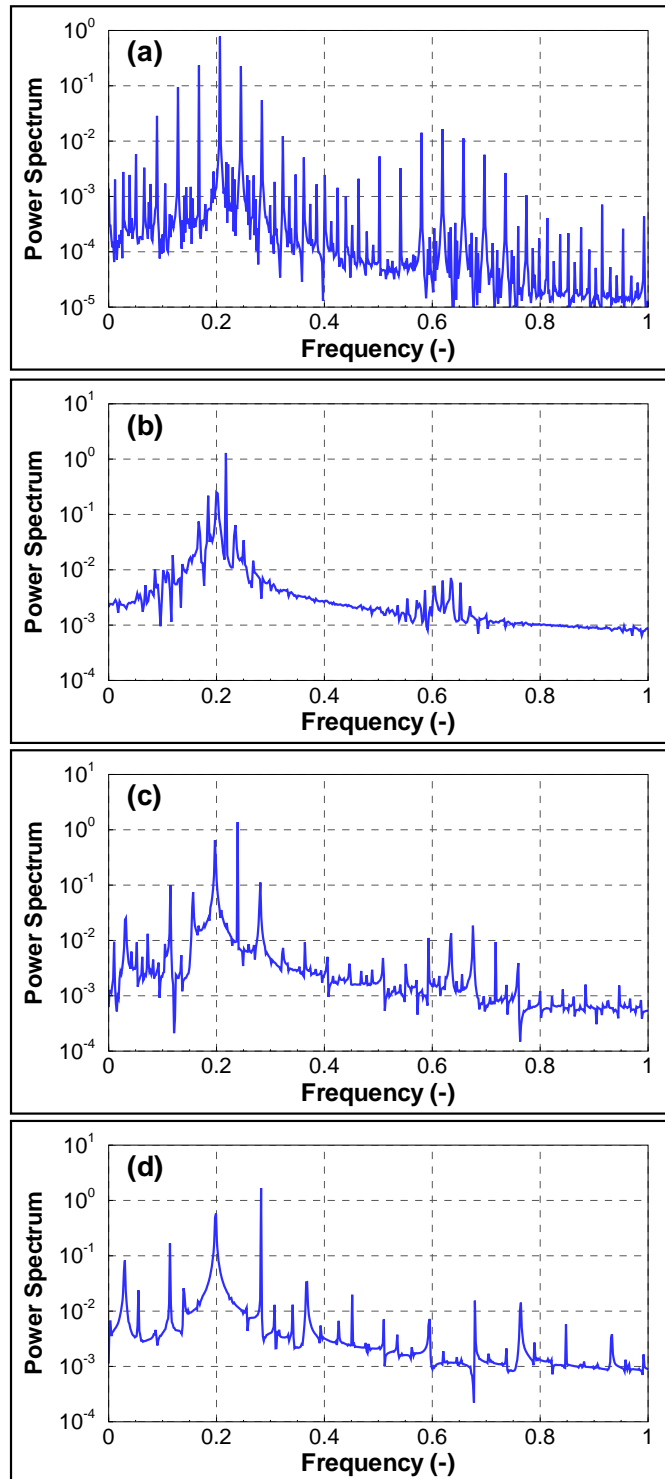


Figure 5.12: Power spectra of C_L : (a) quasiperiodic response at $F_E=0.77$, (b) quasiperiodic response at $F_E=1.00$, (c) chaotic response at $F_E=1.10$, and (d) chaotic response at $F_E=1.30$.

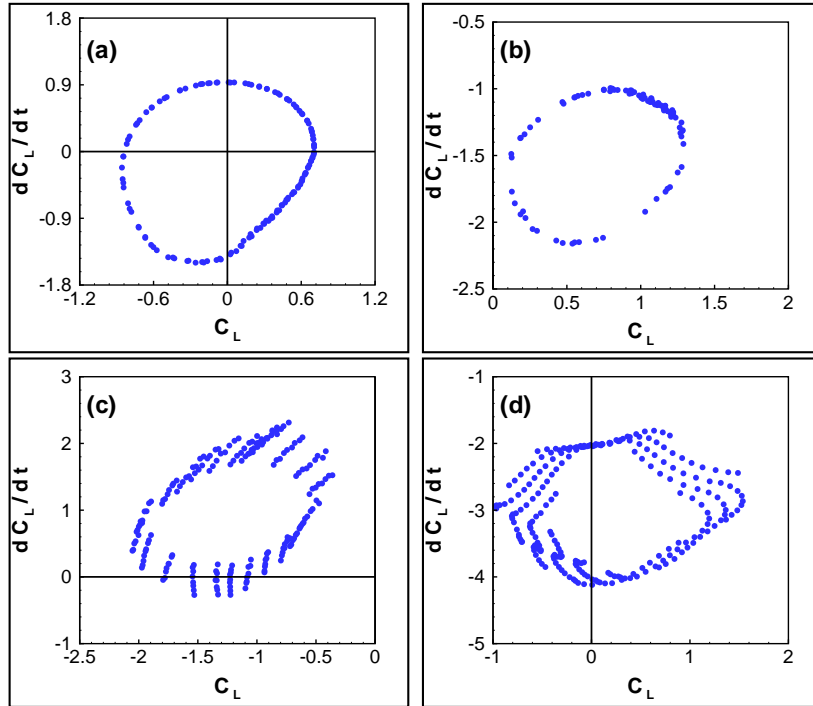


Figure 5.13: Poincaré sections of the orbits for: (a) quasiperiodic response at $F_E=0.77$, (b) quasiperiodic response at $F_E=1.00$, (c) chaotic response at $F_E=1.10$, and (d) chaotic response at $F_E=1.30$.

5.8 The Route to Chaos

We finally examine the route to chaos. To this end, we focus on the transition from a quasiperiodic response at $F_E=1.00$ (shown in Figure 5.14a) to a chaotic response at $F_E=1.10$ (shown in Figure 5.14d). The nearly closed curve in the \dot{C}_L - C_L Poincaré section at $F_E=1.00$ corresponds to a two-period quasiperiodic (or two-torus) response. It distorts and wrinkles at a slightly higher $F_E=1.02$, as shown in Figure 5.14b. Then the torus starts to break down, as shown in Figure 5.14c, at $F_E=1.06$. In Figure 5.14d, the broken torus is shown, where a chaotic response is taking place at $F_E=1.10$.

This sequence means that the route to chaos is quasiperiodic, with torus-breakdown scenario.

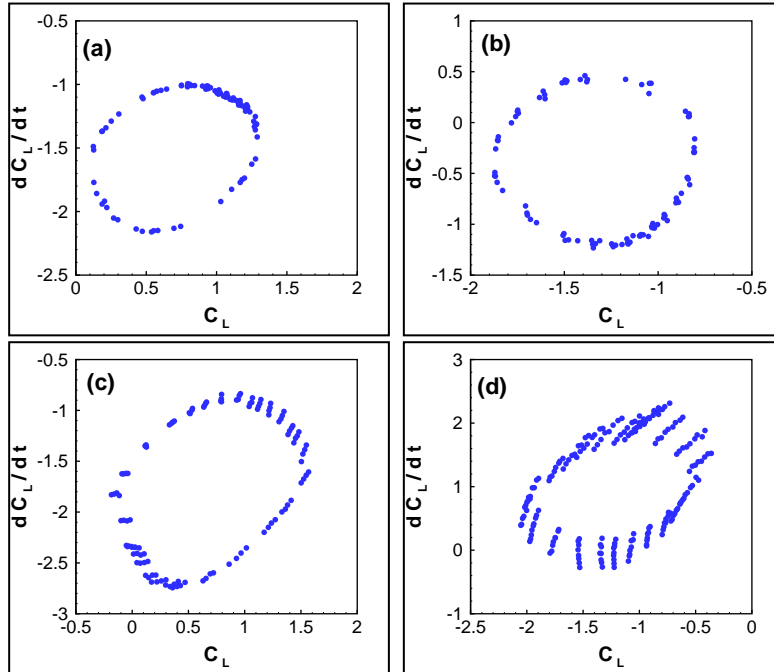


Figure 5.14: Poincaré sections showing the transition from a quasiperiodic response to a chaotic one. The route to chaos is demonstrated by four increasing values of F_E , namely, (a) 1.00, (b) 1.02, (c) 1.06, and (d) 1.10.

Chapter 6

A Cylinder Driven in the Cross-Flow Direction with Different Frequency-Sweep Types

6.1 Synopsis

In the preceding chapter, we considered cross-flow motion of a cylinder over a wide range of frequencies. However, each frequency is isolated and corresponds to a simulation where the motion pattern is unchanged. Consequently, the jump down and multi-valuedness are missed and hence the *hysteresis* could not be predicted. This chapter focuses on the synchronization band but addresses changes in the frequency-response curves of the force coefficients when the cross-flow motion frequency is varied in four different fashions: stationary, quasistationary, discrete, and nonstationary. Because the motion acts as an excitation to the natural wake, we will refer to it as “forcing” and to its frequency as “forcing” frequency. In the stationary case (also

called sine dwell), the forcing frequency is incremented by a small amount and the simulation is carried out long enough for the transients to die out before it is incremented again. The resulting frequency-response curves are bent to the left, indicating a softening-type nonlinearity, and exhibit a region of two coexisting stable responses (i.e., *bistability*). This *bistability* causes jumps and *hysteresis*. In the quasistationary case, again the forcing frequency is incremented, but the simulation is not carried long enough for the transients to die out. Again, the resulting frequency-response curves are bent to the left, exhibit *bistability*, jumps, and *hysteresis*, but the width of the *hysteresis* region is narrower. In the discrete variation, the forcing frequency is again incremented, but the simulation starts from a cylinder at rest in a uniform flow. Consequently, the jump down and multi-valuedness are missed and hence the *hysteresis* could not be predicted (as in the preceding chapter). In the nonstationary case, the frequency is varied continuously in a linear fashion with different rates. The resulting frequency-response curve depends on the rate at which the forcing frequency is changed. We highlight the effects of these fashions on the *hysteresis* and *bistability* phenomena and provide interpretations, based on known behaviors of nonlinear systems, of reported observations of interest in previous studies in the literature.

6.2 Stationary Sweeps

We start with the results of the stationary sweep, which is also called sine dwell. In this case, we vary the forcing frequency in a piecewise continuous function and dwell on each frequency long enough for the transients to die out and the steady state to be reached. We increment the frequency during the simulation so that the initial condition for the simulation with the new frequency is the final state obtained in the

previous frequency. In experimental settings, either the oscillation frequency or the velocity of the incoming stream is varied. Either one will change the nondimensional forcing frequency. In our simulations, we avoid discontinuities in the cylinder motion because they are not realistic and do not occur in experimental settings. A discontinuity in the cylinder velocity after incrementing the frequency results in a fictitious sudden change in the no-slip boundary condition, which induces inaccuracies and additional transients at the beginning of the new frequency interval. The numerical results of Meneghini and Bearman (1996) exhibit sharp glitches in the lift and drag and subsequent transients caused by the discontinuity in the cylinder speed (thus discontinuity in the no-slip boundary condition). Moreover, the finite-volume based simulations of Siegel et al. (2006) also exhibit glitches when a cylinder motion is introduced as an active-control technique for the wake. To eliminate such discontinuity, Blackburn and Henderson (1999) implemented a phase-angle-adjustment algorithm to mimic the experimental behavior. However, no details were given about the performance of their algorithm and to what level the discontinuities in the cylinder motion were reduced.

In this study, we implemented an algorithm to eliminate such discontinuities as follows. We consider the case of incrementing the forcing frequency f_1 , which lasts until a nondimensional simulation time $t_{1,fin}$, to a subsequent frequency f_2 , which starts at $t_{1,fin} + \Delta t$ and ends at $t_{2,fin}$, where Δt is the nondimensional time step. Then, the cylinder motion is described as

$$Y(t) = Y_1(t) = A \sin(2 \pi f_1 t) \quad t_{1,fin} \geq t \quad (6.1)$$

$$Y(t) = Y_2(t) = A \sin(2 \pi f_2 [t + k\Delta t]) \quad t_{2,fin} \geq t \geq t_{1,fin} + \Delta t \quad (6.2)$$

where A is the nondimensional cylinder amplitude and k is an integer. The adjustment time $k\Delta t$ is chosen by minimizing the non-negative deviation function

$$\delta(f_1, f_2) \equiv |Y_2(t_{1,fin} + \Delta t) - Y_1(t_{1,fin} + \Delta t)| \quad (6.3)$$

We also keep $|f_1 - f_2|$ and Δt small so that $\delta(f_1, f_2)$ is practically zero. Maintaining continuity of the displacement $Y(t)$ of the cylinder guarantees continuity of its velocity $\dot{Y}(t)$.

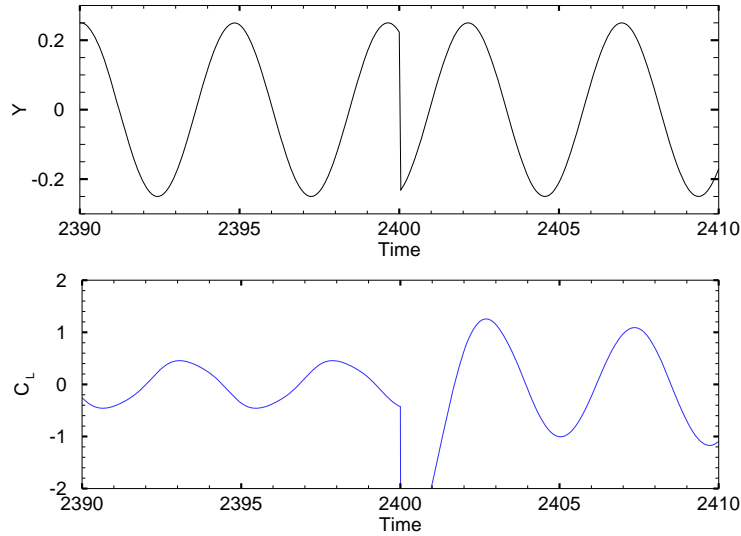


Figure 6.1: Time histories of the displacement and lift coefficient with a stationary forcing around a frequency-stepping instant (nondimensional time = 2,400) when the smoothing method is not used.

To demonstrate performance of the smoothing algorithm and its important influence on the results for stationary sweeps, we select a frequency-stepping case starting from type-B attractor. The time histories of the displacement and velocity of the cylinder and the associated lift coefficient around a frequency-stepping instant are presented in Figures 6.1 and 6.2 without and with smoothing, respectively. In both figures, the forcing frequency is stepped down at a nondimensional time of 2,400. Comparing the

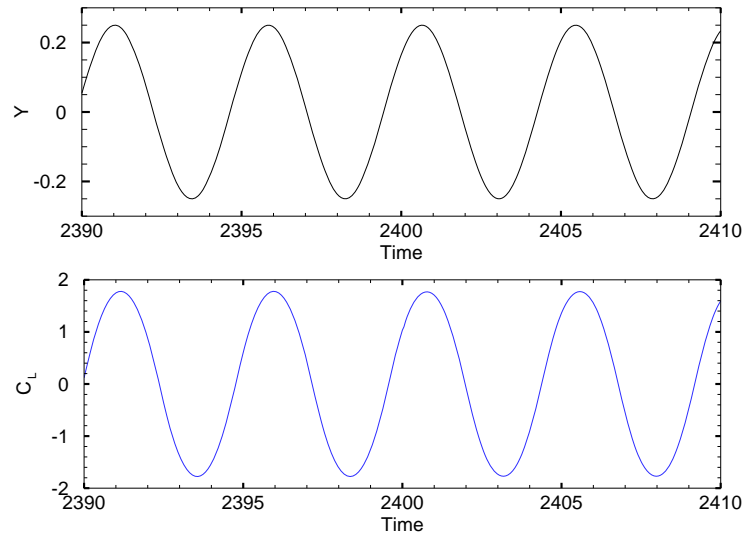


Figure 6.2: Time histories of the displacement and lift coefficient with a stationary forcing around a frequency-stepping instant (nondimensional time = 2,400) when the smoothing method is used.

two figures demonstrates the efficiency of the smoothing; the discontinuities in the displacement and velocity and hence the glitches in the lift are eliminated. Whereas visual inspection of Figure 6.2 suggests that there are no transients following the frequency stepping, there are small transients and hence we still need to wait long enough before the next frequency stepping. It follows from Figure 6.1 that the lift before the frequency stepping is of type-A (small), whereas it follows from Figure 6.2 that it is of type-B (large). This is due to an expedited transition from the type-B attractor to the type-A attractor resulting from the impulsive transients at the previous frequency stepping. The forcing frequency before the stepping is 0.208052, which belongs to the *hysteresis* region and the coexistence of two attractors coexist. This is another and more important effect of spurious discontinuities in the motion history besides the need to wait long enough for the transients to die out completely.

The stationary frequency-response curves for the lift and mean drag coefficients are presented in Figures 6.3 and 6.4, respectively. In the synchronized region, the lift coefficient exhibits *bistability* and hence *hysteresis*. A small-amplitude (type-A mode or attractor) stable branch coexists with a large-amplitude (type-B mode or attractor) stable branch. The former occurs at lower frequencies, whereas the latter occurs at higher frequencies, indicating a softening-type nonlinearity. Each attractor has its basin of attraction, which is the set of initial conditions for which the solution asymptotically tends to that attractor. Theoretical analysis suggests the existence of a third unstable branch (saddles) connecting the two stable branches. Whereas this saddle branch corresponds to the locus of solutions to the Navier-Stokes equations, it is unrealizable numerically and cannot be determined experimentally. According to methods of nonlinear dynamics, the stable manifolds of the saddle divide the state space into two regions, which are the basins of attraction of the two stable solutions.

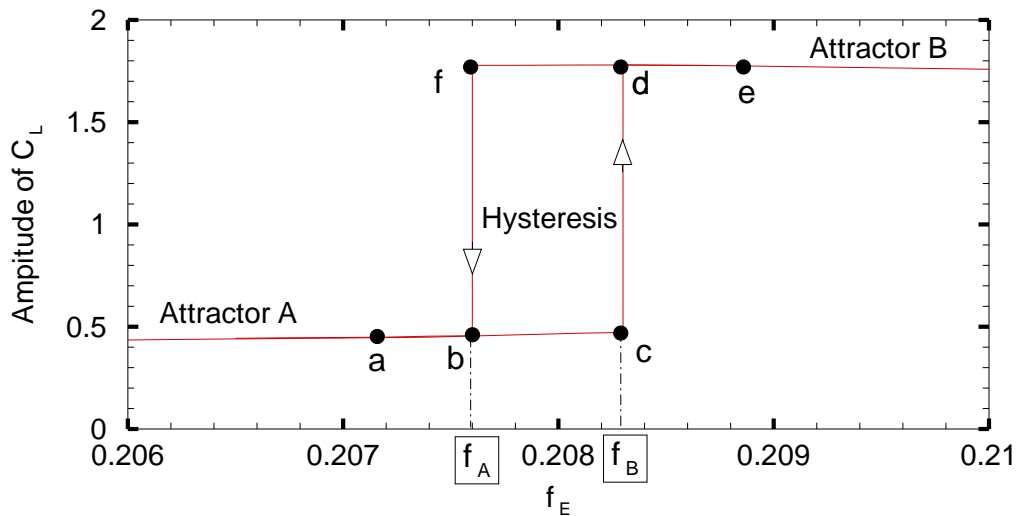


Figure 6.3: Frequency-response curves for the lift coefficient with a stationary forcing.

Starting the simulation at a frequency corresponding to the small-amplitude attrac-

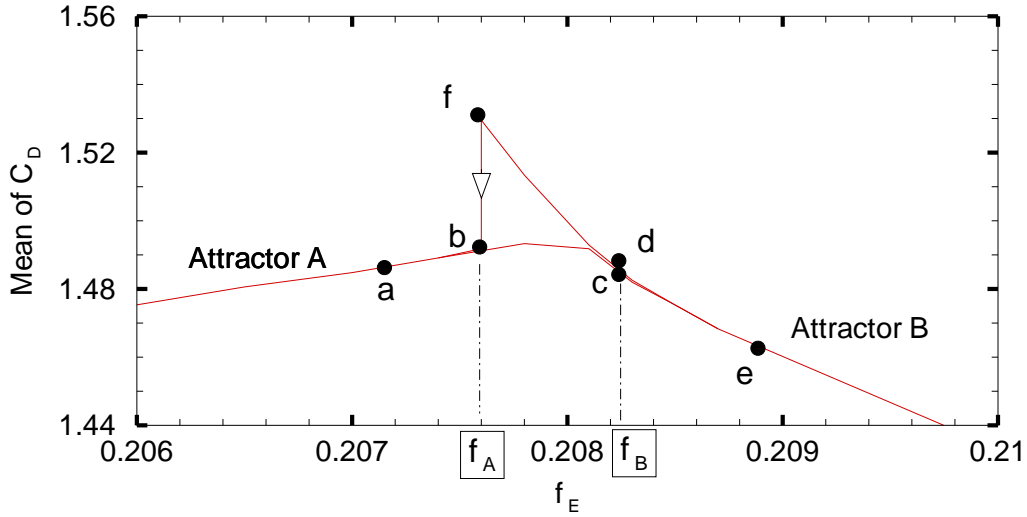


Figure 6.4: Frequency-response curves for the drag coefficient with a stationary forcing.

tor (such as point a in Figure 6.3) and increasing it by increments of 2.2×10^{-4} every 600 time units, we find that the lift increases slowly until the frequency reaches $f_B = 0.20827$. As the frequency is increased further, a jump-up from the small-amplitude branch to the large-amplitude branch takes place (from point c to point d in Figure 6.3). As the frequency is increased further, the lift decreases slowly but remains high. Starting the simulation at a frequency on the large-amplitude branch (such as point e in Figure 6.3) and slowly decreasing it, we find that the lift increases slowly until it is decreased below $f_A = 0.20762$, resulting in a jump-down of the lift from the large-amplitude branch to the small-amplitude branch (from point f to point b in Figure 6.3). As the forcing frequency is decreased further, the lift decreases slowly following the small-amplitude branch.

We examine different characteristics of the lift and drag coefficients of the two attractors. We present in Figure 6.5 the time histories of the lift coefficient and the cylinder displacement for two cases corresponding to points b and f in Figure 6.3.

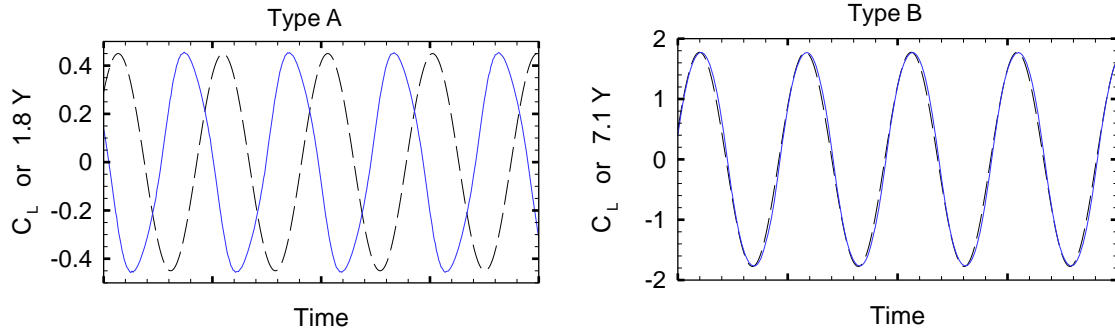


Figure 6.5: Time histories of the scaled cylinder motion (dashed line) and the lift coefficient (solid line) for type-B and type-A attractors. Each plot corresponds to a window of 20 time units.

In order to enhance the contrast between the two attractors, we scale the cylinder displacement $Y(t)$ oscillation such that its amplitude is equal to the amplitude of the lift coefficient. In addition to the remarkable difference in the amplitudes of the two attractors (a factor of four), the type-B attractor is in phase with $Y(t)$, whereas the type-A attractor is 125° degrees out of phase with $Y(t)$.

Projections of the two attractors onto the lift-displacement plane in Figure 6.6 are of special importance. These projections are presented in Figure 6.6. The B attractor is characterized by a curve that closes on itself every oscillation period, forming a single loop. This loop is squeezed and nearly a straight line. Because the enclosed area of this loop represents the nondimensional mechanical energy transferred to the flow from the cylinder over each oscillation period, this energy transfer seems to sustain this attractor and its associated vortex pattern. On the other hand, the A attractor is characterized by another trajectory that also closes on itself every oscillation period, but its loop has a finite enclosed area and its direction is reversed (counterclockwise). Therefore, for the type-A attractor, the flow is actually transferring energy to the

cylinder, which is reflected in vorticity attenuation in the wake as observed experimentally (Zdravkovich, 1982; Gu et al., 1994) and numerically (Marzouk and Nayfeh, 2008a).

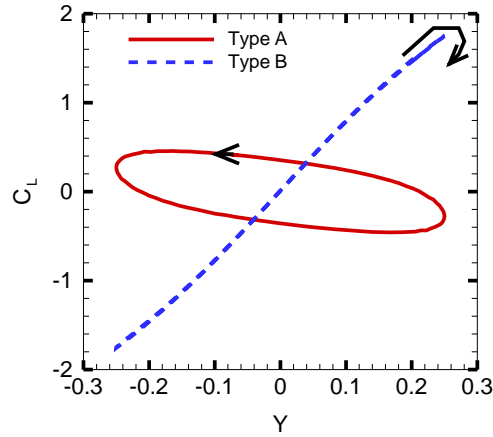


Figure 6.6: Lissajous curves in the lift-displacement plane for type-B and type-A attractors. Directions of the curves are indicated.

The Lissajous curves in the lift-drag plane form a figure eight as a result of the 2:1 frequency relationship between the drag and the lift. Again, the curves of type-A and type-B attractors differ not only in terms of their size, but also in their direction as shown in Figure 6.7. In the former case, the amplitude of the positive or negative lift coefficient continues to increase after the drag coefficient reaches its maximum. In the latter case, the maximum amplitude of the lift coefficient coincides with the maximum drag coefficient, and they simultaneously decrease afterwards. We found that the direction of the type-A Lissajous curve is the same as what we obtained for the case of a fixed cylinder.

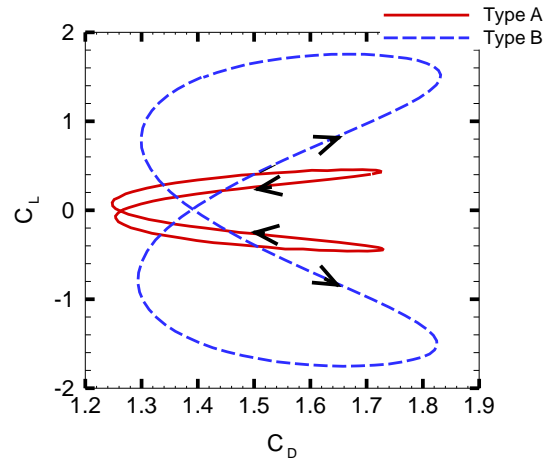


Figure 6.7: Lissajous curves in the lift-drag plane for type-B and type-A attractors. Directions of the curves are indicated.

6.3 Quasistationary Sweeps

If the interval of any forcing frequency is shortened such that the transients did not die out, then the results will not be robust and the jump locations will be erroneous. This is because the transients might produce initial conditions lying in the basin of attraction of the other attractor, thereby expediting the jump. We refer to such cases as quasistationary sweeps.

To demonstrate the difference between this sweep and the stationary one, we present in Figures 6.8 and 6.9 the frequency-response curves obtained for the lift and drag coefficients, when the forcing frequency is incremented every 300 time units. Comparing these curves to their stationary counterparts in Figures 6.3 and 6.4, we conclude that the width of the *hysteresis* is reduced to two thirds of that of the stationary case. Such influence of the dwell time on the forcing frequency should be examined in experimental and numerical studies for similar problems to ensure that the results are stationary and not quasistationary. Blackburn and Henderson (1999) reported a

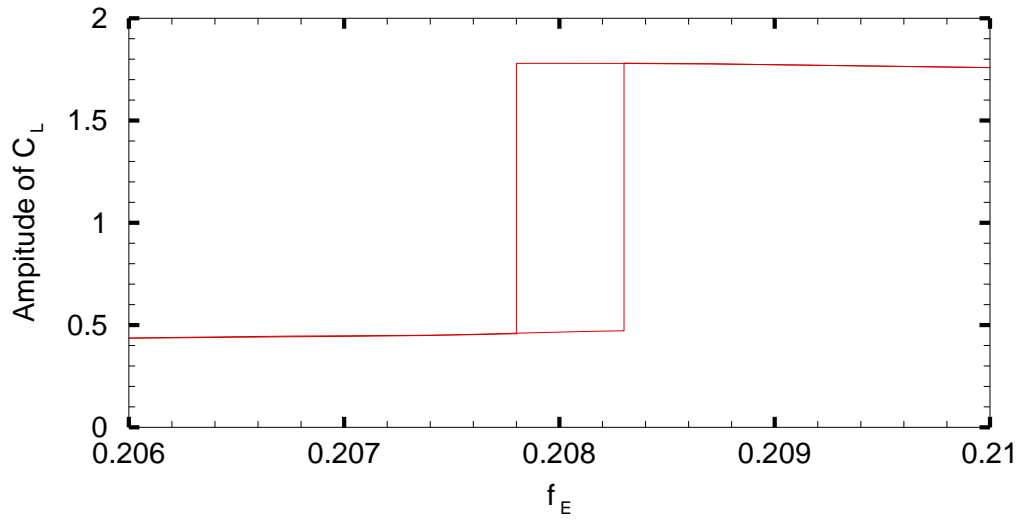


Figure 6.8: Frequency-response curves for the lift coefficient with a quasistationary forcing.

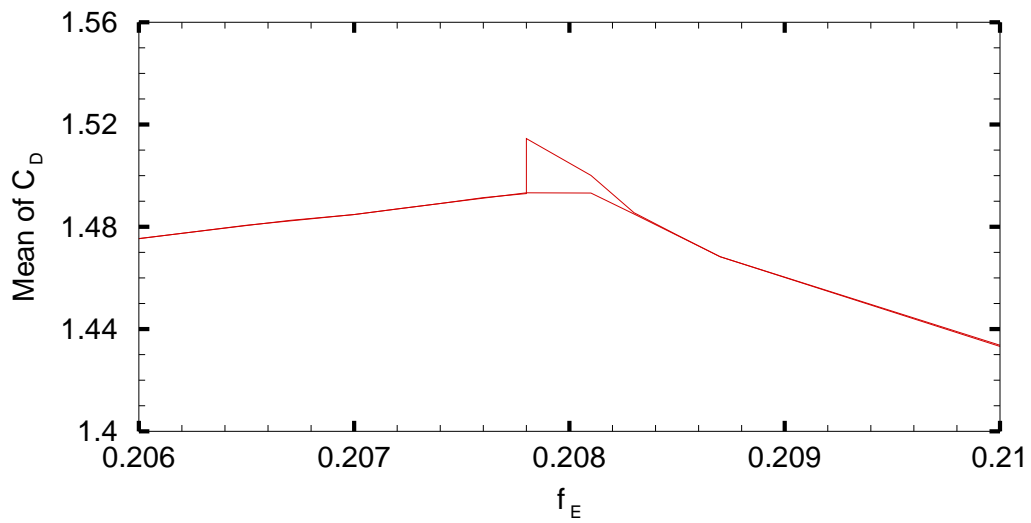


Figure 6.9: Frequency-response curves for the drag coefficient with a quasistationary forcing.

range of weakly chaotic regime within the lock-in spectrum in their applied sine-dwell forcing. The forcing frequency was incremented approximately every 50 cycle, which

is in the order of 250 time units. Therefore, their results might be quasistationary rather than stationary, which explains the weakly chaotic range. This is supported by the fact that this range takes place at the boundary of their reported *hysteresis*. Therefore, this range can be actually part of unresolved *hysteresis* and the reported response is a transient, which is expected to settle at one attractor but the dwell time is insufficient for this to be completed.

6.4 Discrete Sweeps

If the forcing frequency is constant over the entire simulation, starting from a cylinder at rest and uniform flow, we do not find the *hysteresis*. For forcing frequencies below f_A , the steady-state solution locks onto the type-A attractor; and for forcing frequencies above f_B , it locks onto the type-B attractor. In the *hysteresis* interval between f_A and f_B , both attractors coexist, and the initial conditions determine the steady-state solution. We refer to these cases by discrete forcing, and the corresponding frequency-response curves of the lift and drag coefficients are presented in Figures 6.10 and 6.11, respectively. At the ends of these curves, the locked solution loses stability and becomes aperiodic as indicated in Figure 6.11, where an abrupt change takes place in the discrete frequency-response curve for the mean of the drag coefficient at these two instability points.

In previous experiments (Carberry et al., 2001) of discrete forcing at a higher Re of 2,300, it was observed that there is a very narrow range of forcing frequencies near the frequency that separates the two branches of the frequency-response curve of the lift. Over this range, C_L has a large amplitude for a certain interval of time and a small amplitude over another interval even though the forcing frequency is unchanged. We

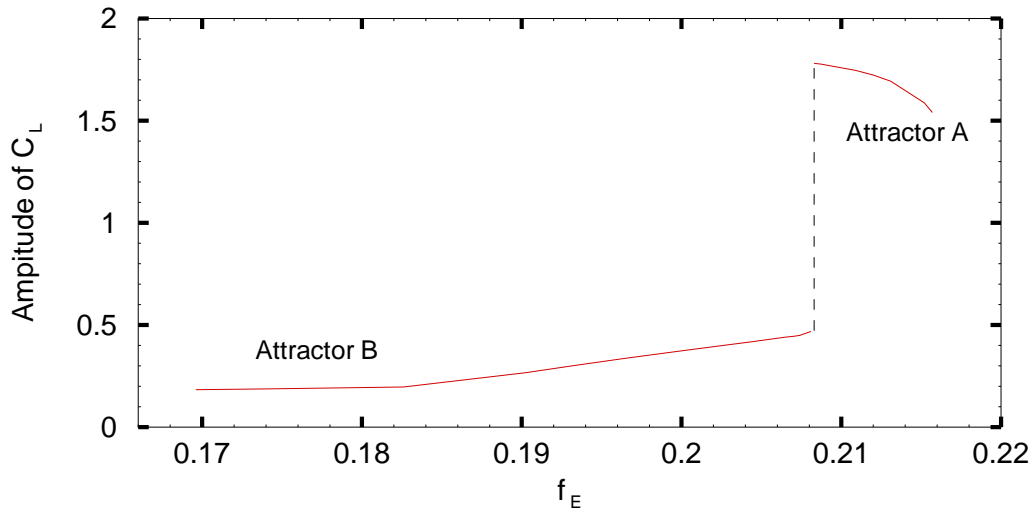


Figure 6.10: Frequency-response curve for the lift coefficient in the case of discrete forcing.

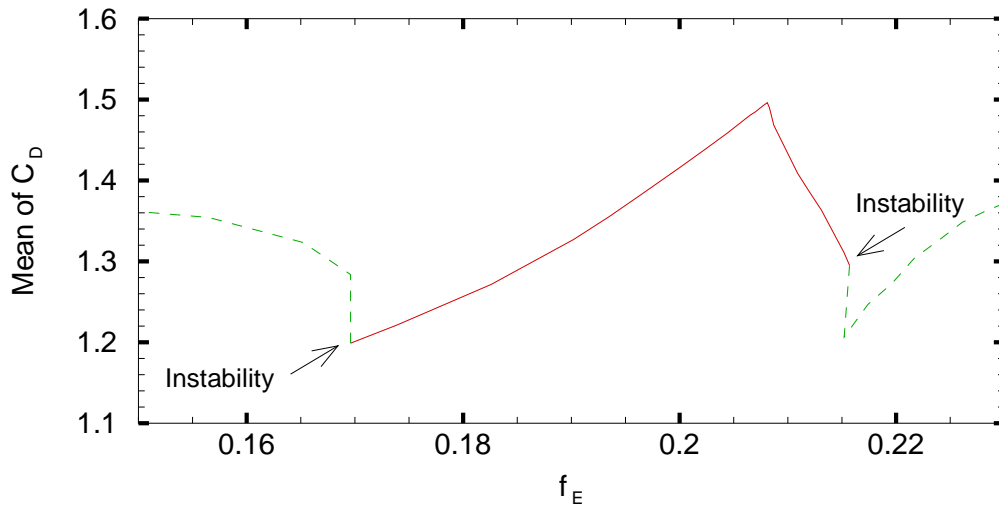


Figure 6.11: Frequency-response curve for the drag coefficient in the case of discrete forcing. The dashed lines correspond to aperiodic time histories of the drag coefficient.

found a similar behavior. We interpret this by an initial condition of the flow and C_L that lies in the basin of attraction of the type-B attractor but near the basin of attraction of the type-A attractor. A large basin of attraction of the type-A attractor

causes the transients of C_L to be close to the type-B attractor.

6.5 Nonstationary Sweeps

Sweeping the forcing frequency as a linear function of time is referred to as nonstationary (or continuous) forcing. We investigate its effect on the frequency-response curve under different rates of forward and backward sweeps when the frequency is increased or decreased gradually across the ‘virtual’ stationary jump locations (i.e., which would happen in case of stationary forcing). The stationary jumps are replaced by nonstationary variation, where the lift switches gradually from the small-amplitude attractor to the large-amplitude attractor and vice versa. This mechanism is denoted by *passage through resonance*. In the forward sweep, the amplitude of the lift coefficient overshoots the stationary curve, oscillates around it, and finally settles on it. Decreasing the rate of sweep results in a decrease in the overshoot and a decrease in the frequency at which it occurs. Similarly, in the backward sweep, the jump-down is replaced by a gradual switch from the upper branch to the lower branch, an oscillation around the lower branch, and a final settlement on it. The frequency-response curves of the lift coefficient obtained for slow and fast sweeps are compared to the stationary frequency-response curve in Figure 6.12. We considered two absolute rates of frequency sweeps $|df/dt|=1\times 10^{-5}$ and 2×10^{-5} for each of the forward and backward sweeps. Here, we do not have access to the saddle, therefore we approximate it by a straight line connecting the two ends of the stable branches for illustration.

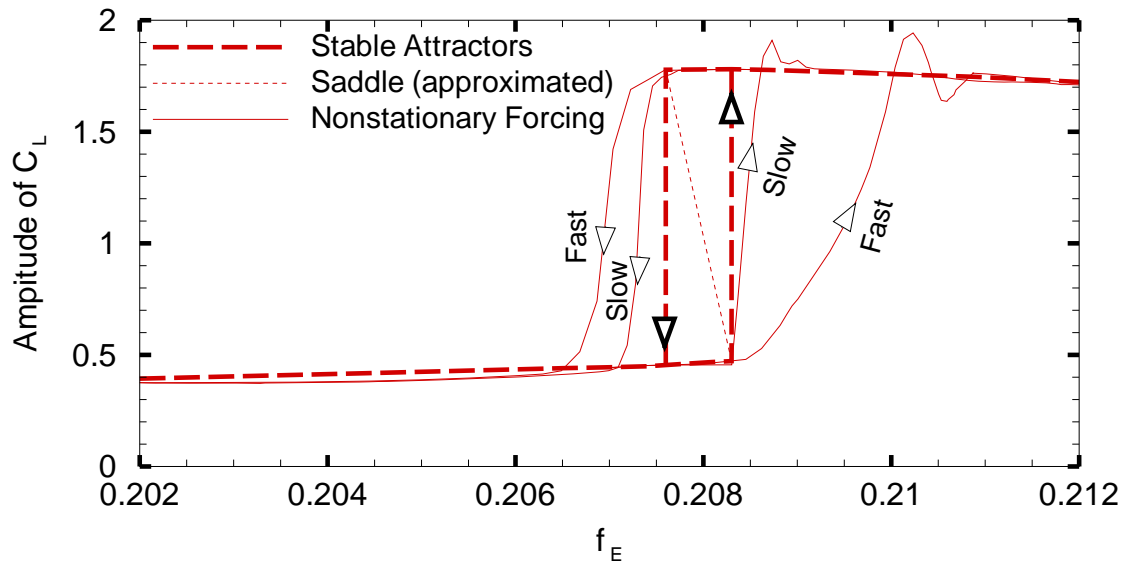


Figure 6.12: Frequency-response curves for the lift coefficient with stationary forcing and different nonstationary forcing.

Chapter 7

Wake Changes Due to In-Line Cylinder Motion

7.1 Synopsis

In this chapter, we study in detail the flow field around a cylinder in a uniform stream while undergoing in-line harmonic motion (rather than the cross-flow one as in previous chapters). Below a critical forcing frequency, the lift and drag responses can be period- n , quasiperiodic, or chaotic. Above this critical frequency, they both become synchronized with the cylinder motion. The lift nearly vanishes due to instantaneous symmetry in the wake, the mean drag drops and saturates at a value independent of the motion frequency, and the oscillatory drag is quadratically dependent on it. We relate these features to changes in the wake and the surface-pressure distribution. We examine the effects of the amplitude of motion and the Reynolds number on the critical frequency. Second- and higher-order spectral analysis shows remarkable changes in the linear and quadratic coupling between the lift and drag when synchronization takes place, which destroys the two-to-one coupling between them that exist in the

case of no motion or synchronization due to cross-flow motion. We contrast some features of the synchronized responses in the case of in-line motion to that in the case of cross-flow motion.

7.2 In-Line Motion

The motion of the cylinder is described by the following sine function:

$$X(t) = \frac{A}{D} \sin(2\pi f_E t) \quad (7.1)$$

where A/D and f_E are the nondimensional amplitude and cyclic frequency of the motion, respectively. We investigate several flow properties over a wide range of f_E while fixing A/D at 0.20. This value allows us to compare the flow features for this case with those obtained for a cylinder with cross-flow motion at the same amplitude and Re (Marzouk and Nayfeh, 2008c). The majority of the results correspond to $Re=500$; the others correspond to $Re=300$.

7.3 Effects of Motion Frequency

Synchronization is illustrated in Figure 7.1, which shows the ratio f_v/f_s as a function of the ratio f_E/f_s . The frequency f_v is the actual nondimensional vortex-shedding frequency, whereas f_s is the natural nondimensional vortex-shedding frequency (again, we found this to be 0.217). When $f_E \approx 2f_s$, shedding is synchronized at f_E . Hence, the graph of f_v/f_s with f_E/f_s is a straight line with unity slope; it starts at the critical value $f_E/f_s = 1.81$ and extends to $f_E/f_s=3.33$. Beyond this value, the synchronized shedding bifurcates and becomes nonsynchronized with less regular pattern and with asymmetric lift. We refer to this range of f_E as post-synchronization compared to

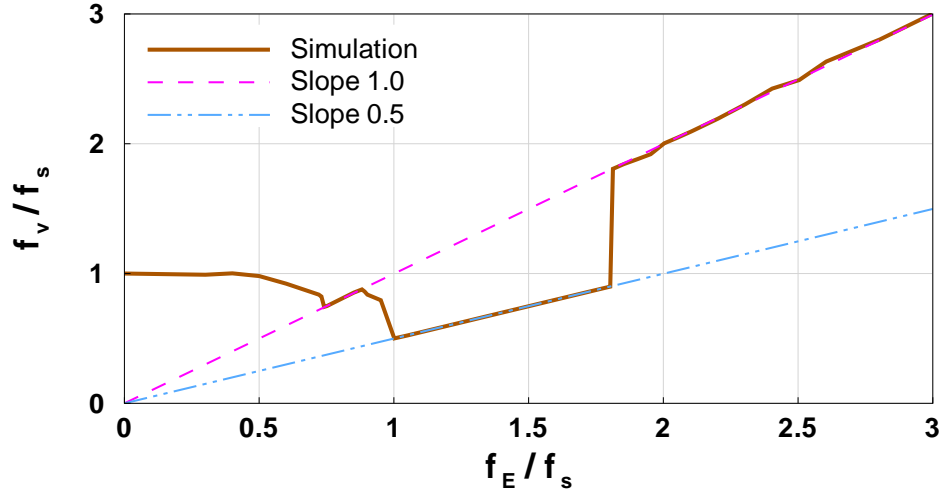


Figure 7.1: Calculated f_v/f_s versus f_E/f_s . Post-synchronization region is indicated by a slope of unity in the simulation results.

pre-synchronization when f_E is below the critical value. This range is in contrast to the range of $f_E/f_s=0.82$ to 1.04 for the case of cross-flow motion at the same amplitude and Re . So, the synchronization range here is not just shifted, but it is also broadened.

Variation of the RMS C_L with f_E is shown in Figure 7.2. The results are presented in terms of relative values; in other words, the RMS C_L is presented relative to its value in the case of $A/D=0$. Similarly, we use the ratio f_E/f_s to express changes in f_E . The lift reduction is clear in this figure; the relative RMS C_L is reduced by two orders of magnitude from 1.696 at $f_E/f_s=1.80$ to 0.0087 (a reduction of 99.5%) at the critical $f_E/f_s=1.81$, corresponding to the beginning of synchronization.

We decompose the steady-state $C_D(t)$ into a constant mean component $\langle C_D \rangle$ and an oscillatory component $C_{D,osc}$ and analyze each one separately. Variation of the relative mean C_D with f_E/f_s is shown in Figure 7.3. Synchronization of the drag causes a reduction in its mean value from 1.32 to 0.77 (a reduction of 42%). In the

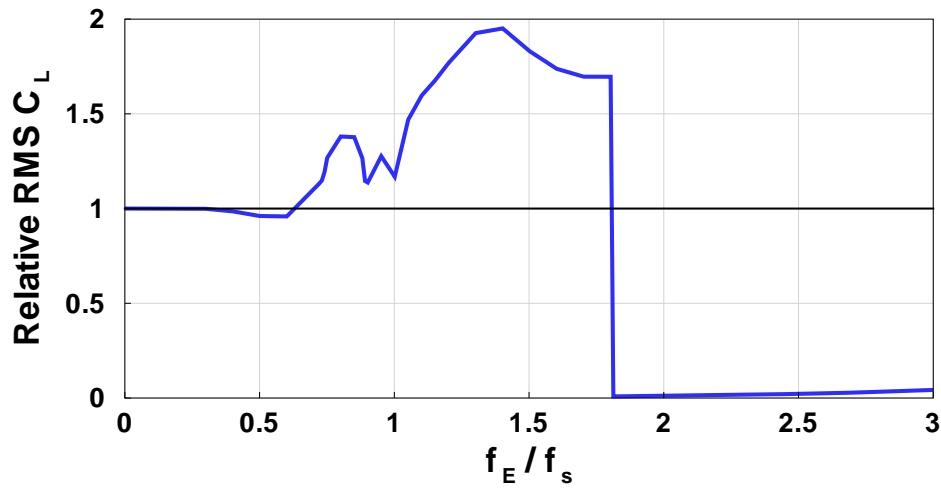


Figure 7.2: Calculated relative RMS C_L versus f_E/f_s .

post-synchronization cases, $\langle C_D \rangle$ is independent of f_E . This is remarkably different from the behavior of $C_{D,osc}$, whose RMS value grows monotonically with f_E as shown in Figure 7.4. This growth can be represented by a quadratic function, as shown in Figure 7.5.

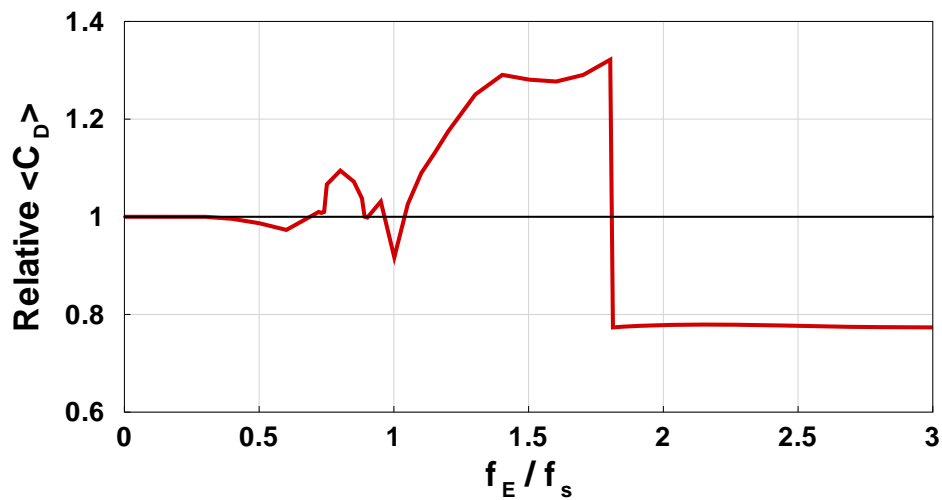


Figure 7.3: Calculated relative $\langle C_D \rangle$ versus f_E/f_s .

The nondimensional mechanical work done by the cylinder on the flow per motion

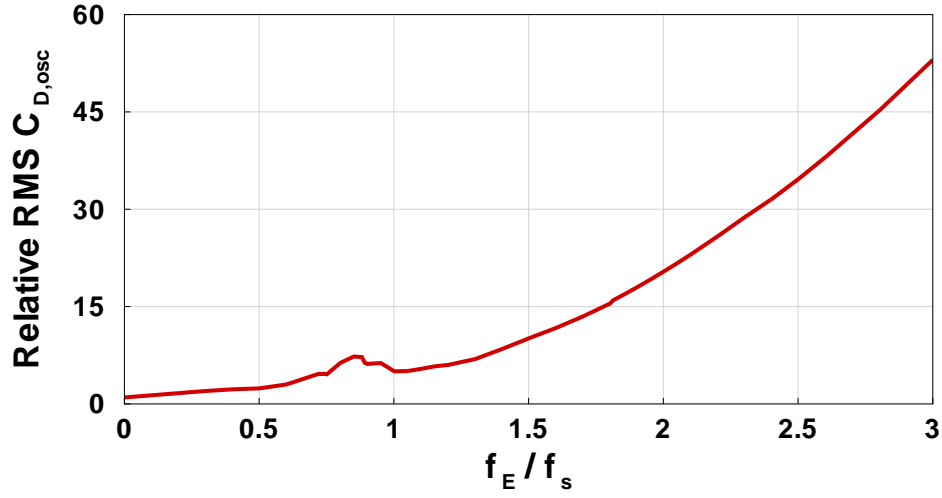


Figure 7.4: Calculated relative RMS $C_{D,osc}$ versus f_E/f_s .

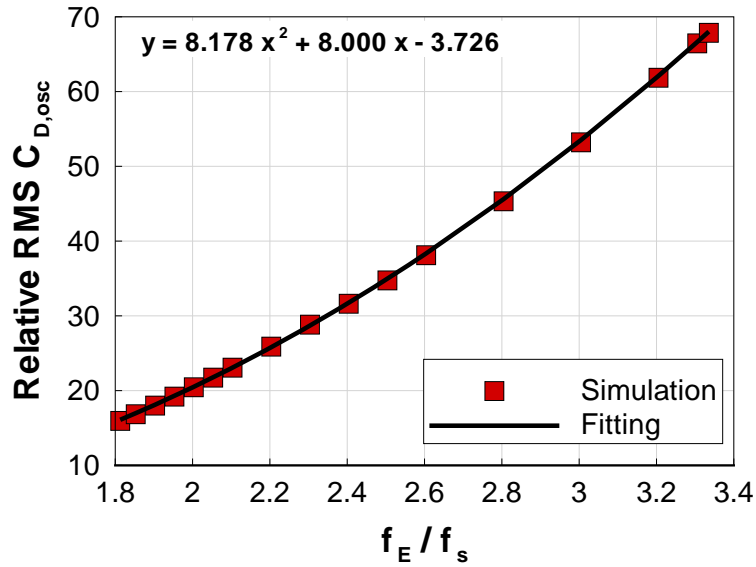


Figure 7.5: Calculated and fitted relative synchronized RMS C_D versus f_E/f_s .

cycle T_M (starting from an arbitrary time t_o) is

$$W_{cyc} = -\frac{A}{D} 2\pi f_E \int_{t_o}^{t_o+T_M} C_D(t) \cos(2\pi f_E t) dt \quad (7.2)$$

The minus sign on the right-hand side of Equation (7.2) ensures the correct sign for W_{cyc} so that, when the cylinder velocity and the drag are in the same direction, W_{cyc} is

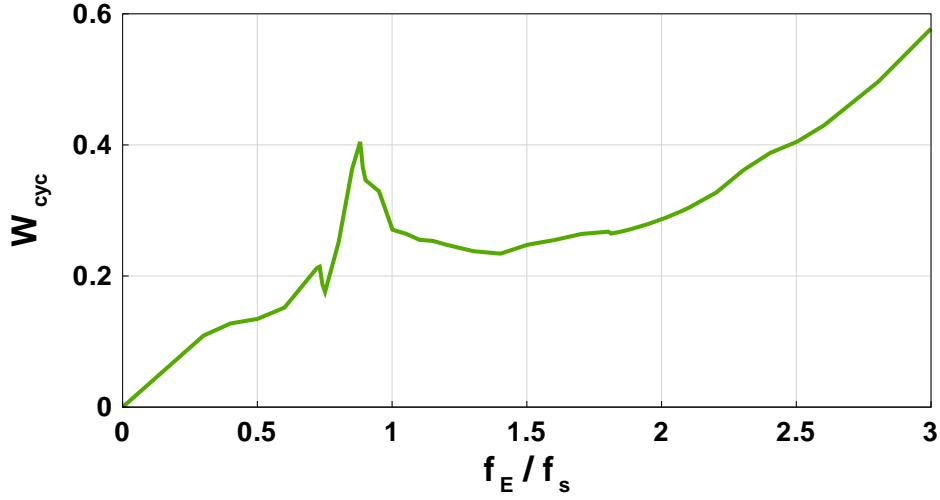


Figure 7.6: Variation of the mechanical work W_{cyc} with f_E/f_s .

negative and work is actually done by the flow on the cylinder. We carry out the above integration numerically using the trapezoidal rule. The results of W_{cyc} as a function of f_E/f_s are given in Figure 7.6. The sign of W_{cyc} is always positive, indicating that work is being done on the flow by the cylinder. This is another difference with the case of cross-flow motion, where W_{cyc} takes on both negative and positive values, depending on f_E .

To first order, the steady-state synchronized drag can be approximated as

$$C_D(t) = \langle C_D \rangle + |C_{D,osc}| \sin(2\pi f_E t + \psi) \quad (7.3)$$

where $|\cdot|$ indicates an amplitude and ψ indicates the phase angle by which C_D leads X . Substituting Equations (7.3) and (7.1) into Equation (7.2) leads to the following expression:

$$W_{cyc} = -\pi \frac{A}{D} |C_{D,osc}| f_E \sin(\psi) \quad (7.4)$$

Equation (7.4) implies that ψ must be negative to yield positive W_{cyc} . We computed ψ for the synchronized drag cases and found that it is always negative varying from

-0.262 (-15°) to -0.175 (-10°), as shown in Figure 7.7. For cross-flow motions,

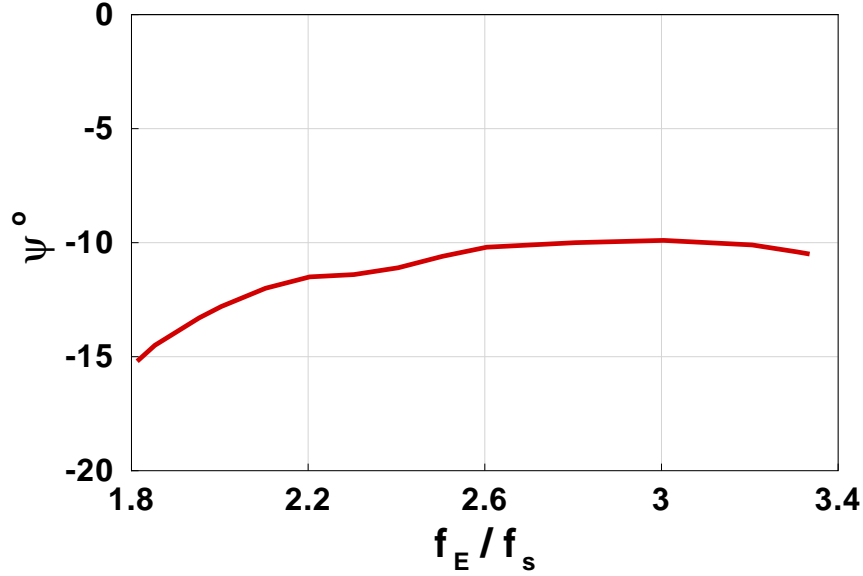


Figure 7.7: Variation of the phase angle ψ of the synchronized C_D with f_E/f_s .

a sudden change in the phase between the synchronized lift and the motion was reported in different studies (e.g., Zdravkovich, 1982; Staubli, 1983; Lu and Dalton, 1996; Marzouk and Nayfeh, 2008c); we also found it to occur for the current Re and motion amplitude. Such a feature does not occur in the examined in-line motion.

We compute the average dissipated power in the flow at each forcing frequency. Its dimensional expression is

$$\hat{P}_{ave} = \frac{1}{\hat{t}_2 - \hat{t}_1} \int_{\hat{t}_1}^{\hat{t}_2} \hat{F}_x [\hat{U}_\infty - \hat{x}] d\hat{t} \quad (7.5)$$

where \hat{F}_x is the dimensional drag force, \hat{t}_1 and \hat{t}_2 are arbitrary (but appropriate for statistical analysis), and $[\hat{U}_\infty - \hat{x}]$ is the relative velocity between the cylinder and free-stream fluid in the \hat{F}_x direction. Combining Equations (7.5) and (7.1) yields the following nondimensional expression for the average dissipated power:

$$P_{ave} = \frac{1}{t_2 - t_1} \int_{t_1}^{t_2} C_D(t) [1 - A/D 2\pi f_E \cos(2\pi f_E t)] dt \quad (7.6)$$

We use at least 40 motion periods to evaluate the integrand in Equation (7.6). When $A/D=0$, P_{ave} reduces to $\langle C_D \rangle$.

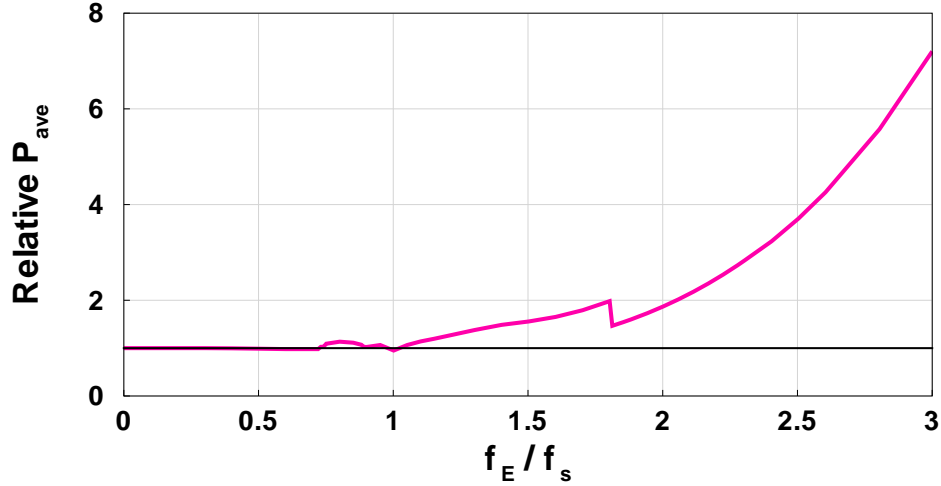


Figure 7.8: Calculated relative P_{avg} versus f_E/f_s .

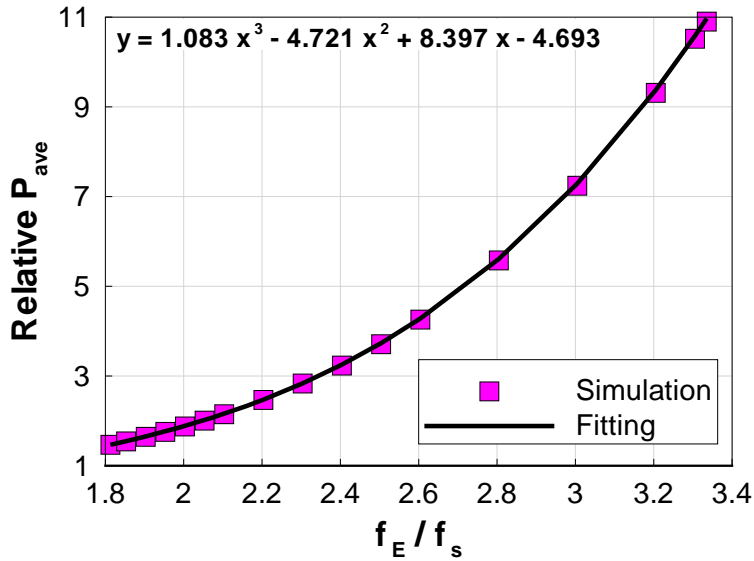


Figure 7.9: Calculated and fitted relative P_{avg} for the synchronized cases versus f_E/f_s .

In Figure 7.8, we show variation of the relative P_{ave} with f_E/f_s . Over the pre-synchronization frequencies, P_{ave} increases slowly, whereas it increases quickly in a

monotonic cubic fashion over the post-synchronization frequencies, as indicated by the polynomial fit in Figure 7.9. This cubic profile can be explained as follows. The first term in the integrand in Equation (7.6) gives $\langle C_D \rangle$, which remains unchanged with f_E for post-synchronization cases, as shown in Figure 7.3. Therefore, P_{ave} is controlled by the second term in the integrand, in which $C_D(t)$ is multiplied by f_E . Due to the approximation in Equation (7.3), we find that this term becomes $-\sqrt{2} \pi \sin(\psi) (A/D) f_E \text{ RMS } C_{D,osc}$, which is proportional to the product of $\text{RMS } C_{D,osc}$ and f_E . The angle ψ varies weakly with f_E , as in Figure 7.7, and $\text{RMS } C_{D,osc}$ increases quadratically with f_E as shown in Figure 7.5; hence P_{ave} increases cubically with f_E .

7.4 Synchronization Map

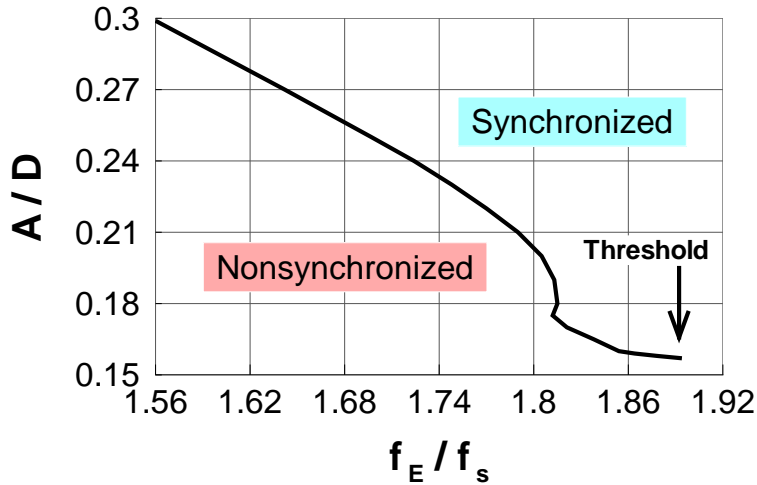


Figure 7.10: Locus of the critical f_E in the $(A/D) - (f_E/f_s)$ plane.

We found that increasing the motion amplitude decreases the critical frequency at which the lift reduction starts. There is a threshold of this amplitude below which

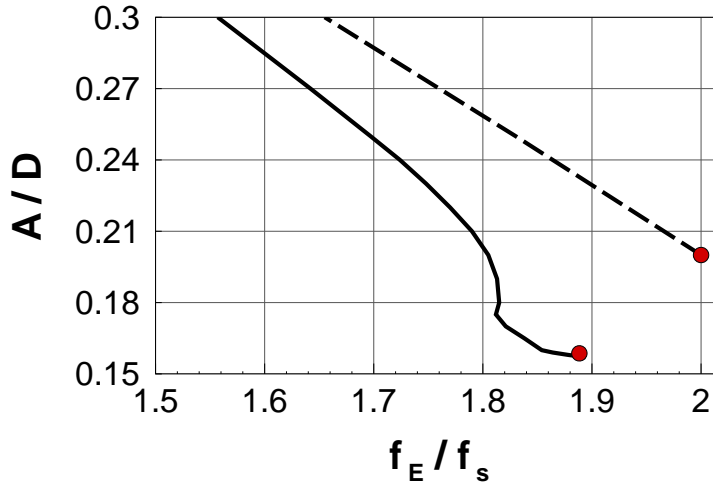


Figure 7.11: Loci of the critical f_E in the $(A/D) - (f_E/f_s)$ plane at $Re=500$ (solid line) and $Re=300$ (dashed line). The threshold (A/D) is indicated by a solid circle.

the lift does not exhibit this feature for any forcing frequency. We found that the threshold here is $(A/D)=0.157$. Figure 7.10 shows the locus of the critical frequency in the $(A/D) - (f_E/f_s)$ plane. Similar variations of the lift and drag with f_E take place at other Reynolds numbers. The loci of the critical frequencies at $Re=500$ and 300 are compared in Figure 7.11. The locus when $Re=300$ is nearly a straight line with a negative slope, and the threshold A/D is increased to 0.2 . The need for a larger motion for the lift reduction to develop at lower Re can be explained by the higher viscous dissipation. This explains the absence of such a feature at $Re=80$ in the experiments of Tanida et al. (1973) and our simulations.

7.5 Pre- and Post-Synchronization Modes

Next, we present several lift and drag response modes that occur before and after the onset of synchronization. These modes are quantitatively and qualitatively different.

Before the critical frequency, we found lift and drag responses that are either period- n , quasiperiodic, or chaotic motions. The best method to distinguish among these responses is Poincaré sections. In Figure 7.12, we show the Poincaré sections of C_L for representative nonsynchronized cases: i) quasiperiodic response at $f_E/f_s=0.4$, ii) period-6 response at $f_E/f_s=0.72$, iii) chaotic response at $f_E/f_s=0.73$, and iv) period-2 response at $f_E/f_s=1.7$. The corresponding Poincaré sections of C_D are shown in Figure 7.13, which clearly indicate that both of the lift and drag have the same response type.

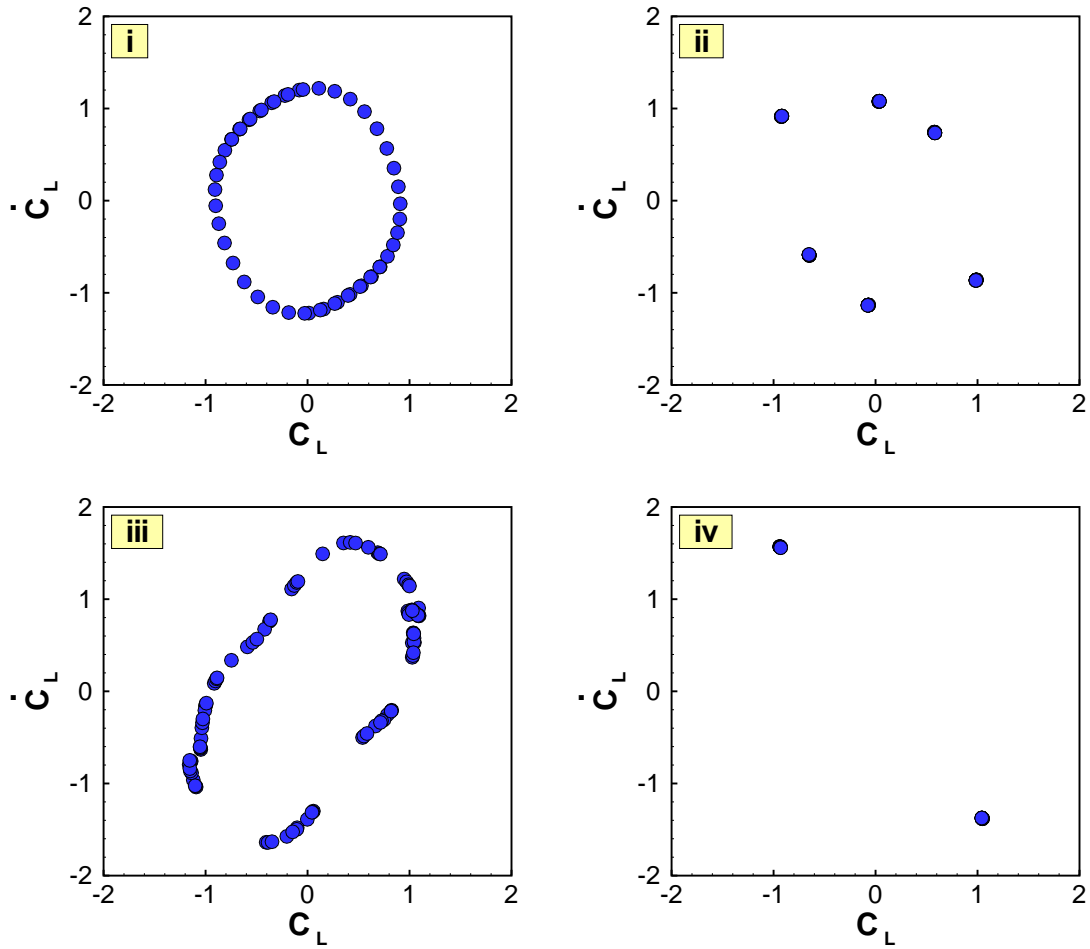


Figure 7.12: Poincaré sections of nonsynchronized C_L : i) $f_E/f_s=0.4$, ii) $f_E/f_s=0.72$, iii) $f_E/f_s=0.73$, and iv) $f_E/f_s=1.7$.

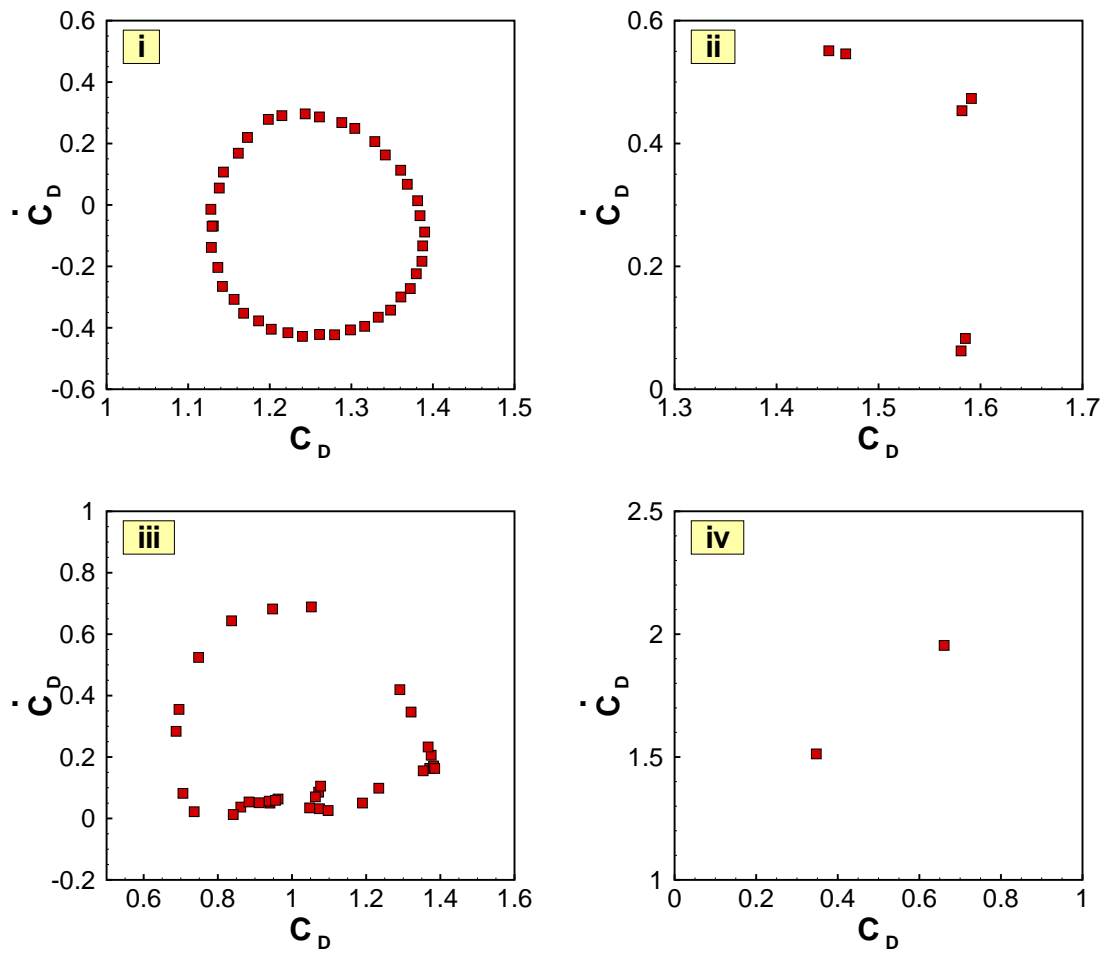


Figure 7.13: Poincaré sections of nonsynchronized C_D : i) $f_E/f_s=0.4$, ii) $f_E/f_s=0.72$, iii) $f_E/f_s=0.73$, and iv) $f_E/f_s=1.7$.

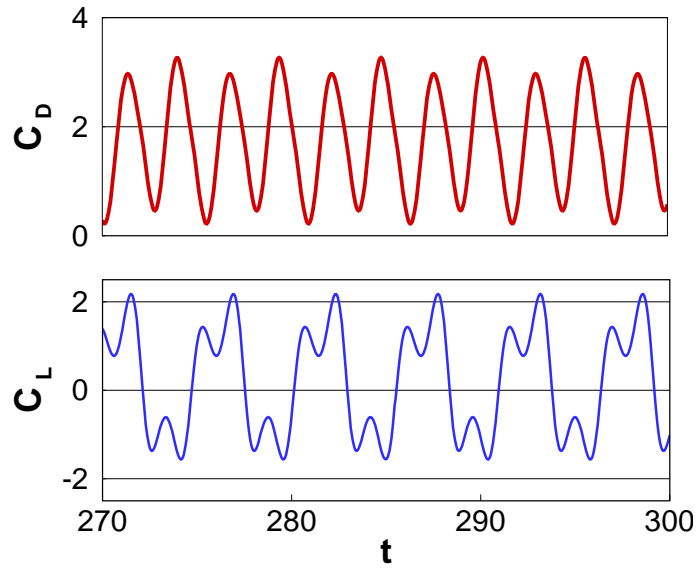


Figure 7.14: Steady-state C_L and C_D versus time for $f_E/f_s=1.7$.

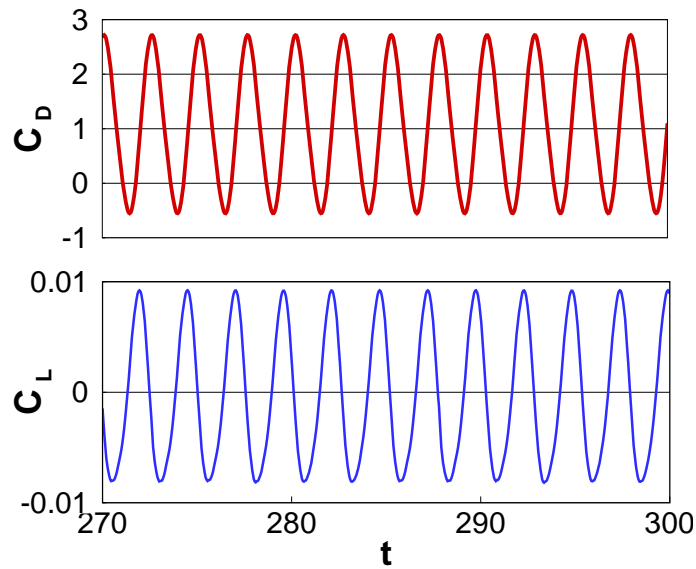


Figure 7.15: Steady-state C_L and C_D versus time for $f_E/f_s=1.81$.

The period-2 mode of the lift and drag takes place for a wide range of f_E/f_s (from 1.15 to 1.8). It is followed by synchronization, which is accompanied by large changes in C_L and C_D as one can see from comparison of the amplitudes and patterns of the time histories in Figure 7.14 to those for the synchronized case at $f_E/f_s=1.81$ in

Figure 7.15.

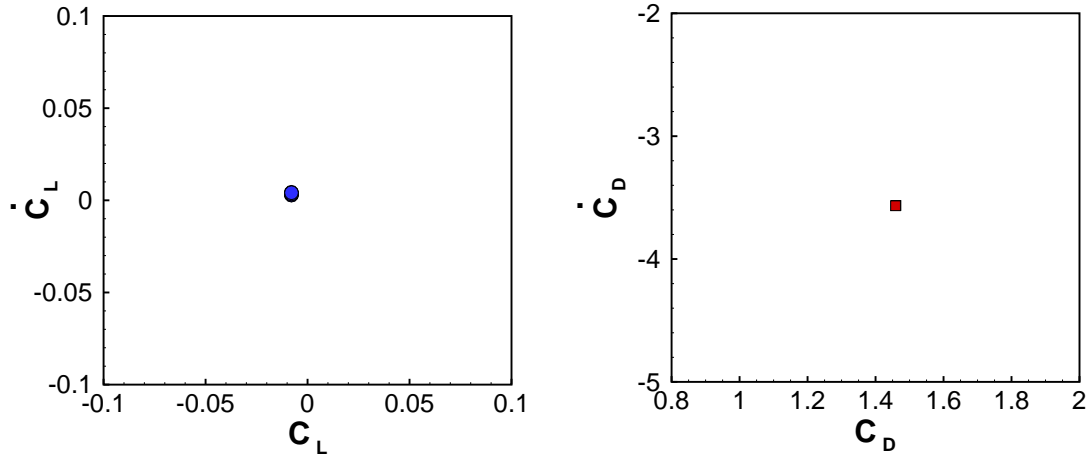


Figure 7.16: Poincaré sections of C_L and C_D for $f_E/f_s=1.81$.

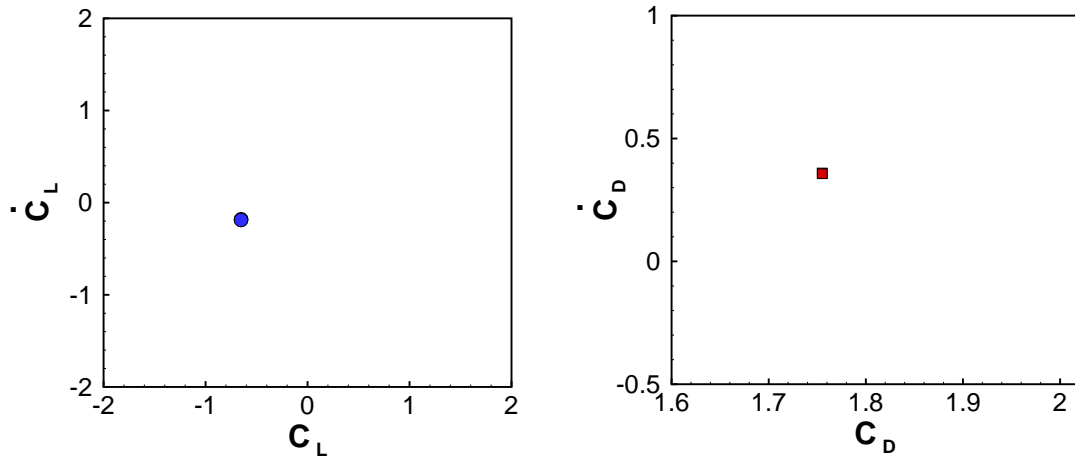


Figure 7.17: Poincaré sections of C_L and C_D for cross-flow motion at $f_E/f_s=1$.

The synchronized lift and drag are characterized by a single point in the Poincaré sections in Figure 7.16. We pay attention to the changes that occur in the lift and drag and their coupling due to synchronization. To achieve this, we compare their spectra and cross-bicoherence to those we found for the period-2 case at $f_E/f_s=1.7$

(the Poincaré sections of C_L and C_D for this case were shown already in the last plots of Figures 7.12 and 7.13, respectively) and also to those we found for another synchronized case at $f_E/f_s=1$ for a cross-flow motion. The Poincaré sections of C_L and C_D for the latter case are shown in Figure 7.17. Whereas each of these sections contains a single point, as was the case in the synchronized cases due to the in-line motion, we show below that the synchronized C_L is period-1 for both cases and C_D is period-1 in case of in-line motion but period-1/2 in case of cross-flow motion. Because one cannot distinguish between the two cases using the Poincaré sections for C_D , we use second- and third-order spectral analysis to differentiate between them.

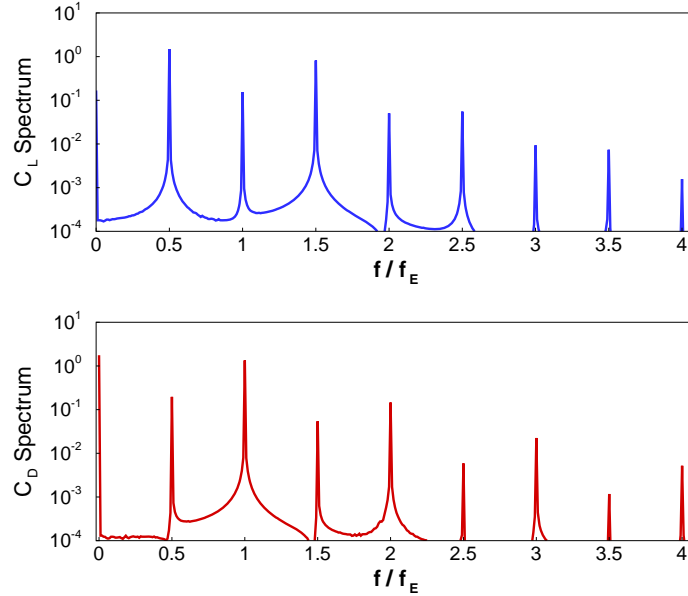


Figure 7.18: Spectra of C_L and C_D at $f_E/f_s=1.7$.

The spectra of C_L and C_D for the period-2 case at $f_E/f_s=1.7$ are shown in Figure 7.18. The frequency f is scaled with f_E to better indicate the positions of the fundamental components and their superharmonics and subharmonics. The fundamental component of C_L is at $f_E/2$, whereas the fundamental component of C_D is at f_E . There are

odd and even superharmonics of C_L , but the odd harmonics are stronger. There are fractional superharmonics in the spectrum of C_D , but the integer ones are stronger. The spectra of C_L and C_D for the synchronized case at $f_E/f_s=1.81$ are shown in Figure 7.19. The fundamental component of C_L is now at f_E and the fundamental component of C_D is still at f_E . Whereas there are still even and odd superharmonics in the spectrum of C_L (as in the pre-synchronization case), their amplitudes decay monotonically and there is no bias towards the odd superharmonics. The fractional superharmonics in the spectrum of C_D have disappeared.

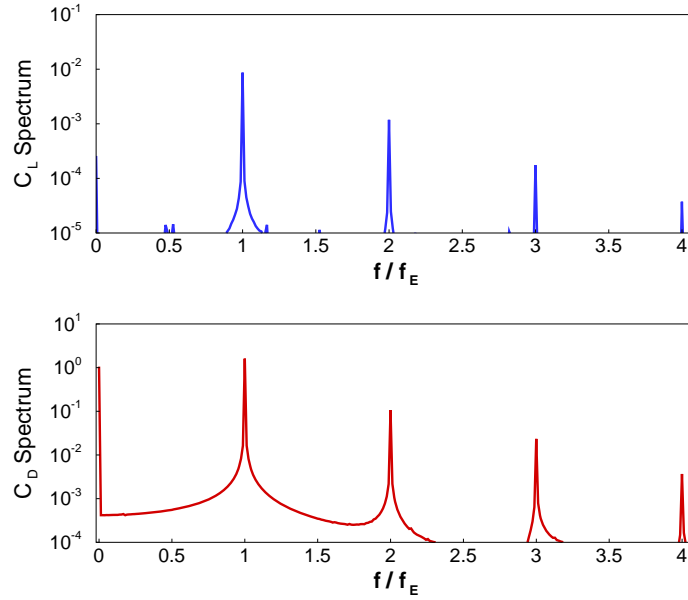


Figure 7.19: Spectra of C_L and C_D at $f_E/f_s=1.81$.

The spectra of C_L and C_D for the synchronized case at $f_E/f_s=1$ for cross-flow motion are shown in Figure 7.20. One of the main differences between this mode of synchronization and the one due to in-line motion is that C_D is synchronized at $2f_E$ in the case of cross-flow motion rather than at f_E . Also, the spectrum of C_L consists mainly of odd harmonics, and the spectrum of C_D consists mainly of even ones. It

should be mentioned here that, in the no-motion case, the spectra of C_L and C_D are qualitatively very similar to those in Figure 7.20 (after scaling f with f_s instead of f_E).

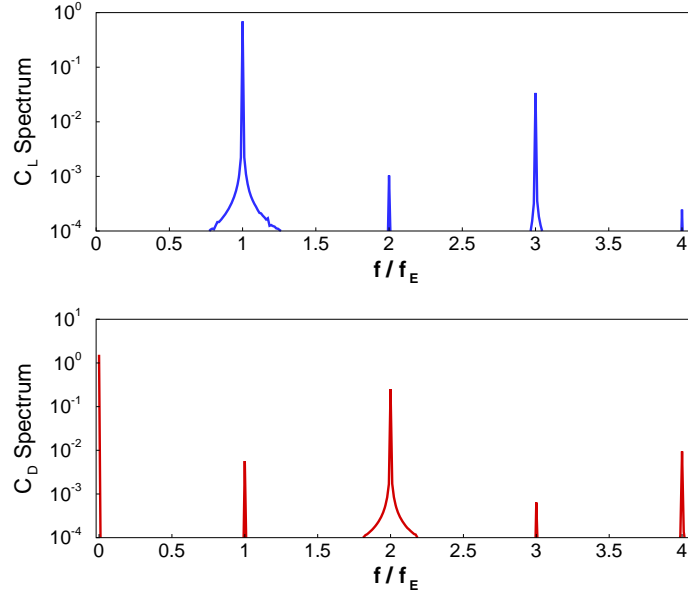


Figure 7.20: Spectra of C_D and C_L for cross-flow motion at $f_E/f_s=1$.

If we define a total force coefficient C_T as $\sqrt{C_L^2 + C_D^2}$ and its angular orientation β_T as $\arctan(C_L/C_D)$, measured in the counterclockwise direction from the positive x -axis, then the near-harmonic profiles of both C_T and β_T in the case of synchronization due to cross-flow motion (as shown in Figure 7.21 for $f_E/f_s=1$) or in the no-motion case are totally altered in the case of synchronization due to in-line motion (as shown in Figure 7.22 $f_E/f_s=1.81$). In the former cases, the frequency of C_T is equal to $2 f_E$ (or $2 f_s$), which is twice the frequency of β_T . Also, the angle β_T is limited to the first and fourth quadrants, thus C_D is always positive. With in-line synchronization, the profile of β_T becomes nearly a step function equal to either 0° or $\pm 180^\circ$. This effect is a consequence of the extreme reduction in C_L . The interval when $|\beta_T| \approx 180^\circ$

corresponds to negative C_D .

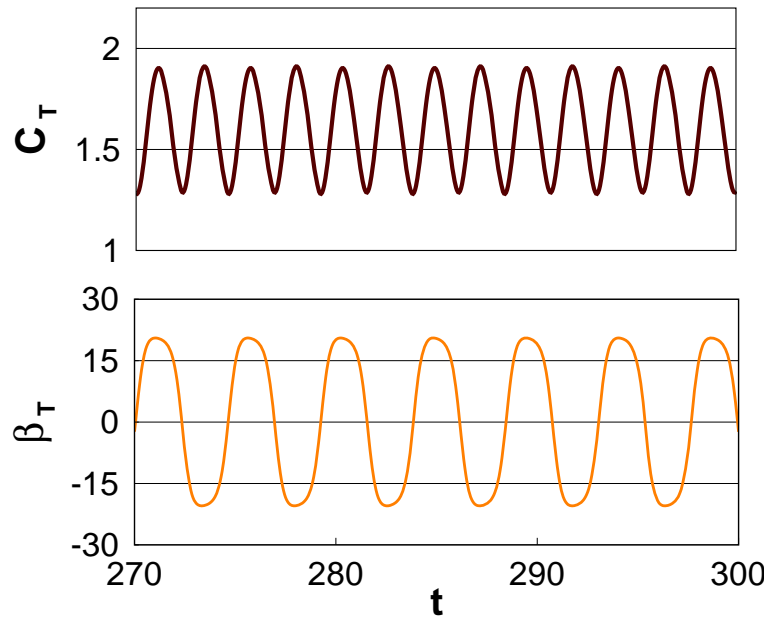


Figure 7.21: Steady-state C_T and β_T for cross-flow motion at $f_E/f_s=1$.

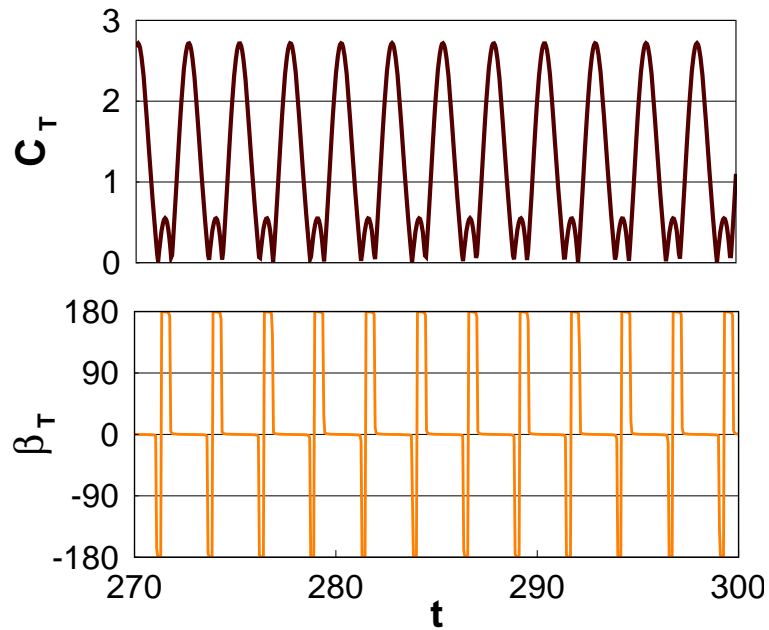


Figure 7.22: Steady-state C_T and β_T versus time for $f_E/f_s=1.81$.

7.6 Higher-Order Spectral Analysis

To examine the type of quadratic coupling between C_L and C_D , we calculate the magnitude-squared cross-bicoherence $b_{LLD}^2(f_1, f_2)$ as

$$b_{LLD}^2(f_1, f_2) = \frac{|M_{LLD}(f_1, f_2)|^2}{M_{LL}(f_1) M_{LL}(f_2) M_{DD}(f_1 + f_2)} \quad (7.7)$$

where

$$M_{LLD}(f_1, f_2) = E \left[\tilde{L}^*(f_1) \tilde{L}^*(f_2) \tilde{D}(f_1 + f_2) \right] \quad (7.8)$$

is the cross-bispectrum, $\tilde{L}(f)$ and $\tilde{D}(f)$ are the discrete Fourier transforms of $C_L(t)$ and $C_D(t)$, respectively; E indicates the expected value (or time average); and the superscript $*$ indicates the complex conjugate. The auto-power spectra $M_{LL}(f)$ and $M_{DD}(f)$ of C_L and C_D are given by

$$M_{LL}(f) = E \left[\tilde{L}^*(f) \tilde{L}(f) \right] \quad (7.9)$$

$$M_{DD}(f) = E \left[\tilde{D}^*(f) \tilde{D}(f) \right] \quad (7.10)$$

The corresponding magnitude-squared cross-bicoherence for the C_L and C_D spectra in Figure 7.18 is shown in Figure 7.23. The presence of many quadratically interacting lift components is noticeable. A fractional subharmonic or superharmonic in C_D at $\frac{1}{2} m f_E$ is formed by quadratic coupling between the C_L components at $(m + k) f_E$ and $-(k + \frac{1}{2} m) f_E$, where $k \geq 0$ is an integer. These coherence points are located in the difference region of b_{LLD}^2 . They are in addition to other couplings between the C_L components at $(\frac{1}{2} m - k) f_E$ and $k f_E$, where $k > 0$ is an integer. These coherence points are located in the sum region of b_{LLD}^2 .

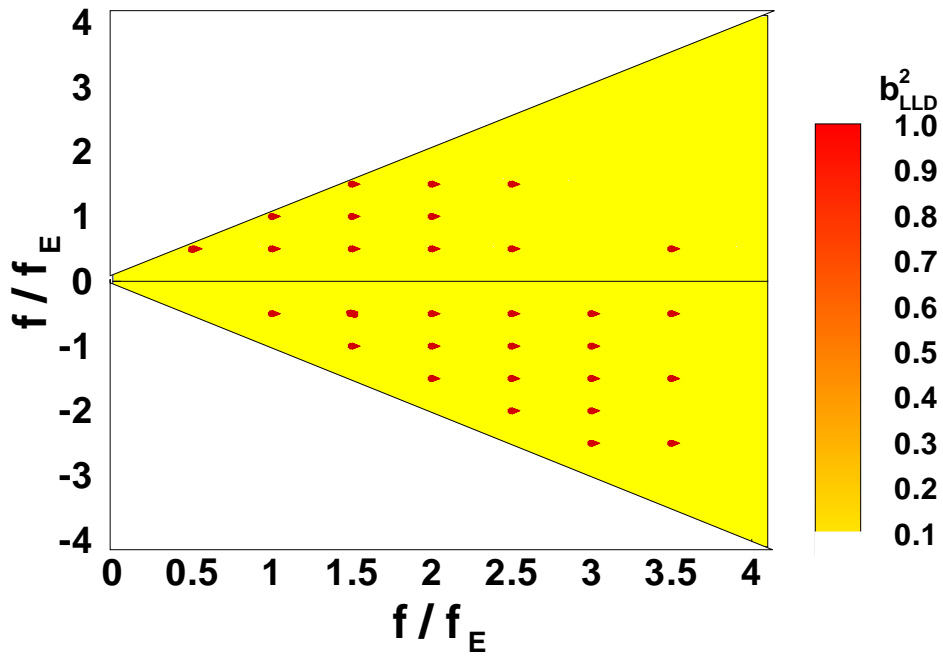


Figure 7.23: Magnitude-squared cross-bicoherence for $f_E/f_s=1.7$.

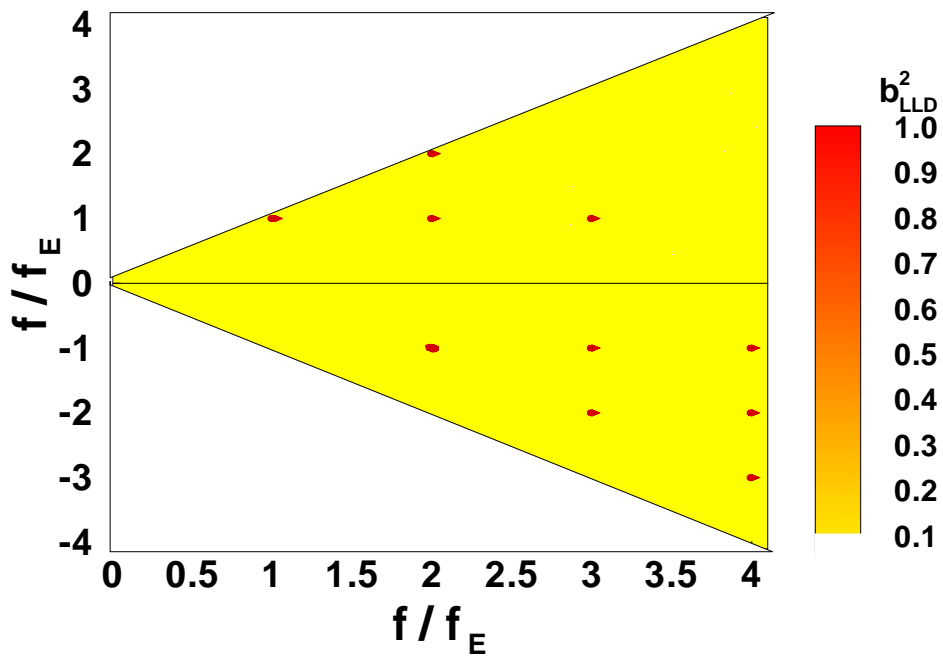


Figure 7.24: Magnitude-squared cross-bicoherence for $f_E/f_s=1.81$.

The number of coherence points is reduced in the synchronized cases, as shown in Figure 7.24, which corresponds to the spectra of C_L and C_D in Figure 7.19. This is because there are phase-coherent components at fractions of f_E . The fundamental frequency of C_D at f_E is formed by the interaction of the components of C_L at $k f_E$ and $-(k + 1) f_E$, where $k \geq 0$ is an integer. Similarly, the superharmonic in the spectrum of C_D at $2f_E$ is formed by the interaction of the components of C_L at $k f_E$ and $-(k + 2) f_E$ in addition to self-interacting C_L component at f_E . A similar structure occurs for the higher superharmonics in C_D .

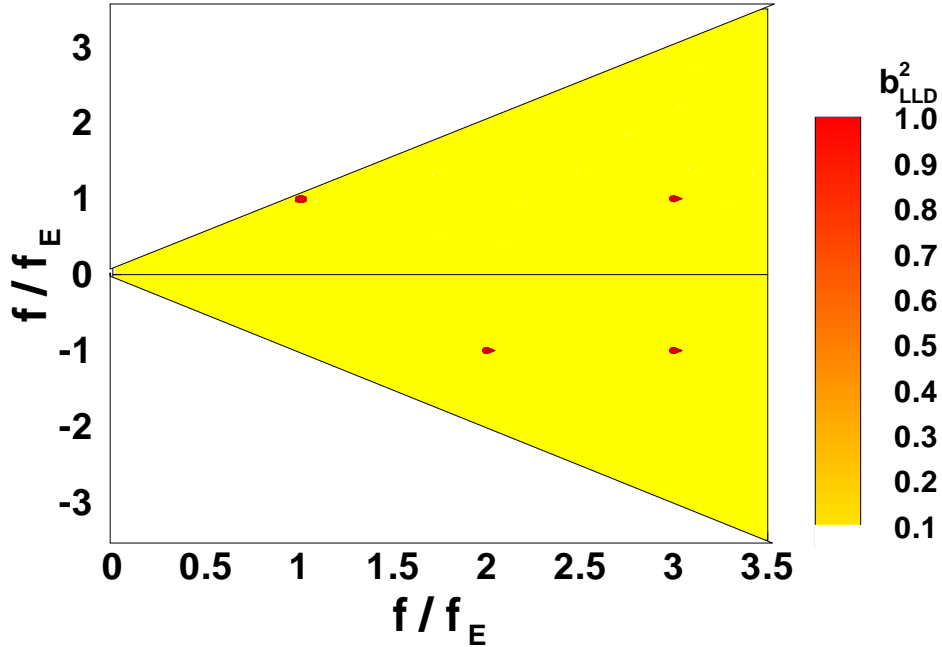


Figure 7.25: Magnitude-squared cross-bicoherence b_{LLD}^2 for cross-flow motion at $f_E/f_s=1$.

The bicoherence plot is even simplified further for synchronization cases due to cross-flow motion, as shown in Figure 7.25, which corresponds to the C_L and C_D spectra in Figure 7.20. This is because of the presence of half the number of significant superharmonics in the C_L (odd ones) and C_D (even ones) spectra. The fundamental

component of C_D at $2f_E$ is formed by self-interacting C_L component at f_E in addition to the interaction of the components of the C_L at $3f_E$ and $-f_E$. The small C_D subharmonic at f_E is formed by the interaction of the components of C_L at $2f_E$ and $-f_E$.

The bicoherence analysis provides information about the quadratic coupling of the C_L components in the C_D components. To examine the linear correlation between the C_L and C_D components, we use the (linear) cross-power spectrum $M_{LD}(f)$, defined as

$$M_{LD}(f) = E \left[\tilde{L}^*(f) \tilde{D}(f) \right] \quad (7.11)$$

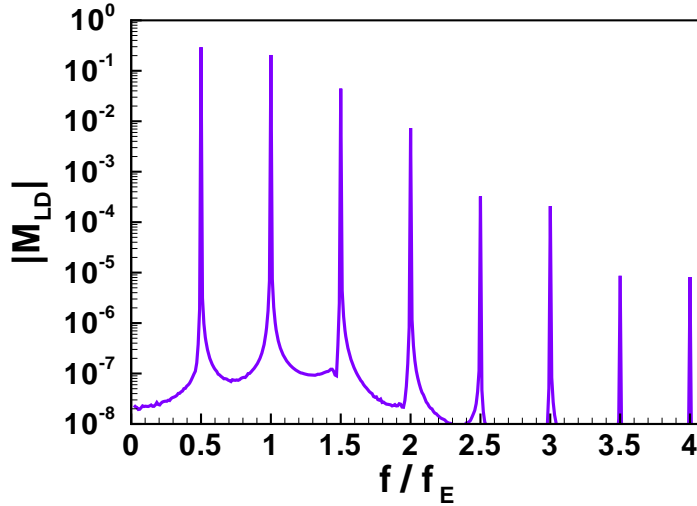


Figure 7.26: Absolute of cross-power spectrum $|M_{LD}|$ for $f_E/f_s=1.7$.

Figures 7.26-7.28 show the absolute value of the cross-power spectrum $|M_{LD}(f)|$ corresponding to the C_L and C_D spectra in Figures 7.18-7.20, respectively. For the pre-synchronization case, $|M_{LD}(f)|$ in Figure 7.26 indicates that all C_L components are linearly coupled with the respective C_D components. The couplings at $f_E/2$ and f_E are both one order of magnitude larger than the one at the subsequent superhar-

monic at $3f_E/2$. For the synchronized cases with either in-line or cross-flow motions, linear couplings occur at f_E and its integer superharmonics. The decay of $|M_{LD}(f)|$ at higher superharmonics is faster in the case of in-line motion.

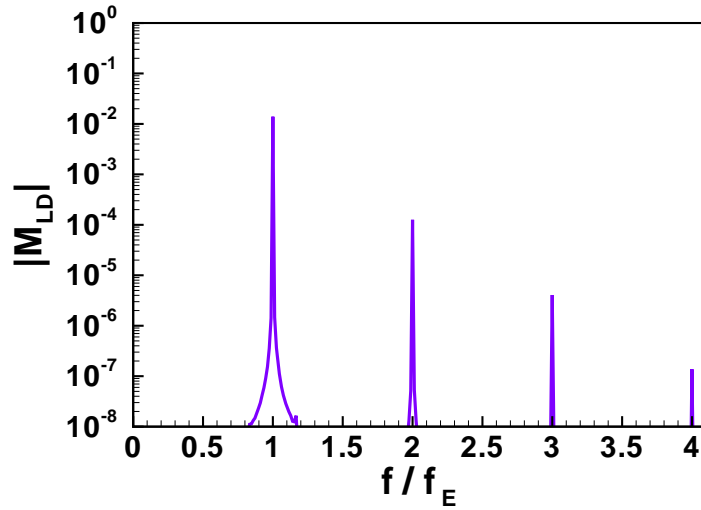


Figure 7.27: Absolute of cross-power spectrum $|M_{LD}|$ for $f_E/f_s=1.81$.

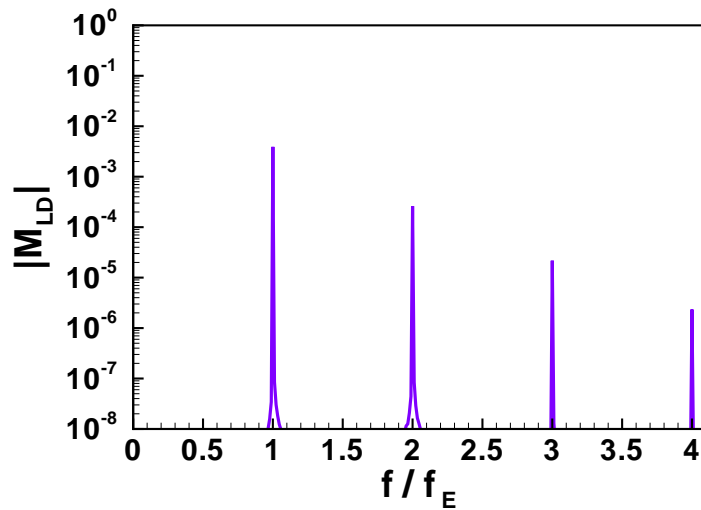


Figure 7.28: Absolute of cross-power spectrum $|M_{LD}|$ for cross-flow motion at $f_E/f_s=1$.

7.7 Wake Structure and Surface Pressure

In the remaining part of this chapter, we relate the large differences in the post-synchronization cases, including the lift reduction and the saturation of the mean drag, to changes in the vortex shedding and the pressure distribution on the surface of the cylinder.

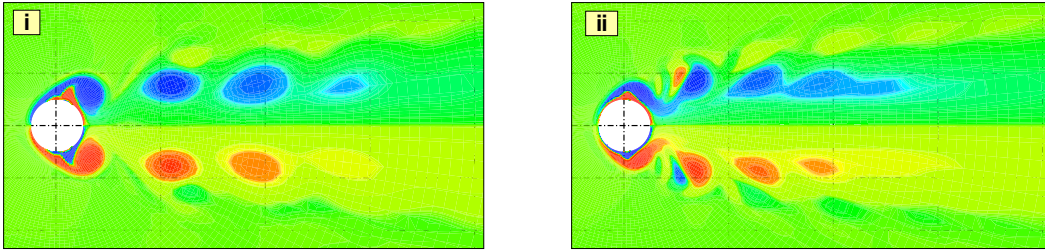


Figure 7.29: Vorticity contours when $X=0$ for synchronized cases: i) $f_E/f_s=1.81$ and ii) $f_E/f_s=3$. Positive (counterclockwise) vortex is being shed from the bottom surface.

In Figure 7.29, vorticity contours in the near field for two post-synchronization cases (at $f_E/f_s=1.81$ and 3) are shown at the instant when $X(t)=0$ and increasing (from negative to positive), and therefore \dot{X} is maximum. The typical von Kármán vortex street with 2S mode is replaced by two parallel 1S streets: one with positive vortices located behind the bottom point of the surface and the other with negative vortices located behind its top point. This instantaneous symmetry in the wake is what causes the reduction in C_L because the lift force is a result of the instantaneous imbalance in the surface pressure (which is related to the vortex strength at the surface) between the top and bottom parts of the surface. As f_E increases, the vortex shedding frequency also increases and the shed vortices along each street become

closer and those being shed from the surface become stronger (higher vorticity levels). So, we expect more negative pressure at the locations of these vortices on the surface of the cylinder.

Figure 7.30 shows distributions of the mean pressure coefficient $\langle C_P \rangle$ at the surface for the same two post-synchronization cases shown in Figure 7.29. The distributions in this figure are almost symmetric about the base point (where the angular coordinate θ is 180°), which causes the mean C_L to be zero. Whereas this figure cannot reveal much about the large reduction in the RMS C_L due to synchronization, we use it to interpret the reduction and saturation behavior of the mean C_D due to synchronization. The value of $\langle C_D \rangle$ is mainly due to the imbalance in $\langle C_P \rangle$ between the upstream and downstream parts of the surface. The upstream $\langle C_P \rangle$ is close to unity, whereas the downstream $\langle C_P \rangle$ is negative. We recall that the part of the surface near the base point ($\theta=180^\circ$) is nearly isolated from shed vortices in the post-synchronization cases, as shown in Figure 7.29. This is reflected in the ‘bump’ in the downstream $\langle C_P \rangle$ at $f_E/f_s=1.81$; it explains the 42% reduction in $\langle C_D \rangle$ once synchronization occurs.

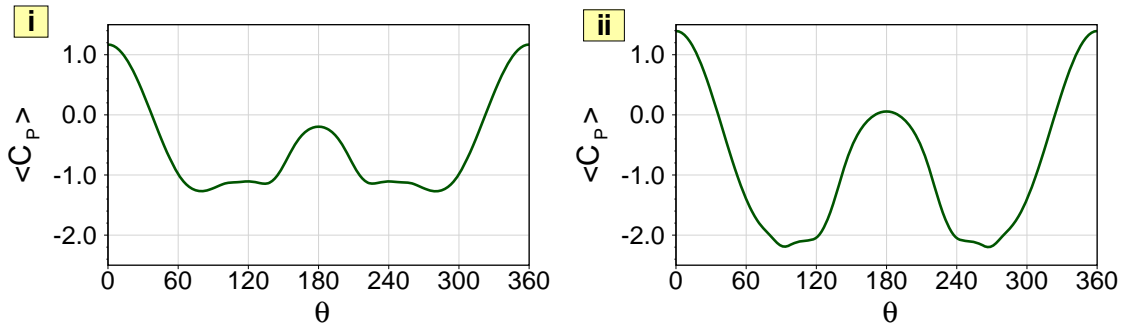


Figure 7.30: Surface distribution of $\langle C_P \rangle$ for synchronized cases: i) $f_E/f_s=1.81$ and ii) $f_E/f_s=3$. The angle θ is 0 at the stagnation point and 90° at the top point.

To interpret the saturation behavior, we compare the two surface distributions of $\langle C_P \rangle$

at $f_E/f_s=1.81$ and 3. The downstream bump becomes stronger in the latter case, which results in a reduced $\langle C_D \rangle$ for this high-frequency synchronized case. However, this is counteracted to a large extent by a reduction (more negative) in $\langle C_P \rangle$ over $\theta = 30^\circ-90^\circ$ and $270^\circ-360^\circ$. Therefore, variations in $\langle C_D \rangle$ for the post-synchronization cases are minimal.

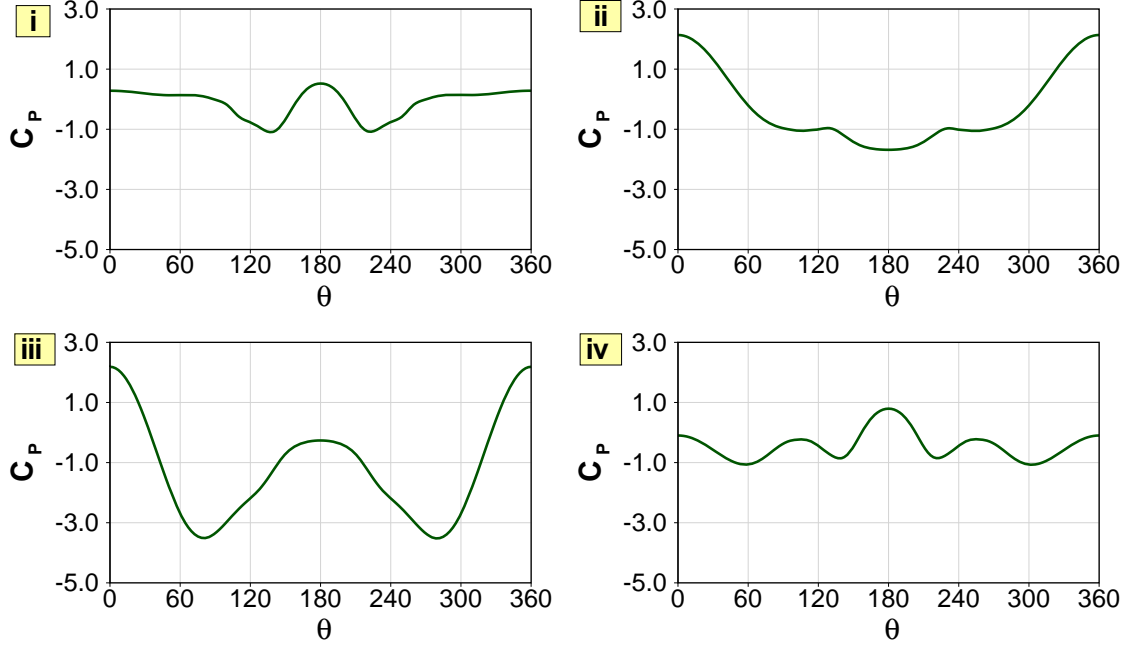


Figure 7.31: Surface distribution of C_P over one motion cycle for $f_E/f_s=1.81$. The motion sequence is: i) $X=0$ and \dot{X} is maximum, ii) X is maximum and $\dot{X}=0$, iii) $X=0$ and \dot{X} is minimum, and iv) X is minimum and $\dot{X}=0$.

To support and augment the above discussion on C_L , C_D , and surface $\langle C_P \rangle$, we examine the surface distributions of C_P over one motion cycle for the post-synchronization case at $f_E/f_s=1.81$ in Figure 7.31. The surface C_P is shown at four equally-spaced instants of time. The surface C_P exhibits instantaneous symmetry about the x -axis. This is due to the instantaneous symmetry of the magnitude of the vorticity at the surface. Because the peaks and valleys in $C_L(t)$ are mainly due to the difference

between C_P at the top and bottom parts of the surface, these peaks and valleys are reduced in the post-synchronization cases due to the strong reduction in the C_P difference that contributes to $|C_L|$. These C_P snapshots also explain the increase in RMS $C_{D,osc}$ with f_E for the post-synchronization cases even though $\langle C_D \rangle$ remains unchanged. Because the surface distribution of $\langle C_P \rangle$ becomes more distorted as f_E increases (as in Figure 7.30), the distortion in the instantaneous C_P distributions is strengthened also. The RMS $C_{D,osc}$ depends on the instantaneous C_P imbalance between the upstream and downstream parts of the surface. This imbalance increases steadily with f_E as a result of the intensified vorticity at the surface.

Chapter 8

Summary and Conclusions

This dissertation research is another step toward increasing the understanding of the wake of a circular cylinder. To accomplish this, we used analytical and numerical approaches to examine the performance of existing wake models and then proposed improved wake models. We applied different analysis techniques to characterize the types of wakes excited by the cylinder motion. We showed the limitations of each technique in terms of its ability to distinguish among the complex wake responses. We studied changes in the wake and induced fluid force due to cross-flow motion with frequency sweeps, and provided interpretations for some reported results of interest in the literature based on the behavior of the nonlinear systems. We showed that relevant experimental studies with sine dwell need to be checked carefully to ensure that the results correspond to stationary forcing and not to quasistationary forcing. We studied in detail the effects of in-line motion on the wake from several perspectives, including the magnitude and response type of the lift and drag, their linear and quadratic couplings, the mechanical work done on the flow, the wake structure, and the surface pressure distributions. In the following, we provide a list of the main conclusions we have from our study:

- We modeled the lift and drag coefficients on a fixed cylinder in a uniform flow through a free-wake oscillator for the lift coefficient and a quadratic algebraic function for the drag coefficient. The models account for the coupling between these coefficients. For the lift coefficient, the van der Pol oscillator was modified by adding a Duffing-type cubic term. Then, the values of the model parameters were estimated by matching an approximate solution of the model, obtained by the method of harmonic balance, to the results we obtained from CFD (computational fluid dynamics) simulations. As for the oscillating drag coefficient, we modified the single-term quadratic model by introducing a second quadratic term so that the exact phase between the drag and lift can be reproduced. We examined the models performance for two different values of the Reynolds number and found they reproduce the lift and drag coefficients obtained from time-consuming CFD calculations. By building a database for the model parameters over a finite numbers of Reynolds numbers, one can use these models to evaluate the force coefficients at any arbitrary Reynolds number within the database (interpolation might be needed) and hence avoid the CFD calculations. The time required to find longtime histories of these coefficients using CFD simulations is about three orders of magnitude larger than the time needed to solve the proposed models, although the accuracy is almost the same. Moreover, these models provide valuable information about characteristics of these coefficients and the system dynamics, such as the order of the nonlinearity, which cannot be revealed from CFD simulations.
- We extended our improved free oscillator for the lift coefficient by accounting for harmonic motion of the cylinder in the cross-flow direction. The objective was to choose an appropriate forcing term that represents the coupling with

cylinder motion. We examined the influences of existing forcing forms, a single external-forcing term, and found that this simple forcing fails to capture the wake bistability, which is a key feature in the wake of a moving cylinder. We also found that parametric forcing is not satisfactory. Consequently, we introduced mixed forcing (external plus parametric) to capture the bistability and hysteresis. We found that velocity-based and acceleration-based forcing produce similar responses. The proposed models have three parameters: two amplitudes for the two parts of the forcing and a third for their phase angle. The phase should be negative for softening-type frequency-response curves.

- We used the CFD simulations and studied the effect of the frequency of a cross-flow motion on the flow in terms of the magnification of the lift and drag forces within and outside the synchronization band of forcing frequencies. Within this band, shedding is entrained by the cylinder motion and the flow response (i.e., the lift coefficient) is synchronized with the motion frequency and hence it is referred to as period-1 response. Outside this synchronization region, the response is complex, making it challenging to identify its type. Using modern methods of nonlinear dynamics, such as power spectra, phase portraits, and one-sided Poincaré sections, we identified three types of responses: period- n with $n > 1$, two-period quasiperiodic (or ‘two torus’), and chaotic responses. We used the Poincaré sections and found that we have a quasiperiodic route to chaos with torus-breakdown scenario.
- We used the CFD simulations and studied the flow past a cylinder oscillating in the cross-flow direction, under synchronization condition, with four types frequency sweep: stationary, quasistationary, discrete, and nonstationary. We

identified several nonlinear phenomena, such as *hysteresis*, *bistability*, *overshoot*, and *passage through resonance*. The first one was investigated in terms of the effect of the rate of the frequency sweep and the last two require nonstationary forcing to develop. We identified a small (or type-A) attractor and a large (or type-B) attractor. The coexistence of two stable solutions, or the *bistability*, causes a *hysteresis* region. The jump between the attractors depends on whether the frequency is increased or decreased. Within the *hysteresis* region, the initial conditions determine the attractor.

- We used the CFD simulations and studied the problem of a cylinder undergoing harmonic in-line motion in a uniform stream for different motion (or wake excitation) frequencies f_E . Depending on the Reynolds number and the nondimensional amplitude of motion A/D , synchronization can occur. When nonsynchronized, the lift and drag can be periodic with large periods, quasi-periodic, or chaotic. The synchronization occurs at lower values of the forcing frequency f_E when either A/D or the Reynolds number increases. When synchronization occurs, the lift and drag are both synchronized at f_E , the lift has almost zero amplitude, the mean drag drops and saturates at a constant value regardless of f_E but its RMS value grows quadratically with f_E , the wake structure and shedding change and become instantaneously symmetric, and the coupling between the lift and drag changes. Whereas the linear coupling between the synchronized lift and drag is similar for the in-line and cross-flow motions, their quadratic coupling is different. The drag excites the lift for all cases, synchronized or not, and mechanical work is done on the flow by the drag and the motion. The instantaneous symmetry in the vortex structure affects the surface distribution of the pressure, which in turn explains the qualitative

and quantitative changes in the lift and drag when they become synchronized.

References

- Al-Jamal, H., and Dalton, C., 2004, “Vortex-Induced Vibrations Using Large Eddy Simulation at a Moderate Reynolds Number,” *Journal of Fluids and Structures*, vol. 19, pp. 73–92.
- Assi, G. R. S., and Bearman, P. W., 2008, “VIV Suppression and Drag Reduction with Pivoted Control Plates on a Circular Cylinder,” 27th International Conference on Offshore Mechanics and Arctic Engineering, Estoril, Portugal.
- Baek, S. J., and Lee, S. B., 2001, “Response of a Circular Cylinder Wake to Superharmonic Excitation,” *Journal of Fluid Mechanics*, vol. 442, pp. 67–88.
- Balasubramanian, S., and Skop, R. A., 1996, “A Nonlinear Oscillator Model for Vortex Shedding from Cylinders and Cones in Uniform and Shear Flows,” *Journal of Fluids and Structures*, vol. 10(3), pp. 197–214.
- Baldwin, B. S., and Barth, T. J., 1990, “A One-Equation Turbulence Transport Model for High Reynolds Number Wall-Bounded Flows,” NASA Technical Memorandum 102847. Also in 29th AIAA Aerospace Sciences Meeting, Reno, Nevada, January 7-10, 1991.
- Barret, C., 1996, “Review of Our National Heritage of Launch Vehicles Using Aerodynamic Surfaces and Current Use of These by Other Nations,” NASA Technical

Paper 3615.

Bernitsas, M. M., and Raghavan, K., 2008, "Reduction/Suppression of VIV of Circular Cylinders through Roughness Distribution at $8 \times 10^3 < Re < 1.5 \times 10^5$," 27th International Conference on Offshore Mechanics and Arctic Engineering, Estoril, Portugal.

Birkhoff, G., and Zarantonello, E. H., 1957, *Jets, Wakes, and Cavities*, Academic Press, New York.

Bishop, R. E. D., and Hassan, A. Y., 1964, "The Lift and Drag Forces on a Circular Cylinder in a Flowing Fluid," *Proceedings of the Royal Society Series A*, vol. 277, pp. 32–50.

Blackburn, H., and Henderson, R., 1996, "Lock-In Behavior in Simulated Vortex-Induced Vibration," *Experimental Thermal and Fluid Science*, vol. 12, pp. 184–189.

Blackburn, H. M., and Henderson, R. D., 1999, "A Study of Two-Dimensional Flow past an Oscillating Cylinder," *Journal of Fluid Mechanics*, vol. 385, pp. 255–286.

Blevins, R. D., 1974, "Flow Induced Vibration of Bluff Structures," Ph.D. Dissertation, Dynamics Laboratory, California Institute of Technology, Pasadena, California.

Blevins, R. D., 1990, *Flow-Induced Vibration*, Second Edition, Van Nostrand Reinhold, New York.

Blevins, R. D., and Coughran, C. S., 2008, "Experimental Investigation of Vortex-Induced Vibration in Two-Dimensions," 18th International Offshore (Ocean)

and Polar Engineering Conference & Exhibition, Vancouver, Canada, July 6-11, 2008, vol. 3, pp. 475–480.

Brown, D. P., Kauppinen, E. I., Jokiniemi, J. K., Rubin, S. G., and Biswas, P., 2006, “A Method of Moments Based CFD Model for Polydisperse Aerosol Flows with Strong Interphase Mass and Heat Transfer,” *Computers & Fluids*, vol. 35(7), pp. 762–780.

Botelho, D. L., 1983, “An Empirical Model for Vortex-Induced Vibrations,” Ph.D. Dissertation, California Institute of Technology, Pasadena, California.

Campioli, T. L., 2005, “The Assessment of Formulations for Numerical Solutions of Low Speed, Unsteady, turbulence Flows over Bluff Bodies,” M.S. Thesis, Department of Aerospace and Ocean Engineering, Virginia Tech, Blacksburg, Virginia.

Carberry, J., Sheridan, J., and Rockwell, D., 2001, “Forces and Wake Modes of an Oscillating Cylinder,” *Journal of Fluids and Structures*, vol. 15, pp. 523–532.

Carberry, J., Sheridan, J., and Rockwell, D., 2002, “Vortex Forces on an Oscillating Cylinder,” ASME International Mechanical Engineering Congress & Exposition, New Orleans, Louisiana, November 17-22.

Chorin, A. J., 1967, “A Numerical Method for Solving Incompressible Viscous Flow Problems,” *Journal of Computational Physics*, vol. 2, pp. 12–26.

Constantinides, Y., and Oakley, O. H., Jr, 2006, “Numerical Prediction of Bare and Straked Cylinder VIV,” 25th International Conference on Offshore Mechanics and Arctic Engineering, Hamburg, Germany.

- Currie, I. G., and Turnball, D. H., 1987, "Streamwise Oscillations of Cylinders near the Critical Reynolds Number," *Journal of Fluids and Structures*, vol. 1, pp. 185–196.
- Dahl, J. M., Hover, F. S., and Triantafyllou, M. S., 2008, "High Harmonic Forces and Predicted Vibrations from Forced In-Line and Cross-Flow Cylinder Motions," 18th International Offshore (Ocean) and Polar Engineering Conference & Exhibition, Vancouver, Canada, July 6-11, vol. 3, pp. 481-488.
- Dalton, C., 2006, Personal communication with Professor Charles Dalton, University of Houston, Department of Mechanical Engineering.
- Di Silvio, G., Angrilli, F., and Zanardo, A., 1975, "Fluidelastic Vibrations: Mathematical Model and Experimental Result," *Meccanica*, vol. 10(4), pp. 269–279.
- Dong, S., Lucor, D., and Karniadakis, G. E., 2004, "Flow past a Stationary and Moving Cylinder: DNS at Re=10000," Users Group Conference (DOD-UGC'04), Williamsburg, Virginia, June 7-11, pp. 88–95.
- Dong, S., and Karniadakis, G. E., 2005, "DNS of Flow past a Stationary and Oscillating Cylinder at Re=10000," *Journal of Fluids and Structures*, vol. 20(4), pp. 519–531.
- Facchinetti, M. , De Langre, E., and Biolley, F., 2004, "Coupling of Structure and Wake Oscillators in Vortex-Induced Vibrations," *Journal of Fluids and Structures*, vol. 19, pp. 123–140.
- Feng, C. C., 1968, "The Measurement of Vortex Induced Effects in Flow past Stationary and Oscillating Circular and D-Section Cylinders," M.S. Thesis, Department of Mechanical Engineering, University of British Columbia, Vancouver, Canada.

- Fletcher, C. A. J., 1991, *Computational Techniques for Fluid Dynamics*, Volume II, Second Edition, Springer-Verlag, Heidelberg.
- Gopalkrishnan, R., 1993, "Vortex-Induced Forces on Oscillating Bluff Cylinders," Ph.D. Dissertation, Massachusetts Institute of Technology, Massachusetts.
- Griffin, O. M., Skop, R. A., and Koopmann, G. H., 1973, "The Vortex-Excited Resonant Vibrations of Circular Cylinders," *Journal of Sound and Vibration*, vol. 31(2), pp. 235–249.
- Griffin, O. M., 1980, "Vortex-Excited Cross-Flow Vibrations of Single Cylindrical Tube," *Journal of Pressure Vessel Technology*, vol. 102, pp. 158–166.
- Gu, W., Chyu, C., and Rockwell, D., 1994, "Timing of Vortex Formation from an Oscillating Cylinder," *Physics of Fluids*, vol. 6(11), pp. 3677–3682.
- Harlow, F. H., and Weich, J. E., 1965, "Numerical Calculation of Time-Dependent Viscous Incompressible Flow of Fluid with Free Surface," *Physics of Fluids*, vol. 8, pp. 2182–2189.
- Hartlen, R. T., and Currie, I. G., 1970, "Lift-Oscillator Model of Vortex Vibration," *Journal of Engineering Mechanics*, vol. 96, pp. 577–591.
- Ibrahim, R. A., 2005, *Liquid Sloshing Dynamics: Theory and Applications*, Cambridge University Press.
- Iwan, W. D., and Blevins, R. D., 1974, "A Model for Vortex Induced Oscillation of Structures," *Journal of Applied Mechanics*, vol. 41(3), pp. 581–586.
- Kaiktsis, L., Triantafyllou, G. S., and Özbas, M., 2007, "Excitation, Inertia, and Drag Forces on a Cylinder Vibrating Transversely to a Steady Flow," *Journal*

of Fluids and Structures, vol. 23(1), pp. 1–21.

Keulegan, G. H., and Carpenter, L. H., 1958, “Forces on Cylinders and Plates in an Oscillating Fluid,” *Journal of Research of the National Bureau of Standards*, vol. 60, pp. 423–440.

Khalak, A., and Williamson, C. H. K., 1999, “Motions, Forces, and Mode Transitions in Vortex-Induced Vibrations at Low Mass-Damping,” *Journal of Fluids and Structures* vol. 13(7-8), pp. 813-851.

Kim, B. H., and Williams, D. R., 2006, “Nonlinear Coupling of Fluctuating Drag and Lift on Cylinders Undergoing Forced Oscillations,” *Journal of Fluid Mechanics*, vol. 559, pp. 335–353.

King, R., 1977, “A Review of Vortex Shedding Research and Its Application,” *Ocean Engineering*, vol. 4, pp. 141–171.

Korpus, R., Jones, P., Oakley, O., and Imas, L., 2000, “Prediction of Viscous Forces on Oscillating Cylinders by Reynolds-Averaged Navier-Stokes Solver,” 10th International Offshore and Polar Engineering Conference, Seattle, Washington, May 28-June 2.

Kovaszny, L. S. G., 1949, “Hot-Wire Investigation of the Wake Behind Cylinders at Low Reynolds Numbers,” *Proceedings of the Royal Society of London Series A*, vol. 198, pp. 174–190.

Krenk, S., and Nielsen, S. R. K., 1999, “Energy Balanced Double Oscillator Model for Vortex-Induced Vibrations,” *Journal of Engineering Mechanics*, vol. 125(3), pp. 263–271.

- Landl, R., 1975, "A Mathematical Model for Vortex-Excited Vibrations of Bluff Bodies," *Journal of Sound and Vibration*, vol. 42(2), pp. 219–234.
- Liu, C., Zheng, X., and Sung, C. H., 1998, "Preconditioned Multigrid Methods for Unsteady Incompressible Flows," *Journal of Computational Physics*, vol. 139, pp. 35–57.
- Lu, X., and Dalton, C., 1996, "Calculation of the Timing of Vortex Formation from an Oscillating Circular Cylinder," *Journal of Fluids and Structures*, vol. 10(5), pp. 527–541.
- Marx, Y. P., 1994, "Time Integration Schemes for the Unsteady Incompressible NavierStokes Equations," *Journal of Computational Physics*, vol. 112, pp. 82–209.
- Marzouk, O. A., Nayfeh, A. H., Arafat, H. N., and Akhtar, I., 2007, "Modeling Steady-State and Transient Forces on a Cylinder," *Journal of Vibration and Control*, vol. 13(7), pp. 1065–1091.
- Marzouk, O. A., and Nayfeh, A. H., 2007, "A Study of the Forces on an Oscillating Cylinder," 26th International Conference on Offshore Mechanics and Arctic Engineering, San Diego, California, June 10-15.
- Marzouk, O. A., and Nayfeh, A. H., 2008a, "Physical Interpretation of the Nonlinear Phenomena in Excited Wakes," 27th ASME Wind Energy Symposium, Reno, Nevada, January 7-10.
- Marzouk, O. A., and Nayfeh, A. H., 2008b, "New Wake Models with Capability of Capturing Nonlinear Physics," 27th International Conference on Offshore Mechanics and Arctic Engineering, Estoril, Portugal, June 15-19.

- Marzouk, O. A., and Nayfeh, A. H., 2008c, “Detailed Characteristics of the Resonating and Non-Resonating Flows Past a Moving Cylinder,” 16th AIAA/ASME/AHS Adaptive Structures Conference, Schaumburg, Illinois.
- Medici, D., 2004, “Wind Turbine Wakes - Control and Vortex Shedding,” Technical Report, Royal Institute of Technology, Stockholm, Sweden.
- Meneghini, J. R., Saltara, F., and Bearman, P. W., 1997, “Numerical Simulation of Vortex Shedding from an Oscillating Circular Cylinder,” 8th International Conference on Computational Methods and Experimental Measurements (CMEM 97), Rhodes, Greece, May 21-23, pp. 409–418.
- Meneghini, J. R., and Bearman, P. W., 1996, “Numerical Simulation of the Interaction between the Shedding of Vortices and Square-Wave Oscillations Applied to a Circular Cylinder,” 2nd International Conference on Hydrodynamics, Hong Kong, editors L. Chwang and B. Leung, December 16-19, vol. 2, pp. 785–790.
- Modarres-Sadeghi, Y., Hover, F. S., and Triantafyllou, M. S., 2008, “Fatigue Calculation of Risers Using a van der Pol Wake Oscillator Model With Random Parameters,” 27th International Conference on Offshore Mechanics and Arctic Engineering, Estoril, Portugal, June 15-20.
- Moe, G., and Wu, Z. J., 1990, “The Lift Force on a Vibrating Cylinder in a Current,” *Journal of Offshore Mechanics and Arctic Engineering*, vol. 112(4), pp. 297–303.
- Muldoon, F., and Acharya, S., 2007, “A Modification of the Artificial Compressibility Algorithm with Improved Convergence Characteristics,” *International Journal for Numerical Methods in Fluids*, vol. 55, pp. 307–345.

- Mureithi, N. W., Goda, S., and Kanki, H., 2001, "A Nonlinear Dynamics Analysis of Vortex-Structure Interaction Models," *Journal of Pressure Vessel Technology*, vol. 123(4), pp. 475–479.
- Nayfeh, A. H., 1973, *Perturbation Methods*, Wiley, New York.
- Nayfeh, A. H., 1981, *Introduction to Perturbation Techniques*, Wiley, New York.
- Nayfeh, A. H., and Balachandran, B., 1995, *Applied Nonlinear Dynamics: Analytical, Computational, and Experimental Methods*, Wiley, New York.
- Nayfeh, A. H., Owis, F., and Hajj, M. R., 2003, "A Model for the Coupled Lift and Drag on a Circular Cylinder," ASME International Design Engineering Technical Conferences & Computers and Information in Engineering Conference, Chicago, Illinois, September 2-6.
- Norberg, C., 1993, "Pressure Forces on a Circular Cylinder in Cross Flow," In: Eckelmann, H., Graham, J. M. R., Huerre, P., and Monkewitz, P. A., editors, *IUTAM Symposium on Bluff-Body Wakes, Dynamics and Instabilities*, Göttingen, Germany, 1992, Springer-Verlag, Berlin (1993), pp. 275-278.
- Norberg, C., 2003, "Fluctuating Lift on a Circular Cylinder: Review and New Measurements," *Journal of Fluids and Structures*, vol. 17, pp. 57–96.
- Ogink, R. H. M., and Metrikine, A. V., 2008, "A Wake Oscillator with Frequency Dependent Tuning Coefficients for the Modeling of VIV," 27th International Conference on Offshore Mechanics and Arctic Engineering, Estoril, Portugal, June 15-20.

- Owis, F. M., and Nayfeh, A. H., 2001, "Numerical Simulation of Super- and Partially-Cavitating Flows over an Axisymmetric Projectile," 39th AIAA Aerospace Sciences Meeting and Exhibit, Reno, Nevada, January 8-11.
- Owis, F. M., and Nayfeh, A. H., 2004, "Numerical Simulation of 3-D Incompressible, Multi-Phase Flows over Cavitating Projectiles," *European Journal of Mechanics - B/Fluids*, vol. 23(2), pp. 339–351.
- Pantazopoulos, M. S., 1994, "Vortex-Induced Vibration Parameters: Critical Review," 13th International Conference on Offshore Mechanics and Arctic Engineering, Houston, Texas, February 27-March 3, vol. 1, pp. 199-255.
- Parkinson, G. V., Feng, C. C., and Ferguson, N., 1968, "Mechanism of Vortex-Excited Oscillation of Bluff Cylinders," The Symposium on Wind Effects on Buildings and Structures, Loughborough, England, paper 27.
- Patankar, S. V., and Spalding, D. B., 1972, "A Calculation Procedure for Heat, Mass and Momentum Transfer in Three-Dimensional Parabolic Flows", *International Journal of Heat and Mass Transfer*, vol. 15, pp. 1787–1806.
- Placzek, A., Sigrist, J.-F., and Hamdouni, A., 2009, "Numerical Simulation of an Oscillating Cylinder in a Cross-Flow at Low Reynolds Number: Forced and Free Oscillations," *Computers & Fluids*, vol. 38(1), pp. 80–100.
- Qin, L., 2004, "Development of Reduced-Order Models for Lift and Drag on Oscillating Cylinders with Higher-Order Spectral Moments," Ph.D. Dissertation, Department of Engineering Science and Mechanics, Virginia Tech, Blacksburg, Virginia.

- Rayleigh, L., 1879, "Acoustical Observations," *Philosophical Magazine*, vol. 7, pp. 149–162.
- Rogers, S. E., Kwak, D., and Kiris, C., 1991, "Steady and Unsteady Solutions of the Incompressible Navier-Stokes Equations," *AIAA Journal*, vol. 29(4), pp. 603–610.
- Roshko, A., 1953, "On the Development of Turbulent Wakes from Vortex Streets," NACA Technical Note 2913.
- Saltara, F., Meneghini, J. R., Siqueira, C. R., and Bearman, P. W., 1998, "The Simulation of Vortex Shedding from an Oscillating Circular Cylinder with Turbulence Modelling," 1st Bluff Body Wakes and Vortex-Induced Vibrations Conference and ASME Fluids Engineering Division Summer Meeting, Washington D.C., June 21-25.
- Sarpkaya, T., 1978, "Fluid Forces on Oscillating Cylinders," *Journal of Waterway, Port Coastal and Ocean Division, Proceedings of ASCE*, WW4, vol. 104, pp. 275–290.
- Sarpkaya, T., and Isaacson, M., 1981, *Mechanics of Wave Forces on Offshore Structures*, Van Nostrand-Reinhold, New York.
- Siegel, S., Cohen, K., and McLaughlin, T., 2006, "Numerical Simulations of a Feedback-Controlled Circular Cylinder Wake," *AIAA Journal*, vol. 44(6), pp. 1266–1276.
- Skop, R. A., 1974, "On Modelling Vortex-Excited Oscillations," Naval Research Laboratory Memorandum Report 2927.

- Skop, R. A., and Griffin, O. M., 1973, "A Model for the Vortex-Excited Resonant Response of Bluff Cylinders," *Journal of Sound and Vibration*, vol. 27(2), pp. 225–233.
- Skop, R. A., and Griffin, O. M., 1975, "On the Theory for the Vortex-Excited Oscillations of Flexible Cylindrical Structures," *Journal of Sound and Vibration*, vol. 41(3), pp. 263–274.
- Soh, W. Y., and Goodrich, J. W., 1988, "Unsteady Solution of Incompressible NavierStokes Equations," *Journal of Computational Physics*, vol. 79, pp. 113–134.
- Spalart, P. R., and Allmaras, S. R., 1992, "A One-Equation Turbulence Model for Aerodynamic Flows," 30th AIAA Aerospace Sciences Meeting and Exhibit, Reno, Nevada, January 6-9.
- Staubli, T., 1983, "Calculation of the Vibration of an Elastically Mounted Cylinder Using Experimental Data from Forced Vibration," *ASME Journal of Fluids Engineering*, vol. 105(2), pp. 225-229.
- Stewart, B. , Leontini, J. , Hourigan, K., and Thompson, M. C., 2005, "Vortex Wake and Energy Transitions of an Oscillating Cylinder at Low Reynolds Number," *Australian and New Zealand Industrial and Applied Mathematics Journal (ANZIAM) Journal*, vol. 46(E), pp. C181–C195.
- Strouhal, V., 1878, "Uber eine Besondere Art der Tonerregung," *Annalen der Physik und Chemie (Leipzig)*, vol. 5, pp. 216–251.
- Tanida, Y., Okajima, A., and Watanabe, Y., 1973, "Stability of a Circular Cylinder Oscillating in Uniform Flow or in a Wake," *Journal of Fluid Mechanics*, vol.

61, pp. 769–784.

Torum, A., Moe, G., Johansen, J. V., and Katla, E., 1996, “On Current Induced In-Line Oscillation in Pipelines Free-Spans,” 15th International Conference on Offshore Mechanics and Arctic Engineering, Florence, Italy, June 16-20, vol. 5, 459–469.

Vandiver, J. K., 1987, “The Relationship between In-Line and Cross-Flow Vortex-Induced Vibration in Cylinder,” *Journal of Fluids and Structures*, vol. 1, pp. 381–399.

Vickery, B. J., and Watkins, R. D., 1962, “Flow Induced Vibration of Cylindrical Structures,” 1st Australian Conference on Hydraulics and Fluid Mechanics, Nedlands, Western Australia, December 6-13.

Wen, C. Y., Yeh, C. L., Wang, M. J., and Lin, C. Y., 2004, “On the Drag of Two-Dimensional Flow about a Circular Cylinder,” *Physics of Fluids*, vol. 16(10), pp. 3828–3831.

Wilcox, D. C., 2001, “Turbulence Modeling - An Overview,” 39th AIAA Aerospace Sciences Meeting, Reno, Nevada, January 8-11.

Williamson, C. H. K., 1985, “Sinusoidal Flow Relative to Circular-Cylinders,” *Journal of Fluid Mechanics*, vol. 155, pp. 141–174.

Williamson, C. H. K., and Roshko, A., 1988, “Vortex Formation in the Wake of an Oscillating Cylinder,” *Journal of Fluids and Structures*, vol. 2, pp. 355–381.

Williamson, C. H. K., and Roshko, A., 1990, “Measurements of Base Pressure in the Wake of a Cylinder at Low Reynolds Numbers,” *Zeitschrift für Flugwissenschaften und Weltraumforschung*, vol. 14, pp. 38-46.

- Williamson, C. H. K., 1996, "Vortex Dynamics in the Cylinder Wake," *Annual Reviews of Fluid Mechanics*, vol. 28, pp. 477–539.
- Wu, Z. J., 1989, "Current Induced Vibrations of a Flexible Cylinder," N.T.H. Report, Division of Structural Engineering, The Norwegian Institute of Technology, University of Trondheim, Norway.
- Zdravkovich, M. M., 1982, "Modification of Vortex Shedding in the Synchronization Range," *Journal of Fluids Engineering*, vol. 104, pp. 513–517.
- Zheng, Z. C., and Zhang, N., 2008, "Frequency Effects on Lift and Drag for Flow past an Oscillating Cylinder," *Journal of Fluids and Structures*, vol. 24(3), pp. 382–399.